DISS. ETH NO. 15984

CMOS-Integrated Cantilevers for Biosensing and Probe Microscopy

A dissertation submitted to the

SWISS FEDERAL INSTITUTE OF TECHNOLOGY ZURICH

for the degree of

Doctor of Natural Sciences

presented by

Tormod Volden
Ingénieur Diplômé, INSA Toulouse

born 09.12.1971
citizen of Norway

accepted on the recommendation of

Prof. Henry Baltes, examiner
Prof. Oliver Brand, co-examiner
Dr. Jan Lichtenberg, co-examiner

2005

CONTENTS

ABSTRACT

This thesis presents the design, fabrication and characterization of CMOS-based cantilever sensor systems. Two different applications were investigated: cantilever arrays for surface-stress sensing, targeted for the detection of biomolecules, and cantilever arrays for atomic force microscopy (AFM). Both systems were fabricated in a standard industrial CMOS process with subsequent micromachining. The sensors were integrated with electronic circuitry in order to form high-performance, single-chip sensor systems with a high level of functionality and flexibility.

Integrated piezoresistive sensor elements facilitate the integration with the on-chip circuitry. In contrast to optical read-out, which dominates in cantilever-sensor research, the integrated electronic read-out can be easily applied to large arrays of cantilevers. For the AFM system, the integration of individual height actuation is crucial for parallel multi-cantilever scanning.

Because of the on-chip, high-gain amplification, the sensor offset signals have to be compensated in order to not saturate the subsequent signal-conditioning stages. This was performed in both applications with symmetric Wheatstone bridges and reference cantilevers. Additional offset compensation schemes were also included in the circuitry.

The surface-stress sensor system features four crystalline-silicon cantilevers with embedded piezoresistors. Both single-cantilever and dual-cantilever (where one cantilever acts as a reference sensor) operation are possible. The on-chip circuitry has a total gain of up to 67 dB and also includes low-pass filtering. The sensor system has been characterized by mechanical deflection of the cantilevers as well as by employing it for humidity and volatile-organic-compound detection based on polymer swelling. The operation of the system in liquid environment has been studied in order to prepare the system for the detection of biomolecules.

A thorough characterization of thermally actuated cantilevers was performed on previously designed AFM systems. This served as a foundation for the design of a new AFM system, which features ten scanning cantilevers with embedded piezoresistive force sensors and thermal bimorphs with integrated heaters for height actuation. The analogue circuitry has a gain of up to 64 dB. Integrated, digital

controllers allow individual, closed-loop operation of four cantilevers simultaneously. The height and force data is transferred over a digital, high-speed interface. Characterization of the cantilevers and the total system is presented along with examples of scanned images.

Fabrication process development was undertaken to ensure a high fabrication yield for the fragile cantilever structures. Packaging and interconnection issues were studied in order to facilitate system integration and commercial application.

ZUSAMMENFASSUNG

Design, Fabrikation und Charakterisierung von CMOS-basierten Cantilever-Sensoren stehen im Mittelpunkt dieser Arbeit. Dabei wurden zwei Anwendungen untersucht: Cantilever-Arrays zur Bestimmung von Oberflächenstress für die Detektion von Biomolekülen, sowie Arrays für Atomkraftmikroskopie (AFM). Beide Systeme wurden in einem Standard-CMOS-Prozess gefolgt von zusätzlichen Mikrofabrikationsschritten hergestellt. Dies ermöglicht die Integration von mikroelektronischen Schaltungen mit den Sensoren, um leistungsfähige, monolithische Sensorsysteme mit einem hohen Grad an Funktionalität und Flexibilität zu bilden.

Diese Integration wird durch die Verwendung von integrierten, piezoresistiven Sensorelementen erleichtert. Im Gegensatz zu den in diesem Forschungsgebiet immer noch dominierenden optischen Ausleseverfahren, lässt sich die integrierte, elektronische Detektionsmethode leicht auf umfangreichere Cantilever-Arrays ausdehnen. Für die Parallelisierung des AFM-Systems ist ausserdem die Integration einer für jeden Cantilever individuellen Vertikalansteuerung notwendig.

Aufgrund der auf dem Chip integrierten, hochempfindlichen Verstärker ist eine Offsetkompensation der Sensorsignale erforderlich, um ein Übersteuern der Eingangsstufen zu vermeiden. Für beide Systeme wurde dies durch den Einsatz symmetrischer Wheatstone-Brücken mit integrierten Referenz-Cantilevern erreicht. Zusätzliche Verfahren zur Offsetkompensation wurden direkt in der Schaltung vorgesehen.

Der Oberflächenstress-Sensor verfügt über vier Cantilever aus kristallinem Silizium mit integrierten Piezoresistoren. Dabei ist ein Betrieb sowohl mit einzelnen als auch mit paarweisen Cantilevern möglich; im letzteren Fall wird ein Cantilever als Referenz verwendet. Die dazugehörige Schaltung erreicht eine Gesamtverstärkung von 67 dB und enthält einen Tiefpassfilter. Das System wurde mechanisch durch Auslenken der Cantilever charakterisiert. Nachdem die Cantilever mit einem geeigneten Polymer beschichtet wurden, liess sich das System ausserdem als Sensor für Luftfeuchtigkeit und für organische Lösungsmittel einsetzen. Abschliessend wurde die Verwendung des Systems in Flüssigkeiten unter-

sucht, um den Sensor in Zukunft für die Detektion von Biomolekülen einsetzen zu können.

Für das AFM-System wurden die thermisch ausgelenkten Cantilever einer Vorversion des Chips eingehen charakterisiert. Dies bildete die Grundlage für das Design des neuen AFM-Chips, der mit zehn Sensorcantilevern mit integrierten, piezoresistiven Kraftsensoren und thermischen Bimetallaktoren mit eingebauten Heizern ausgestattet ist. Die analoge Verstärkung beträgt hier 64 dB. Integrierte, digitale Regler ermöglichen die Steuerung in Rückgekopplung von vier Cantilevern gleichzeitig. Die gewonnenen Höhen- und Kraftinformationen werden über ein digitales Hochgeschwindigkeits-Interface nach aussen übermittelt. Eine Charakterisierung der Cantilever und des Gesamtsystems wird mit einigen Beispielscans erläutert.

Parallel zu den beiden Projekten wurde der Herstellungsprozess für eine bessere Ausbeute der zerbrechlichen Cantileverstrukturen weiterentwickelt. Aspekte der Aufbau- und Verbindungstechnik wurden untersucht, um die Systemintegration und Kommerzialisierung zu ermöglichen.

1 INTRODUCTION

1.1 MICROSENSORS

Sensors are devices capable of detecting physical or chemical quantities, such as light, temperature, pressure or gas concentration. Using modern fabrication techniques, often adapted from the microelectronic industry, a new generation of sensors with dimensions in the micrometer range has emerged. These sensors offer high sensitivity and accuracy at low manufacturing cost. Low power consumption and small size are other inherent advantages of this technology, often referred to as microelectromechanical systems (MEMS). In addition to replacing old sensor systems, microsensors find new applications in all aspects of modern life: from household appliances and entertainment products, to medical technology and security detectors, to space probes for interplanetary exploration.

The combination of microsensors and miniaturized electronic circuitry allows, for instance, the cellular phone in our pocket to carry a camera, the wrist-watch to include a pressure sensor and a computer mouse or joystick to use a motion detector. Inside our cars, a micro accelerometer reliably detects collisions and triggers air-bag release, while sensors inside the tires alert the driver of a diminishing tire pressure. Microsensors are also finding their way into medical applications, with promise of small, fast and easy-to-use equipment and new methods for early diagnosis and treatment.

The modern electronic industry is dominated by the complimentary metal-oxide-semiconductor (CMOS) technology. CMOS chips are mass-produced at low cost, consume little power and are consequently found in every computer as well as most other electronic equipment.

Monolithic co-integration of microelectronics and microsensors in CMOS technology has been successfully demonstrated [Baltes1996]. This allows industrial sensor fabrication at low cost and high precision in existing manufacturing facilities. The sensors can be tightly integrated with the electronic circuitry, creating smart sensors with a high degree of functionality on a single chip.

A whole family of microsensors is based on mechanical cantilever structures. These microcantilevers act as high-sensitivity transducers converting one physical quantity into another. For instance, a microcantilever for atomic force microscopy (AFM) translates a force on the cantilever tip into a deflection. For a vibrating cantilever, the force changes the cantilever's resonance frequency. In chemical and biochemical microcantilever sensors, the binding between an analyte and the cantilever surface changes the surface stress or the mass of the cantilever, which results in bending or change of the resonance frequency, respectively.

1.2 Motivation of this Thesis

AFM Cantilever Systems

In the field of AFM and other probe microscopy techniques, passive cantilevers in combination with an optical read-out are the norm. Self-sensing cantilevers that integrate piezoresistive or piezoelectric force sensors offer an alternative to the optical read-out and have recently become commercially available [Veeco2005]. Integrated actuation of the cantilevers using piezoelectric layers or thermal bimorphs has been used to speed up the topology tracking of the cantilever tip and hence allow for faster scanning [Minne1998]. The combination of integrated sensor and actuator elements greatly simplifies the development of cantilever arrays [Minne1999]. Use of multiple cantilevers in an array can speed up scanning through parallelization, widen the scanning range and provide redundancy [Staufer2000].

The complexity and cost of fabrication, the demanding set-up and the operation of these array systems have so far been a hindrance to commercial development and wide-spread use.

The work in this thesis was focused on the use of standard CMOS technology in in order to develop cantilever arrays for AFM with high functionality at low cost. Fabrication, packaging and integration of electronics were developed towards an easy-to-use, one-chip solution providing the core of a versatile, high-performance AFM system.

Cantilever-Based Biochemical Sensors

There is an increasing interest in the development of cantilever-based sensors for detection of biomolecules [Thundat1995, Wu2001]. As for microscopy cantilever systems, the optical read-out schemes are dominating [Battiston2001]. A few examples of integrated piezoresistive detection have been developed [Thaysen2001]. Many of the advantages of sensor integration are shared with AFM systems, for example, the straight-forward extension into sensor arrays. Arrays of cantilevers can be used to simultaneously probe for multiple analytes as well as to increase the signal-to-noise ratio by providing reference cantilevers [Boisen2000]. A large part of the research performed in this area relies on the use of modified AFM cantilevers, which are not optimized for the detection of surface-stress changes induced by biomolecular reactions. There is still a lack of optimized sensor and cantilever designs for the mechanical detection of analyte-surface binding.

In the scope of this thesis, new sensor array systems were developed for the detection of surface stress. CMOS technology was the method of choice for the sensor development, which would also allow downstream commercialization and mass-production. The envisioned product would be a compact medical diagnosis system.

Outline

This thesis presents the development, fabrication and characterization of two cantilever-based sensing systems. The surface-stress sensing system is discussed in Chapter 3 and the AFM array system in Chapter 4. Since both systems are based on microcantilever arrays with piezoresistive read-out, they share a common part of theory and design considerations. This is presented in Chapter 2, where also some fundamental differences of the two sensor functions are explained.

1.3 Summary of Major Results

CMOS-Integrated Cantilever System For Surface-Stress Sensing

A novel platform for the detection of surface-stress changes has been developed, fabricated and characterized (see Fig. 1.1a). The system benefits from standard, industrial CMOS technology to integrate the sensor elements. The sensors are combined with on-chip electronic circuitry to achieve low-noise performance and

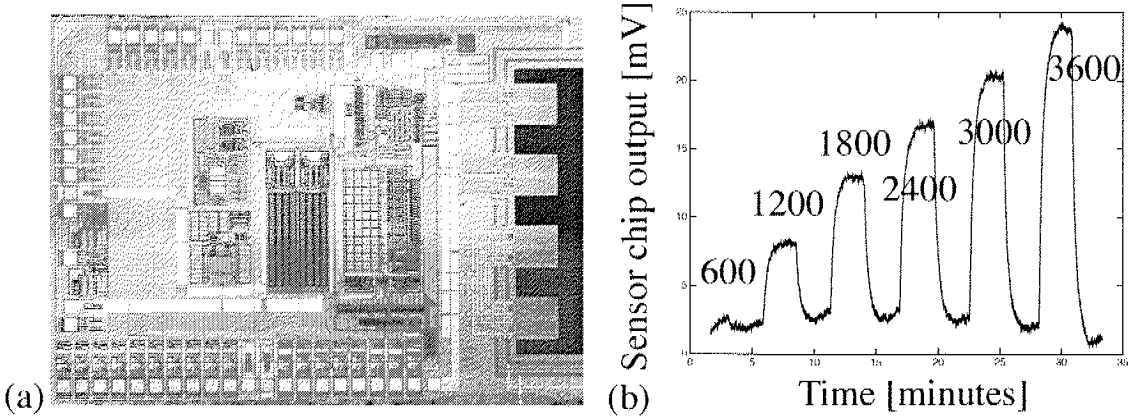

Fig. 1.1: (a) CMOS-integrated system for surface-stress sensing including an array of cantilevers and signal conditioning circuitry. The chip measures 3.9 mm x 2.7 mm. (b) Detection of volatile organic compounds: Ethanol in concentration steps from 600 ppm to 3600 ppm (see Section 3.6.4).

a high degree of flexibility. Various configurations of sensing layers and reference cantilevers have been implemented, including fully symmetric Wheatstone bridges for reduced sensor offset. The system is targeted for "biosensing" – the detection of specific biomolecules, but can also be used for a variety of related surface-stress experiments. This has been demonstrated by the detection of volatile organic compounds (see Fig. 1.1b) as well as by humidity sensing.

CMOS-Integrated AFM Cantilever Array System

Cantilever arrays for atomic force microscopy were developed and integrated with on-chip electronics to form a complete AFM system (see Fig. 1.2a). The possibilities of standard, industrial CMOS technology were exploited to achieve a high level of functionality at low cost. The cantilevers include piezoresistive force sensors and thermal actuators. The on-chip circuitry includes digital, closed-loop controllers to enable, e.g., constant-force mode microscopy or force-distance measurements for surface chemistry analysis. The processing capacity of the digital signal processing unit is 16 million arithmetic operations per second. Fully integrated signal processing and a digital interface reduce the need for external components and simplify the system integration.

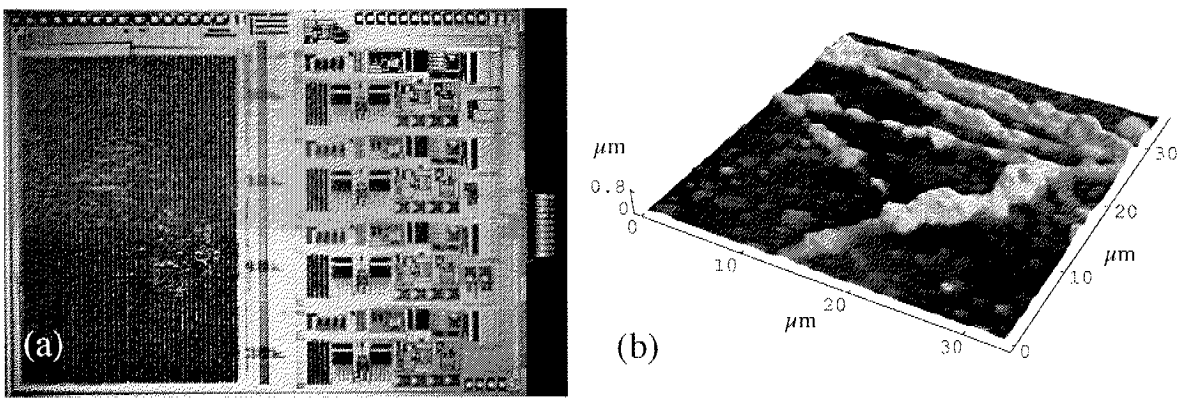

Fig. 1.2: (a) CMOS-integrated AFM system including an array of cantilevers and control circuitry. The chip size is 7 mm x 10 mm. (b) Image (scanned in constant-force mode) of a dried-out network of chicken neurites (see Section 4.5.5).

A comprehensive characterization of the thermal actuation was performed to tailor the control circuitry. Suppression of sensor offset was implemented by a novel reference cantilever structure. An example of an image scanned in constant-force mode is shown in Fig. 1.2b.

2 CMOS CANTILEVER SENSORS

This chapter gives a general overview of cantilever-based sensors, their application and the technology involved. The theory and design considerations discussed provide a base for the particular implementations presented in the following chapters.

Although the cantilevers used in both applications, AFM microscopy and surface-stress sensing, share a bulk of common background and theory, fundamental differences in their sensing mechanisms will be highlighted and will justify different design approaches. Some design considerations will be left for the appropriate chapters.

A summary of the theory of the piezoresistive effect and cantilever mechanics relevant to both applications will be followed by numerical simulations to exemplify important results. Finally, some general notes on fabrication will be given.

2.1 INTRODUCTION

2.1.1 APPLICATION OF CANTILEVER-BASED SENSORS

Cantilever-based sensors have found their use in physical sensing, scanning-probe microscopy, as well as in chemical and biological sensing. Although a cantilever sensor can have any size, the focus of this overview is on microsensors with feature dimensions in the micro- and nanometer range.

The breakthrough in their wide-spread usage came with the development of atomic force microscopy (AFM). After the invention of scanning tunnelling microscopy (STM) in 1981 [Binnig1982] which is based on the measurement of the electrical tunnelling current from a sharp tip to a (conducting) surface, AFM evolved as a way to also scan non-conducting surfaces [Binnig1986]. Here the contact (or near contact) force between a tip and a surface is measured. Long, thin cantilevers with low stiffness are used to translate the small force acting on

the tip at the end of the cantilever into a detectable (static) deflection. In the case of resonant (or dynamic) mode operation, the change of the vibrational resonance frequency caused by the tip-surface interaction is detected. A whole family of force-microscopy instruments uses cantilevers, and there is a large choice of commercially available (mainly passive) cantilevers for this purpose [Vecco2005].

Chemical and biological sensors require a sensing layer on the cantilever. The layer, often an application-specific coating, absorbs or interacts with the analyte in question and changes the properties of the cantilever. For instance, a change in the resonance frequency can be induced by the added mass of the bound or absorbed analyte [Thundat1995]. A change in surface stress can change the stiffness and hence also affect the resonance frequency [Chen1995] or it can create a static bending of the cantilever [Wu2001].

Some acceleration sensors (a microsensor application having a wide commercial exploitation) are also cantilever based, where a lumped mass on the cantilever's free end acts as an inertial mass and deflects the cantilever as the microsensor is subject to an acceleration [Ning1995, Sensonor2005].

Related to probe microscopy, there is also the use of cantilevers in micro-lithography and micro-manipulation, where the cantilever is moved over the surface and interacts with it in order to leave a defined pattern [Eigler1990]. IBM's *Millipede* project [Vettiger2002] is using arrays of cantilevers which thermally read information from and write to a flat polymer surface. In the last example, the mechanical properties of the cantilever play a less prominent role.

2.1.2 Sensing Methods

To be able to measure the response of the cantilever in a sensor system, a detection principle has to be chosen. The first AFM systems, derived from STM, used the tunnelling current between a conducting cantilever and a sharp, conducting tip held close to it, to monitor the deflection of the cantilever. The use of optical read-out schemes, where a laser beam is reflected off the cantilever and into a multi-cell photodetector that records the deviation angle, is currently seen in most applications. Sub-nanometer deflections can be detected by such methods [Meyer1988], but they often involve tedious alignment of the optics and issues when operating in media of different opacity and diffraction index. Interferom-

etry and diffraction patterns are also used to enhance the deflection sensitivity [Savran2003].

Capacitive read-out can be realized by measuring the capacitance between the cantilever and a fixed counter-electrode [Ghatnekar2005]. Potential sticking of the electrodes complicates this approach, and it is not well suited for liquid operation [Villarroya2004].

Integrated piezo-electric or -resistive elements are increasingly being used, for instance in AFM [Veeco2005]. Especially silicon sensors, where piezoresistive elements can be easily fabricated by doping, are suited for such integration. This allows for liquid operation, eased integration with electronics, low power consumption, and finally avoids the need for external components such as lasers and photodetectors.

2.1.3 Actuators

Active cantilevers, for instance for resonant systems or integrated force-feedback solutions, need an actuating principle. Magnetic actuation often features a current loop [Lange2003] or magnetic material [Han1996] in the cantilever immersed in a magnetic field. Electrostatic actuation can be applied in gas and vacuum operation [Ghatnekar2005], generally with the same limitations as for capacitive sensing. Piezoelectric elements have been integrated in fast-response AFM cantilevers [Minne1998]. Thermal actuation often profits from the bimorph effect, where the cantilever is heated, for instance by the current in an integrated heating resistor or by laser illumination, and the different thermal expansion coefficients of the layers in the cantilever create a resulting deflection [Brand1992].

2.1.4 CMOS Integration

CMOS is the dominant technology in mass-produced electronics. High volumes and strong competition bring the prices down while the performance of the integrated circuits keeps improving steadily. The monocrystalline silicon used in CMOS technology has also excellent, well-defined mechanical properties. Combined with the possibility of creating mechanical structures and devices using microfabrication technology, this has made silicon a successful building material for microsensors. The integration of sensor fabrication with standard industrial CMOS processing has shown to be a promising way of producing reliable and versatile microsensors [Parameswaran1989, Baltes1996]. The availability and

low unit price of commercial CMOS production and the advantages of integrated electronic circuitry allow for mass production of sensors with high functionality.

Elements of the CMOS process, originally established for the realization of transistors, resistors and other electronic components can, either by themselves or in combination with subsequent post-processing, provide sensor elements. The CMOS transistor source-drain diffusion (also used for resistors) has piezoresistive properties and can therefore be used as piezoresistive elements. This also applies to the deposited polycrystalline layers, traditionally used for resistors and capacitors as well as the transistor gate electrode. The n-well that encloses p-channel transistors can be used as an etch-stop layer during anisotropic silicon etching performed as post-processing [Müller1998]. The combination of silicon and metal layers can constitute bimorph elements for thermal actuation, with heating resistors integrated in the silicon. Some layer characteristics of a commercial CMOS process are summarized in Table 2.1.

*Tab. 2.1: Process parameters from a commercial 0.8 µm, double-metal CMOS process (courtesy of austria*microsystems*, Graz, Austria). (TCR = temperature coefficient of resistivity)*

Device layer	Example usage in sensor design	Thickness (μm)	Sheet resistance (Ω)	Min. width (μm)	TCR (10^{-3} K^{-1})
n-well	mechanical structures	3.50	1200	5.0	6.5
n^+ diffusion	piezoresistor	0.40	25	2.0	1.8
p^+ diffusion		0.40	40	2.0	1.7
polysilicon	piezoresistor, mech. struct.	0.42	23	0.8	0.9
metal-1	bimorph, sacrificial etch layer, current loop	0.6	0.07	1.4	3.0
metal-2		1.0	0.04	1.6	3.0

2.2 PIEZORESISTIVE EFFECT

All materials exhibit, at least to some degree, a piezoresistive effect, that is, the resistivity is changed as a function of the stress in the material. This is in part owing to strain and geometrical changes like elongation or reduction of the cross section, but for some materials the effect is much stronger. Typically, semiconductors have a strong piezoresistivity, which can be explained by the changes in the energy band gap as the crystal lattice is deformed resulting in a change in carrier mobility and carrier density.

2.2.1 PIEZORESISTIVE TENSOR

The resistivity in a solid is in general a second rank tensor ρ connecting the current density vector J and the electrical field vector E:

$$E = \rho J \tag{2.1}$$

In the linear approximation, considering small stresses, the piezoresistivity π, a tensor of fourth rank, links the stress tensor σ (of second rank) to the (change of) resistivity tensor ρ:

$$\frac{\Delta\rho}{\rho_0} = \pi\sigma, \tag{2.2}$$

where ρ_0 is the resisivity in absence of stress. Due to the symmetry of the stress tensor, the number of independent coefficients of the tensor π is at most 36. In the case of monocrystalline silicon (as well as germanium), the symmetry of the crystal lattice further reduces this number to 3, often referred to as π_{11}, π_{12} and π_{44} (engineering notation).

2.2.2 CRYSTALLINE SILICON

The devices presented in the following chapters have been fabricated on standard CMOS wafers, where the wafer surface is a (100) plane of the silicon lattice. The straight edges of the fabricated cantilevers have <110> orientations.

Measured values of the piezoresistive coefficients π_{ij} of low-doped silicon, in an orthogonal coordinate system aligned with the crystallographic axes, are shown in Table 2.2.

Tab. 2.2: Piezoresistive coefficients π_{ij} (10^{-11} Pa^{-1}) of low-doped crystalline silicon at room temperature for a coordinate system aligned with the principle crystallographic axes [Smith1954].

	π_{11}	π_{12}	π_{44}
p-type	6.6	-1.1	138.1
n-type	-102.2	53.4	-13.6

The equivalent values π'_{ij} for an arbitrary orientation can be found by coordinate transformation [Bao2000]. By choosing x, y, z along [110], [1$\underline{1}$0], [100], the expressions of resistance change for p-type resistors aligned along some typical straight and diagonal axes can be expressed as in Eqns. (2.3–2.6). The proportional, numerical expressions (b) are included for easier comparison of magnitudes and have the unit 10^{-11} Pa^{-1} omitted from all terms. For clarity the term $\pi_{12}\sigma_{zz}$, which is negligible for surface resistors, has been omitted from all expressions.

[110] *along x axis*:
$$\frac{\Delta R}{R} = \left(\frac{\pi_{11}+\pi_{12}+\pi_{44}}{2}\right)\sigma_{xx} + \left(\frac{\pi_{11}+\pi_{12}-\pi_{44}}{2}\right)\sigma_{yy} \quad (2.3)$$

$$\sim (71.6)\sigma_{xx} + (-66.3)\sigma_{yy} \quad (2.3b)$$

[1$\underline{1}$0] *along y axis*:
$$\frac{\Delta R}{R} = \left(\frac{\pi_{11}+\pi_{12}-\pi_{44}}{2}\right)\sigma_{xx} + \left(\frac{\pi_{11}+\pi_{12}+\pi_{44}}{2}\right)\sigma_{yy} \quad (2.4)$$

$$\sim (-66.3)\sigma_{xx} + (71.6)\sigma_{yy} \quad (2.4b)$$

[010] *x y of same sign*:
$$\frac{\Delta R}{R} = \left(\frac{\pi_{11}+\pi_{12}}{2}\right)(\sigma_{xx}+\sigma_{yy}) + (\pi_{11}-\pi_{12})\sigma_{xy} \quad (2.5)$$

$$\sim (2.75)(\sigma_{xx}+\sigma_{yy}) + (3.85)\sigma_{xy} \quad (2.5b)$$

$$[100]\ x\ y\ \textit{opposite sign}\text{:}\quad \frac{\Delta R}{R} = \left(\frac{\pi_{11}+\pi_{12}}{2}\right)(\sigma_{xx}+\sigma_{yy}) - (\pi_{11}-\pi_{12})\sigma_{xy} \tag{2.6}$$

$$\sim (2.75)(\sigma_{xx}+\sigma_{yy}) - (3.85)\sigma_{xy} \tag{2.6b}$$

Some observations can be made from the above expressions. For [110] and [1$\underline{1}$0] directions (horizontal and vertical to the primary flat of the (100) wafer) the shear stress component σ_{xy} does not contribute to a change of resistance. The coefficients of σ_{xx} and σ_{yy} are of different signs and similar magnitude, meaning that if σ_{xx} is similar to σ_{yy}, the resulting resistance change can be small and even zero.

For [010] and [100] directions (45° to the primary flat of the (100) wafer), σ_{xx} and σ_{yy} have equal coefficients, however in this case the shear stress component σ_{xy} is also contributing with a coefficient of similar magnitude and with respectively positive or negative sign.

The resistance change for a resistor of any direction can also be expressed as

$$\frac{\Delta R}{R} = \pi_L\sigma_L + \pi_T\sigma_T \tag{2.7}$$

where σ_L and σ_T are the stress components longitudinal and transversal to the resistor, and π_L and π_T are calculated from the above coefficients π_{ij}.

2.2.3 Polycrystalline Silicon

Polycrystalline silicon (polysilicon) is composed of grains of crystalline silicon of random orientation. The resulting piezoresistive coefficients (see Tab. 2.3), which can be approximated by averaging the monocrystalline parameters over all directions [Nathan1999, Bao2000], also depend on deposition and annealing conditions.

Since the Young's modulus E also varies, it is customary to characterize the piezoresistivity by the gauge factor $G = E\pi$ so that for a thin film resistor,

$$\frac{\Delta R}{R} = G_L\varepsilon_L + G_T\varepsilon_T \tag{2.8}$$

Tab. 2.3: Piezoresistive coefficients for low-doped polysilicon (10^{-11} Pa^{-1}) [Bao2000].

	π'_{11}	π'_{12}	π'_{66}
p-type	58.8	-27.2	85.9
n-type	-45.4	25.0	-70.4

where ε_L and ε_T are the strain components longitudinal and transversal to the resistor. The gauge factors for polysilicon, with G_L typically between 20 and 50 and G_T between -10 and 20 for p-type polysilicon [Nathan1999], are lower than those for monocrystalline silicon, but still far higher than for metal strain gauges.

2.2.4 Thermal Effects

The influence on the resistivity $(\Delta\rho)/\rho_0$ of a material from a temperature change ΔT is, in the first order approximation

$$\frac{\Delta\rho}{\rho_0} = \alpha_1 \Delta T \tag{2.9}$$

where α_1 is the linear temperature coefficient of resistivity (TCR). Values of α_1 for relevant CMOS layer materials are listed in Tab. 2.1.

2.3 Cantilever Mechanics

2.3.1 General Formulas

The microstructures presented in the following chapters are relatively long, thin cantilevers and can be treated as rectangular beams submitted to small deflections and elastic deformation. The stiffness coefficient k of a cantilever beam of length L and Young's modulus E is

$$k = 3 \cdot \frac{EI}{L^3} \tag{2.10}$$

where the area moment of inertia I for a rectangular cantilever is (with z being the distance from the neutral axis to a point in the cross section A)

$$I = \int_A z^2 dA = \frac{wt^3}{12}, \tag{2.11}$$

The stiffness is then a function of its dimensions length L, width w, thickness t and the Young's modulus E of the material [Sarid1994]:

$$k = \frac{Ewt^3}{4L^3} \tag{2.12}$$

The way the stiffness is dependent on the geometry (L, w, t) is important to take into consideration in the design of cantilever sensors.

For some applications the resonant behaviour has to be considered. The fundamental frequency of vibration for a cantilever clamped in one end is [Sarid1994]:

$$\omega = \sqrt{\frac{\kappa^4 \cdot EI}{\rho A}} = \frac{\lambda^2}{\sqrt{3}} \cdot \sqrt{\frac{k}{m}} = \frac{\lambda^2}{2\sqrt{3}} \cdot \frac{t}{L^2} \cdot \sqrt{\frac{\hat{E}}{\rho}} \tag{2.13}$$

where κ is a wave number and $\lambda = \kappa L$ is 1.875 for the first vibrational mode. $\hat{E}$ is the apparent Young's modulus $E/(1-\nu)$ with ν being the Poisson ratio. It can be noted that ω is independent of the width w.

2.4 Deflection by Force on Cantilever End

The sensing element chosen for the AFM cantilever designs in Chapter 4 are integrated piezoresistors. The principal signal to be detected by these cantilevers is the vertical force on the cantilever tip. Therefore, the effect of this force on the stress in the cantilever and the resulting change of resistivity of integrated resistors will be investigated.

2.4.1 Stress Distribution

For the following expressions and simulations, the cantilevers are aligned along the x axis, with the width along the y axis, and thickness along the z axis.

We consider a cantilever beam submitted to a force F along z applied to the cantilever free end. The cantilever will (for a positive force) experience compressive axial stress above its neutral axis and tensile stress below (see Fig. 2.1).

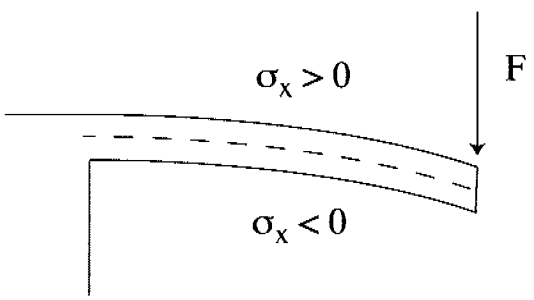

Fig. 2.1: Schematic of a cantilever deflected by a force F on the tip. The stippled line is the neutral axis, where the axial stress σ_x is zero. Above this axis, the axial stress is tensile (positive), and below compressive (negative).

The axial stress σ_x at a distance h from the neutral axis is directly related to the curvature r of the bending beam:

$$\sigma_x = -\frac{hE}{r} \quad \text{with} \quad \frac{1}{r} = \frac{d^2 z}{dx^2} \tag{2.14}$$

$$\sigma_x = \frac{hF}{I}(L-x) = -\frac{12hF}{wt^3}(L-x) \tag{2.15}$$

The magnitude of the stress is decreasing linearly from its maximum at the clamped end towards zero stress at the free end. At any cross-section, the stress is linearly proportional to the distance from the neutral axis, hence with maximums of opposite sign at the top and bottom surface of the cantilever.

The resulting deflection z along the cantilever is

$$z = \frac{FL}{2EI}x^2\left(1 - \frac{x}{3L}\right) = \frac{6FL}{Ewt^3}x^2\left(1 - \frac{x}{3L}\right) \tag{2.16}$$

and the maximum deflection is at the cantilever tip $x = L$:

$$z_{\max} = \frac{FL^3}{3EI} = \frac{4FL^3}{Ewt^3} \tag{2.17}$$

which also can be found by using Eqn. (2.12) and $z_{\max} = F/k$.

Fig. 2.2 shows the calculated axial stress and deflection for a silicon cantilever of dimensions *500 x 85 x 5 μm^3* submitted to a force of 1 nN.

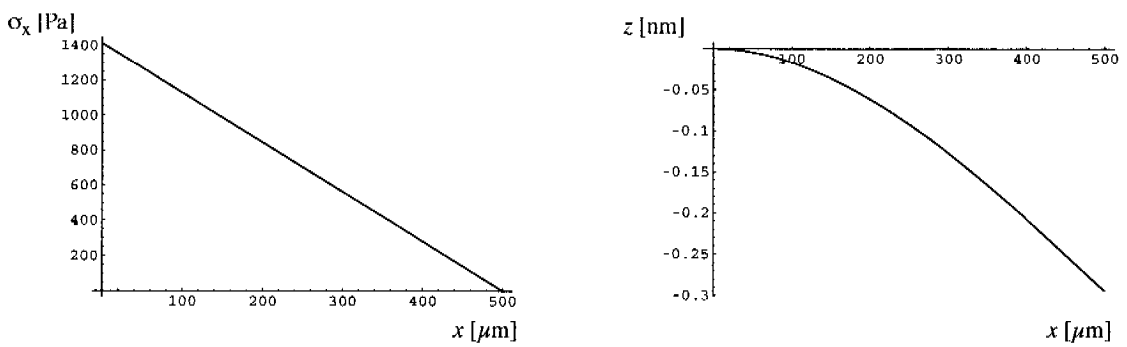

Fig. 2.2: The axial stress σ_x (left) on the cantilever surface and the deflection z (right) along the cantilever axis, calculated using the beam approximation. The cantilever dimensions are 500 x 85 x 5 μm^3, and the force F_z applied to the tip is -1 nN.

The beam approximation used for the above derivations is valid when $w << L$, and for broader cantilevers the analytical calculation is more extensive [Timoshenko1987]. The complexity suggests the application of finite-element analysis tools to estimate the stress distribution and, by comparing to the analytical results, validate the chosen approximations.

2.4.2 Simulated Cantilever Beam

The first simulations will describe an AFM cantilever similar to the designs presented in Chapter 4. The simulations will serve as a support for the design discus-

sion, and in order to validate the chosen approximations, they will also be compared to the analytical expressions in the previous section.

The following simulations were done with the *Ansys* FEM software tool [Ansys2004], using the *SHELL91* shell element (eight-node, six degrees of freedom per node). A Young modulus for silicon of E=160 GPa and a Poisson ratio of ν=0.17 were used. The cantilever dimensions are 500 x 85 x 5 μm^3, and the force F_z applied to the tip is 1 nN. For comparison, Eqn. (2.12) would give an expected stiffness of k = 3.4 N/m, and a tip deflection z = 0.3 nm.

Stress Distribution

The simulation shown in Fig. 2.3 shows the stress component σ_{xx} caused by the force F_z.

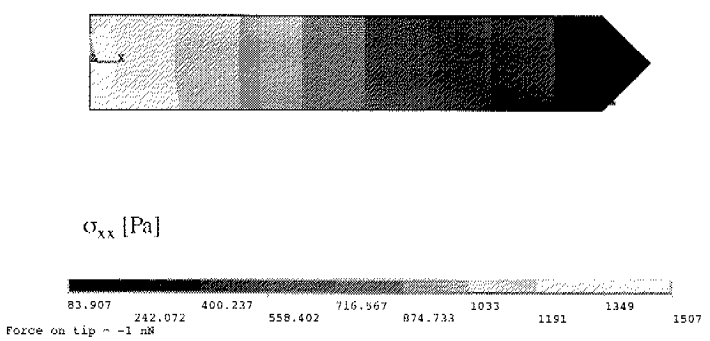

Fig. 2.3: Stress component σ_{xx} caused by a transversal force at the free end, simulated using FEM.

The graph in Fig. 2.4 shows the stress component σ_{xx} along the middle of the cantilever (y=0). The linear slope of the stress curve is well in agreement with Eqn. (2.15). The resulting deflection at the cantilever end is 0.3 nm as expected.

The beam approximation introduced in Section 2.3 neglects any stress σ_{yy} along the y axis (the width of the cantilever). The simulation in Fig. 2.5 shows the component σ_{yy}, which is strongest near the clamped end. Here, the boundary conditions of the clamping (zero displacement in all directions) together with the coupling of the stress in x and y direction through the material's Poisson ratio, influence the transversal stress component σ_{yy}. However, its magnitude is small

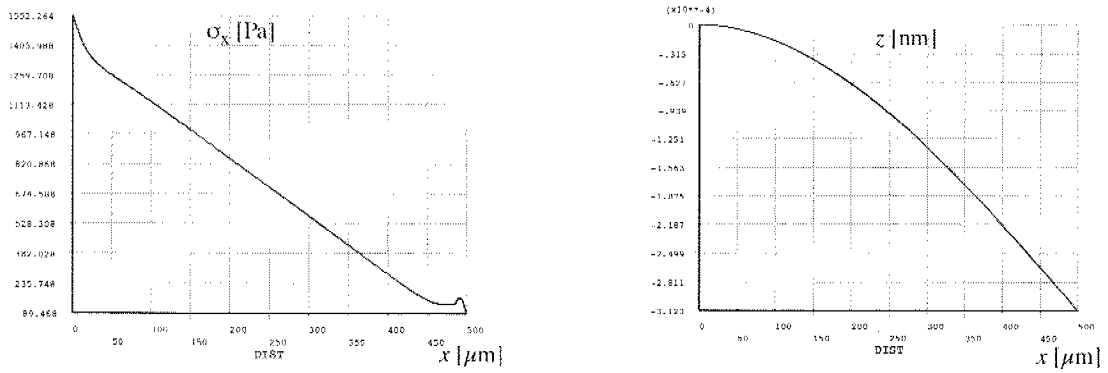

Fig. 2.4: Simulated stress component σ_{xx} (left) and deflection (right) along the middle of the cantilever (y=0). The stress values near both ends of the cantilever deviates from the simplified analytical results in Fig. 2.2 since the simulation includes the boundary conditions in both x and y directions and the corresponding influence of the Poisson ratio.

compared to σ_{xx}, which justifies the beam approximation for a cantilever of these dimensions for most purposes.

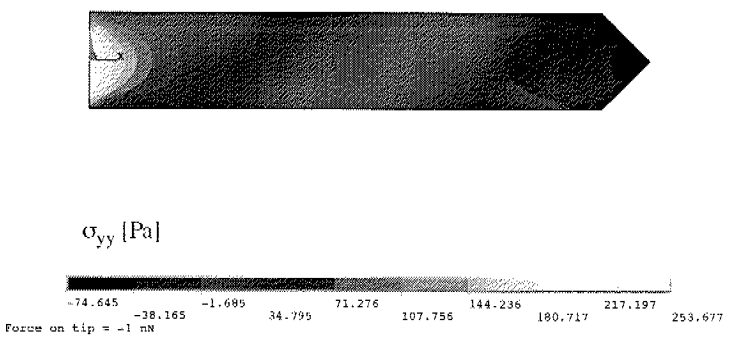

Fig. 2.5: Stress component σ_{yy} caused by a transversal force at the free end.

Resistivity Change Distribution

As seen in Section 2.2, the resistance change of a piezoresistive stress sensor is a function of both the longitudinal and transversal stress relative to the resistor (and current flow) direction. It is therefore interesting not only to look at the isolated stresses in each direction, but also the resulting change of resistivity composed

from both these contributions. The resistor directions considered are respectively parallel and perpendicular to the cantilever axis.

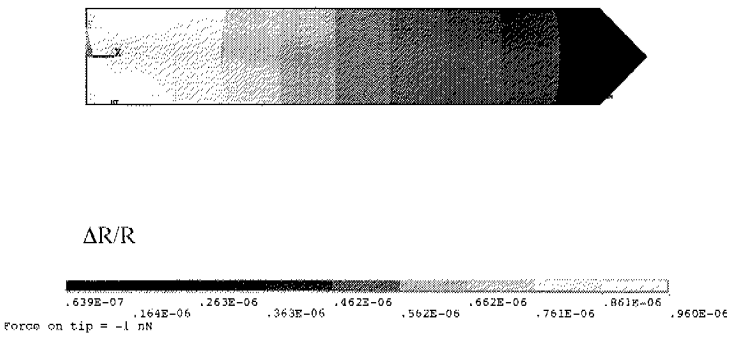

Fig. 2.6: Resistive change, resistor aligned along x axis: $\Delta R/R = \pi_L \sigma_{xx} + \pi_T \sigma_{yy}$

In Fig. 2.6 and Fig. 2.7 the relative change of resistivity is plotted for resistors parallel to the x axis and to the y axis, respectively. The coefficients are those of Tab. 2.2. Compared to the similarly looking distribution of the σ_{xx} stress seen in Fig. 2.3, the influence of σ_{yy} can be seen as small deviations of the isocurves.

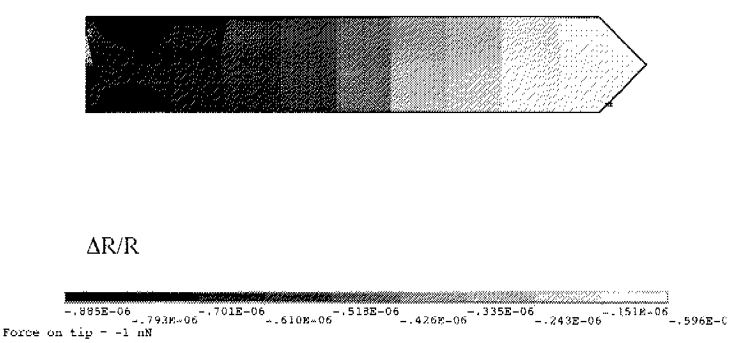

Fig. 2.7: Resistive change, resistor aligned along y axis: $\Delta R/R = \pi_L \sigma_{yy} + \pi_T \sigma_{xx}$

It can be concluded from Fig. 2.6 and Fig. 2.7 that the influence from the width of the cantilever and its clamping does not create large variations in the change of resistivity along its width. There is an increase of sensitivity near the edges of the cantilever, as well as near the clamping, but on the other hand these locations have strong gradients, and the exact positioning of the resistors will therefore be

more delicate at these places, for instance when good matching between resistors is desired.

2.4.3 SIMULATED CANTILEVER PLATE

Cantilevers for detection of surface stress, presented in Chapter 3, will have other form factors than cantilevers for AFM, and in particular, they will be broader. It will be shown in the next section that a distributed surface stress will create a totally different stress field than what results from a concentrated force on the cantilever tip. However, it is still interesting to look at the effect of a concentrated force on these broader cantilevers. First, the simulations will show the effect of the width on the stress field when the assumption $w << L$ no longer is true, and tell if the beam approximation nevertheless can be useful. Secondly, this way of deflecting a cantilever can be a reliable method to characterize the cantilevers mechanically, and the simulations can predict the resistance changes that are occurring in such experiments.

The silicon cantilever plate has dimensions 300 x 300 x 4 μm^3 and the concentrated force applied to the middle of the free edge is F_z = 28 nN. Again a Young modulus for silicon of E=160 GPa and a Poisson ratio of ν=0.17 were used for the simulations. If the beam approximation and Eqn. (2.12) are applied, the stiffness would be k = 28.4 N/m with a resulting maximum deflection of 1.0 nm.

The simulation in Fig. 2.8 (top) shows the resulting stress field. In this case of a square plate cantilever with $w = L$, the influence from the clamping and the resulting concentration of stress is seen more distinctively than in the previous example of a long cantilever. However, the simulated deflection is 1.0 nm, still in good agreement with the beam approximation.

The stress σ_{yy} along the y axis is near the clamped edge up to 1/5 of the stress along the x axis σ_{xx}, corresponding to $\sigma_{yy} \approx -\nu\sigma_{xx}$, but is still very small in the rest of the plate, see Fig. 2.8 (top right). The resulting change in resistivity is shown in Fig. 2.8 (bottom), for resistors aligned parallel and normal to the x axis.

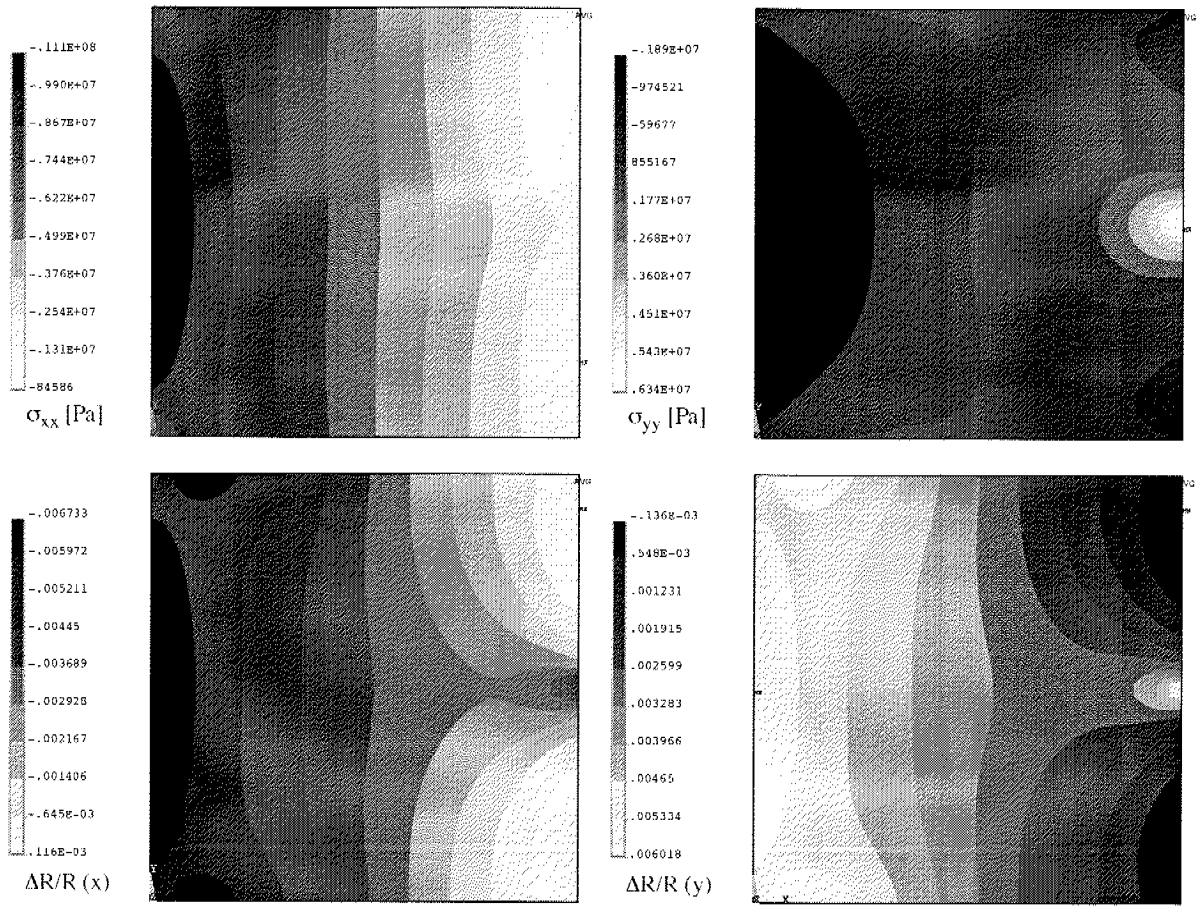

Fig. 2.8: *Stress components σ_{xx} (top left) and σ_{yy} (top right) caused by a transversal, concentrated force $F_z = 28$ nN applied at the free end. (bottom left) Resistive change, resistor aligned along x axis:* $\Delta R/R = \pi_L \sigma_{xx} + \pi_T \sigma_{yy}$ *(bottom right) Resistive change, resistor aligned along y axis:* $\Delta R/R = \pi_L \sigma_{yy} + \pi_T \sigma_{xx}$

2.5 Distributed Surface Stress

2.5.1 Stress Distribution

In order to calculate the resulting stress in a cantilever plate when its surface is modified, for instance, by the binding of a molecular layer, the surface modification will be characterized by the change of surface stress it introduces [Fritz2000, Wu2001].

Surface stress is the reversible work per unit area needed to elastically stretch a pre-existing surface [Cammarata1994], such that for an isotropic surface the surface stress is the scalar $\sigma_s = \gamma + \partial\gamma/\partial\varepsilon$, where γ is the excess, surface free energy density due to the existence of the surface, and ε is the stretching strain. The exact definition of surface stress in the thermodynamic sense is the subject of some ambiguity and controversy [Gutman1995].

In the following, the change of surface stress equals the change of surface free energy density. The surface stress σ_s is seen as the result of a stress σ_d in a thin (compared to the cantilever) layer of thickness t_d on top of a given surface such that $\sigma_s = t_d\sigma_d$. The relation between a surface stress change σ_s and the resulting deflection of a free cantilever is expressed by Stoney's formula [Stoney1909]:

$$\sigma_s = \frac{Et^2}{6R(1-\nu)} \tag{2.18}$$

where R is the radius of curvature of the deflected cantilever. The only geometrical parameter of the cantilever occurring in this expression is the thickness t. Stoney developed this expression studying large metal plates being coated with thin metal films. The relation between surface stress and curvature can be expected to be of local nature, that is, in a first approximation the curvature at one point is only dependent on the surface stress and material properties near this point, as long as the plate is thin and soft enough.

The height deflection z at the end of the cantilever is, for small deflections, equal to $l^2/(2R)$ or

$$z = \frac{3(1-\nu)}{Et^2} l^2 \sigma_s \tag{2.19}$$

The amplitude of the deflection is important in the case of for instance optical read-out like the schemes used for AFM. However, in the case of integrated stress sensors, the deflection at the end of the cantilever is not used for the detection. The surface stress creates a stress distribution in the cantilever, and the resulting average stress in the piezoresistor is detected.

2.5.2 Stress Distribution in the Cantilever Cross-section

The stress distribution inside a beam submitted to surface stress has been treated in the one-dimensional case in [Rasmussen2003, Thaysen2001]. The strain $\varepsilon_x(z)$ at any section of the beam can be expressed as the superposition of the strain component ε_c due to tension/compression along its long axis and a strain component $\varepsilon_b(z)$ due to pure bending:

$$\varepsilon_x(z) = \varepsilon_c + \varepsilon_b(z) \tag{2.20}$$

For a multilayer cantilever where each layer i has thickness t_i and Young modulus E_i, the expression becomes

$$\varepsilon_x(z) = -\frac{\sigma_s}{\sum_i E_i t_i} - \frac{\sigma_s h_T z}{\sum_i E_i t_i \left(\left(h_T - \sum_{j=0}^{i} t_j + \frac{t_i}{2} \right)^2 + \frac{1}{3}\left(\frac{t_i}{2}\right)^2 \right)} \tag{2.21}$$

where h_T is the position of the top layer (relative to the neutral axis).

With a cantilever of non-negligible width, and a surface stress with both x and y components, a two-dimensional treatment is relevant. In the case of $\sigma_{xx} = \sigma_{yy}$ the assumption of a neutral *plane* can be justified and the strain components can be expressed as [Paci2003]

$$\varepsilon_{xx} = \varepsilon_{yy} = \left(-\frac{1}{\sum_i \frac{E_i t_i}{1+\nu_i}} - \frac{3(t - t_s - z_n)}{\sum_i \frac{E_i}{1+\nu_i}((z_i - z_n)^3 - (z_{i-1} - z_n)^3)} (z - z_n) \right) \sigma_s t_s \tag{2.22}$$

where z_i is the location of each layer and z_n is the location of the neutral plane.

These analytical expressions are valid for a position sufficiently far away from the free or clamped edges. Again, a finite-element analysis will show the influence of the boundaries.

2.5.3 Simulated Cantilever Plate

Simulations were done in *Ansys*, with the *SHELL181* shell element (four-node, six degrees of freedom per node) which allows the application of initial stresses. A three-layer sandwich is used in order to model a silicon cantilever with integrated piezoresistors and a functional layer on top. The cantilever dimensions are 300 x 300 x 4 μm^3, with a resistor depth of 500 nm. The initial stress applied to the functional layer of 30 nm thickness is $\sigma_{xx} = \sigma_{yy} = 50$ MPa, corresponding to a surface stress of $\sigma_s = t\sigma = 1.5$ N/m. A Young modulus of E=160 GPa and a Poisson ratio of ν=0.17 were used for all layers. The graphs in Fig. 2.9 show the simulated stress distribution in the resistor layer.

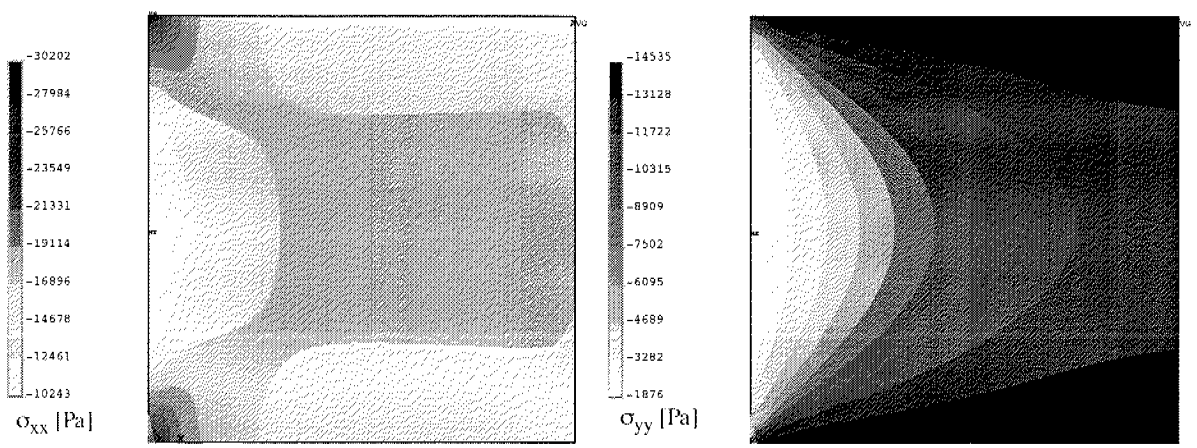

Fig. 2.9: Stress components σ_{xx} (left) and σ_{yy} (right) in resistor layer for a plate subjected to uniform surface stress.

Although the stress applied to the functional layer is uniform, and a free plate as described by Eqns. (2.18–2.22) would have a resulting uniform stress distribution, the simulations illustrate how the boundary conditions influences the stress field. Near the clamped edge, σ_{xx} varies from minimum levels around the centre to the sharply concentrated maximums at the clamped corners, whereas the main parts of the cantilever experience smaller variations. σ_{yy} has its minimum in the centre of the clamped edge, gradually increasing towards the free edges.

The resulting effect on the piezoresistive elements is again determined by the resistor orientation. The change of resistivity for resistors aligned along the x and y axis respectively can be seen in Fig. 2.10. The maximum change is at the corners of the clamped edge. However for the central part of the cantilever, the vari-

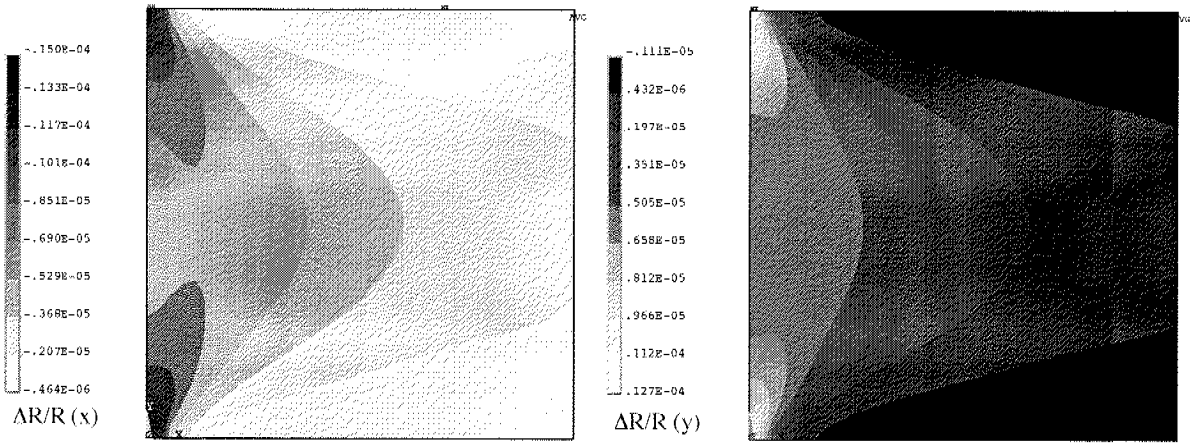

Fig. 2.10: (left) Resistive change, resistor aligned along x axis: $\Delta R/R = \pi_L \sigma_{xx} + \pi_T \sigma_{yy}$ *(right) Resistive change, resistor aligned along y axis:* $\Delta R/R = \pi_L \sigma_{yy} + \pi_T \sigma_{xx}$.

ations are smaller. For resistors aligned along the x axis, the change of resistivity has its maximum magnitude at the clamped edge, steadily decreasing towards the free end, and with greatest reduction towards the side edges. Piezoresistors placed near the clamped edge will therefore have the highest sensitivity to surface stress. However, the strong gradients in these region makes the precise placement of the resistors relative to the cantilever edges important. In the major parts of the cantilever the change is lower, but with a more uniform distribution.

For resistors aligned along the y axis, there is a negative change of resistivity near the two side edges, with the rest of the cantilever experiencing a positive change. There are therefore regions with near zero changes, and a resistor of a given length placed across the zero border can end up with a zero net change of resistance. Such resistor segments should therefore be avoided when sensitivity to surface stress is wanted.

2.6 Signal and Noise

Sensor Performance

A number of parameters characterize the performance of a sensor, such as its resolution, sensitivity, dynamic range, bandwidth, noise level and signal-to-noise

ratio. A commonly referenced benchmark figure is the limit of detection which is the smallest signal that can be distinguished from the background noise, determined by the sensitivity and the background noise level.

The system designs presented in this thesis are composed of sensors integrated with circuity. The sources of the noise can by divided into three groups: the inherent noise of the sensor elements, the inherent noise in the circuitry and instrumentation chain, and finally the external interference that shows up in the signal owing to cross-sensitivities both in sensors and circuitry.

2.6.1 Internal Sensor Noise

The inherent noise sources in a cantilever sensor with piezoresistive read-out are the vibrational noise in the cantilever itself, and the electrical noise in the piezoresistors.

Cantilever Noise

The vibrational noise of a cantilever beam due to the thermal excitation of its vibrational modes and the resulting noise in an integrated piezoresistor has been calculated in [Hansen1999]. For a free cantilever (no force on the free end), the apparent deflection z at the free end is

$$\overline{z^2} = \frac{1}{3} \cdot \frac{k_B T}{k} \cdot \frac{L}{l\left(1 - \frac{l}{2L}\right)^2} \tag{2.23}$$

where l is the length of the piezoresistor, T is the absolute temperature, and k_B is Boltzmann's constant ($1.38 \cdot 10^{-23}$ JK^{-1}). The influence of this noise is greatly reduced by limiting the bandwidth below the fundamental resonance frequency. This will be the case for the surface-stress sensors detecting biological binding, where the expected signal changes are relatively slow, and the bandwidth can be reduced to for instance below 10 Hz. For the AFM systems operating in constant-force mode the bandwidth will also be reduced to well below the resonance frequencies of 25–45 kHz.

Resistor Noise

Thermal noise (Johnson noise) is the random motion of free charge carriers caused by thermal agitation, in the frequency band f_1 to f_2:

$$\overline{v_n^2} = 4k_B TR(f_2 - f_1) \tag{2.24}$$

The noise power $\overline{v_n^2}$ is proportional to the resistance R as well as to the bandwidth, which would encourage smaller resistance values.

Flicker noise (1/f or Hooge noise) in resistors, has a spectral power density inversely proportional to the frequency and to the number of charge carriers N [Wong2003]:

$$\overline{v_n^2} = \frac{\alpha V^2}{N} \log \frac{f_2}{f_1} \tag{2.25}$$

where V is the voltage across the resistor and $\alpha \approx 2 \cdot 10^{-3}$ is a dimension-less constant. The number of charge carriers can be increased by using geometrically large resistors. The driving voltage V, as will be seen later, directly influences the sensitivity of the resistive detection, so choosing its value is a trade-off between low flicker noise and high sensitivity.

Both thermal noise and flicker noise are minimized by narrowing the bandwidth. However, the flicker noise can still be considerable for low frequency ranges where the factor f_2/f_1 is high, even if the bandwidth $f_2 - f_1$ is small.

Temperature Influence

The vibrational noise and the thermal noise are proportional to the absolute temperature. Self-heating of the piezoresistors can therefore increase their influence [Hansen1999]. The power dissipation V^2/R and cooling of the resistors has therefore to be taken into consideration.

2.6.2 Circuitry and System noise

The electronic circuits are also subject to thermal noise and flicker noise, as well as to the shot noise due to the discrete flow of charge carriers across p-n junctions. Because of the complexity of the components and their interconnection, the

resulting noise is not easily calculated by analytic means. However, the same tools used for design of the circuitry often provide the possibility of simulating the performance in term of frequency behaviour and noise level, so that the designs can meet the desired specifications, at least within the accuracy of the simulation, before the final implementation on silicon chips. Although low-noise architectures can reduce the noise, the inherent noise sources impose a fundamental limit to the dynamic range and noise figures of the circuitry.

2.6.3 External Interference

The signals that are read out from the sensors (through the associated circuitry) often show a correlation with additional factors other than the physical effects that originally are desired to be detected. These cross-sensitivities, such as for example temperature and light dependence, are inherent to the sensor and circuitry elements, and must be dealt with by careful design, packaging and instrumental set-up. Some interference can have a random character, other types can be more systematic, for example the day and night temperature variations in a laboratory, or the vibrations from a motor-driven apparatus nearby. A cantilever can be deflected by fluctuations in the surrounding media, for instance by turbulence in a gas or liquid flow, and the corresponding noise is observed in the measured signal. By efficient signal conditioning and acquisition, and by limiting the bandwidth to the minimum range needed, these noise sources can be eliminated if their noise spectrum is outside the useful signal bandwidth. The design of the sensor can also greatly influence how much of the external noise is picked up by the system. As will be seen in the next section, sensor schemes such as Wheatstone bridges can efficiently reduce the effect of certain common-mode noise sources.

2.6.4 Sensor Read-out in Bridge Configurations

There are several ways to detect the change of resistance in a piezoresistor. A single resistor can be submitted to a known voltage or current, and the resulting current respectively voltage can be measured, preferably using a four-wire set-up. Monitoring the resistance change in this way requires a small signal change to be measured against a high background, since $V_{out} = IR(1 + \Delta R/R)$ with usually $\Delta R/R << 1$. This can be improved by connecting the sensing resistor with three resistors of equal value in a Wheatstone bridge configuration as shown in Fig. 2.11a (quarter-bridge). The output voltage of the bridge is now proportional to the relative resistance change, $V_{out} = V \cdot \Delta R/(4R)$. An important result is

that the bridge output is not dependent on the absolute resistance of the resistors. The half-bridge shown in Fig. 2.11b has two sensing resistors in the bridge. The output signal can now be doubled, $V_{out} = V \cdot \Delta R/(2R)$. A full bridge (Fig. 2.11c) has four variable resistors, ideally having two resistors experiencing the opposite resistance change as the two others, yielding $V_{out} = V \cdot \Delta R/R$.

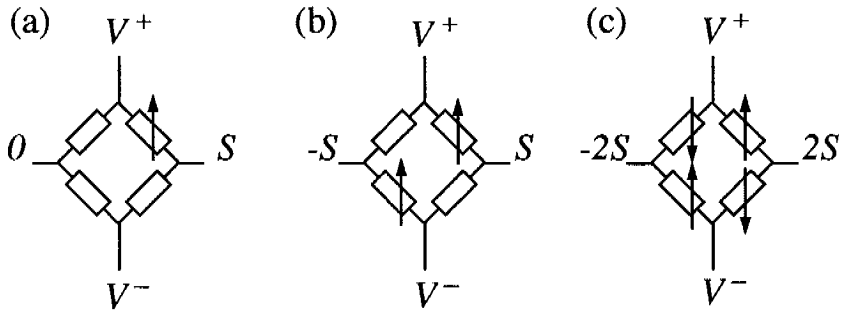

Fig. 2.11: Schematic of different Wheatstone bridge configurations, (a) quarter-bridge, (b) half-bridge, and (c) full-bridge. The bridges are biased with a fixed voltage $V = V^+ - V^-$. The arrow symbolizes a small change ΔR of the resistance R, with a corresponding signal change $S = V \cdot \Delta R/(4R)$. The differential output signals of the bridges are S, $2S$ and $4S$, respectively.

For best linearity and direct amplification, the four resistors should have identical resistance in order to have a zero offset voltage (the output voltage at zero sensor excitation). If the resistors are physically similar with the same response to common-mode disturbances as for example temperature variations, the symmetry of the bridge will also cancel out the common change in resistance. This built-in common-mode rejection applies for all external noise sources that influence the resistors in an uniform way.

In cases where the sensor scheme does not allow a full bridge of sensing resistors, with pair-wise opposite signal, it will still be useful to ensure that the "passive" resistors experience the same environment as the "active" resistors, and serve as reference sensors. The common noise sources will be eliminated, leaving only the difference between the "active" and "passive" sensors to be measured as the output signal. Usage of such reference sensors will be demonstrated in both the presented applications of this thesis.

2.6.5 Resistor Geometry

The depth and resistivity of the resistors are defined by the CMOS process technology and summarized by the *sheet resistance* R_S, where $R = R_S(L/w)$ (see Tab. 2.1 for example values), so that length and width remain the only design parameters to determine.

The resistance of the piezoresistors does not affect the stress sensitivity, but has consequences on power dissipation and thermal noise. The output of the Wheatstone bridge is proportional to the supply voltage, so to obtain high sensitivity, a high supply voltage is desirable. If the application requires low power consumption and minimal self-heating of the sensor, the voltage must be balanced with high enough resistors. Depending on the bandwidth, the thermal noise can then be dominating the final signal-to-noise ratio.

For some applications, smaller sensor size is more important than low power dissipation and short, narrow resistors can be used. The width of a diffused resistor is limited by the design rules of the chosen CMOS process (2 μm for the processes used in this work). For small dimensions, however, the low relative precision can cause sensor output offset.

2.6.6 Sensor Output Offset

The sensor output offset is the dc output from the sensor when no force or stress is applied. This background signal lowers the useable dynamic range of the system and even causes saturation of the amplification chain if its is higher than the input signal range. The offset can also introduce cross-sensitivities to the system by breaking the noise-suppressing symmetry of the sensor bridge. The influence of the sensor offset can be diminished by minimizing its sources in the sensor design, and by integrating offset compensation schemes.

One source of offset in a Wheatstone bridge sensor is the imperfect matching of the resistors due to small variations of geometry and doping. The precision limits of the processing result in lower relative precision for smaller features, which can be important for small-sized resistors (see Tab. 2.4). The matching can be improved by using wider and longer resistors when possible.

A more important offset source is the variations of the residual stress seen by the piezoresistors. The built-in stress in the CMOS processed wafer is relatively uniform over its surface, however during the postprocessing steps, when the thin silicon membranes are formed and later shaped into cantilevers, stress is released

Tab. 2.4: Mismatch between the four p^+ diffusion resistors in a Wheatstone bridge, measured on unetched chips (no micromachining).

Dimensions L x w (μm^2)	Estimated resistance (Ω)	Measured mean ± st.var. (Ω)	Relative deviation between resistors
1000 x 20	2000	2085 ± 2.3	0.1%
45 x 2.0	900	899 ± 7.2	0.8%

according to the new geometry. This often results in a visible deflection of the released cantilevers. The piezoresistors located on a cantilever will experience different deformation and stress depending on their location and consequently have different resistance (see Fig. 2.12). The resulting offset can be minimized by

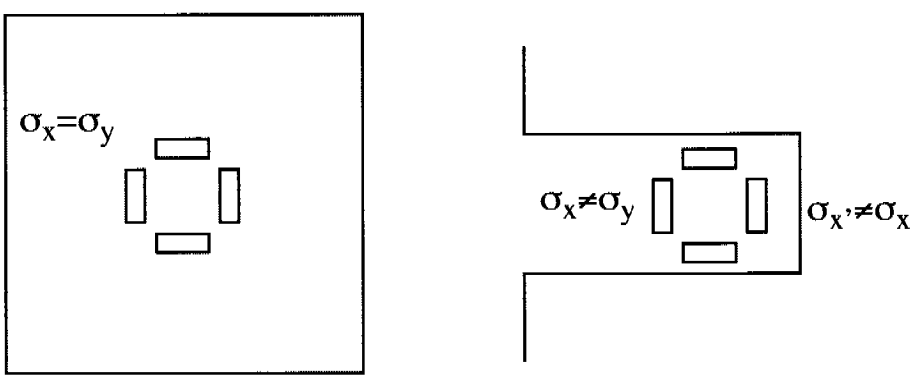

Fig. 2.12: Schematic of piezoresistive bridge before (left) and after (right) micromachining. For a wafer of sufficient size, the built-in surface layer stress can be considered symmetric and uniform over all resistors. After the release of mechanical structures, the stress in a resistor depends on the orientation and proximity of the silicon edges.

relocation of the resistors, but since the working principle of the sensor often relies on resistor location and geometry, some offset has to be accepted in order to provide the wanted sensitivity.

The exact magnitude of the offset is not easily predicted and is seen to vary from process to process as well as between chips from different wafers of the same process. The presented systems in the following chapters therefore include sev-

eral offset compensation schemes and are designed to cope with a wide offset range.

2.7 General Fabrication and Processing

The cantilever sensors are fabricated in an out-sourced industrial CMOS process followed by in-house wafer-level micro-machining. The processes used are double-metal CMOS processes on 100-mm wafers from austria*micro*systems, Austria. Some of the characterized AFM devices use a high-voltage, 2.0-μm process (CBT) and the remainder uses a low-voltage 0.8-μm process (CYE).

Cantilever shape and structures are defined in the CMOS process by taking advantage of suitable CMOS layers (n-well silicon, aluminium, dielectrics). Also, piezoresistive sensing elements and bimorph actuation elements are formed at the CMOS foundry. The mechanical structures, i.e. the cantilevers, are then released in the post-process micromachining steps. After dicing, the chips are mounted on dedicated printed circuit boards or in dual-in-line (DIL) packages and are electrically connected using wire bonding.

2.7.1 Design and Foundry Processing

The design of the devices together with the complete circuitry is performed with the CAD tool Cadence [Cadence]. All chip designs for one processing run are assembled into a single reticle design, which is shipped to the CMOS foundry; chips for different projects typically share one reticle (see Fig. 2.13a).

At the foundry, a full CMOS process is performed using stepper-based lithography. The only modification of the standard process is the creation of a wafer-scale metal network to provide electrical biasing of the wafer during the post-CMOS anisotropic etching with electro-chemical etch-stop (see Fig. 2.13b). The wafers are also ground and polished on the backside to a reduced thickness of 380 μm in order to shorten the necessary etch time in the post-processing. The polishing prepares the back surface for the deposition of the silicon nitride etch mask, also deposited by the foundry. After the full, standard CMOS process is completed, the finished wafers are sent back from the foundry ready for post-processing.

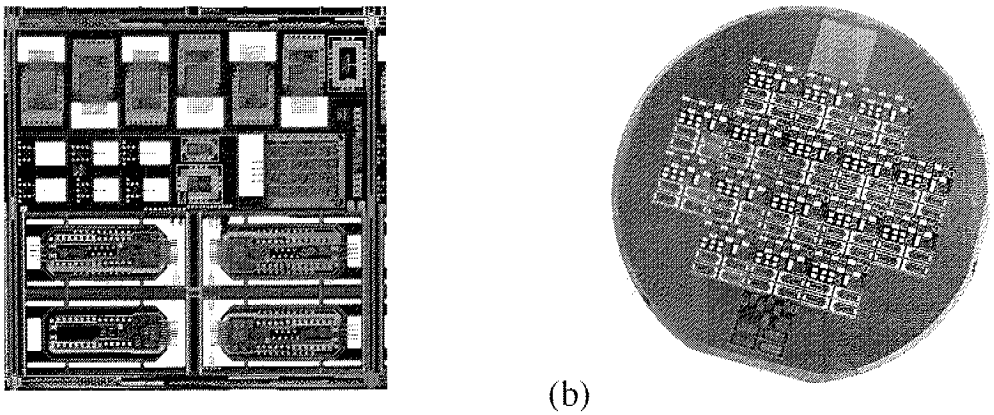

(a) (b)

Fig. 2.13: (a) A CMOS design reticle, 15 mm x 15 mm. (b) The complete wafer has a diameter of 100 mm and contains 16 reticles. The contacts for biasing the n-well and p-substrate during backside etching are seen above the reticles.

2.7.2 Post-CMOS Processing

Backside Etch

In order to create silicon membranes from which cantilevers can be shaped, an anisotropic wet etch is performed from the backside of the wafer [Müller2000]. First, the openings in the silicon nitride etch mask are defined with reactive-ion etching (RIE). Because of the anisotropic nature of the KOH etching of silicon, the walls of the etched cavities have an angle of 54° with the surface. The size of the etch mask openings must therefore be calculated as a function of the wafer thickness and the desired membrane size.

A 6-molar KOH solution at 90°C is used as etchant together with a four-electrode electro-chemical etch-stop (ECE) technique [Kloeck1989]. The ECE technique assures reliable and reproducible fabrication of thin silicon membranes. This is achieved by reverse-biasing the junction between the n-well and the p-substrate, and keeping the n-well at a higher potential than the KOH solution (passivation potential). The p-substrate is held at a negative (etching) potential, so that the etch continues through the p-substrate until it stops at the n-well.

The final thickness of the membrane is defined by the junction depth of the n-well. The high-voltage process provides two different n-well depths at 4 μm and 7 μm, whereas the normal low-voltage process only has a 3.5 μm n-well.

Additional reactive-ion etching of silicon can afterwards be used on the backside of the wafers to further thin the membranes, if the desired thickness is less than the n-well depth.

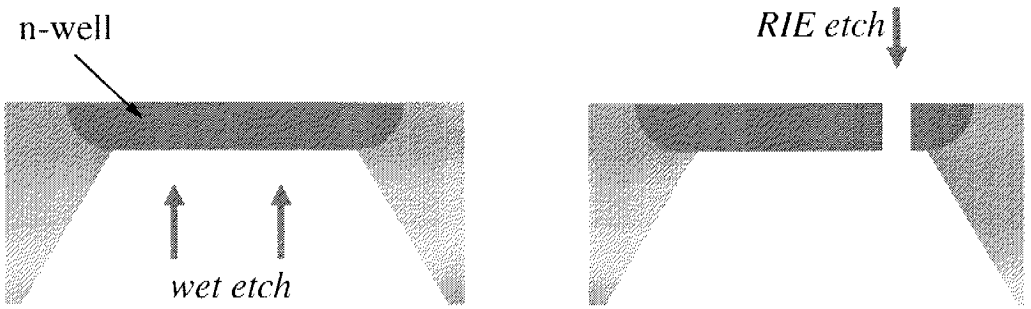

Fig. 2.14: Post-processing steps: Formation of silicon membranes using a backside wet etch stopped at the n-well (left). Release of the cantilevers using front-side, reactive-ion etching (right).

CANTILEVER RELEASE

To release free-standing cantilevers, the remaining layers of the membrane have to be removed around the cantilevers. The nitride passivation layer that usually covers most of the wafer area, as well as some of the oxide layers, have already been opened in the CMOS process. However, some oxide from the CMOS process can not be removed in the process itself, and has to be removed in the post-processing in order to expose the underlying silicon. The oxide etch can be performed by front side reactive-ion etching with CF_4 and CHF_3 (typically 40 nm/min) or wet etching, using an etch mask of photoresist.

Finally, the silicon membrane is etched using reactive-ion etching with SF_6 and CHF_3 (typically 500 nm/min), where a photoresist mask defines the silicon structures to be kept as cantilevers. Fig. 2.14 shows a schematic of the most important post-processing steps.

2.7.3 DICING

Dicing of the wafers into individual chips can be harmful to the fabricated cantilevers, which will easily break under the pressure of the water jet used in the dicing saw. Minimising the water flow is not a good solution, since it increases particle contamination and blade wear. A special process sequence was therefore

developed to enhance the yield through the post-processing and dicing. Before the final release of the cantilevers (the membranes are already formed), a protective layer of photoresist is spun on the wafer backside. Slow spinning is used to obtain a thick layer of approximately 10 μm. This way, the cantilevers are supported by the photoresist layer after their release from the front side. The backside coating has the additional advantage that the wafer is not perforated during the cantilever release. This allows for a subsequent front-side spinning process for further protection of the micromechanical structures. A second thick photoresist layer is spun on from the front-side to fully encapsulate the cantilevers in photoresist before the dicing process (see Fig. 2.15), which can be done with full water jet pressure.

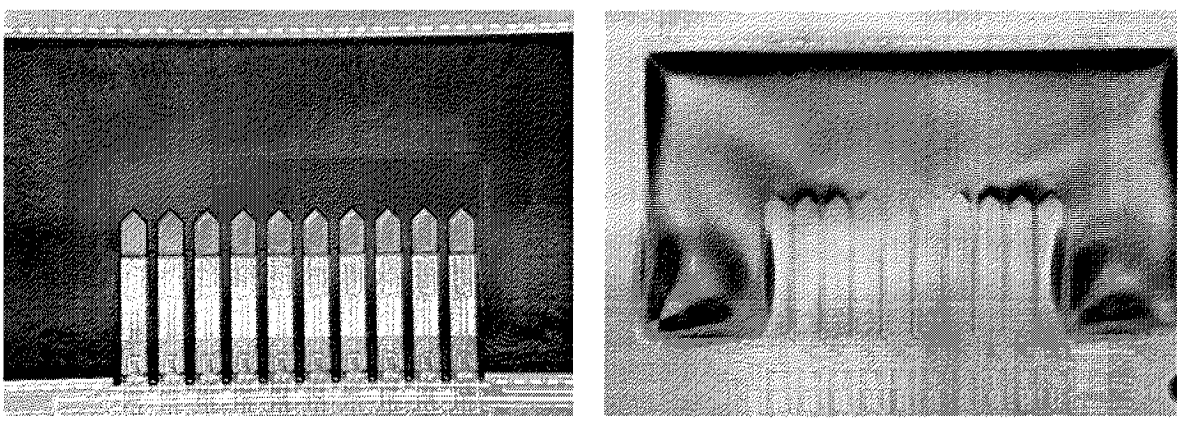

Fig. 2.15: (left) During the RIE silicon membrane cut, the released cantilevers are supported by the backside photoresist coating. (right) After a second spin coating of photoresist on the front side, the cantilever array is totally embedded in photoresist.

In addition to supporting the cantilevers, the photoresist layer also protects the chips from dicing debris. This is important since the finished chips can not undergo the relative strong cleaning that usually is performed to clean away particle contamination. For instance, use of ultrasound cleaning would break the cantilevers.

The photoresist is easily removed from the final chips with acetone or another suitable photoresist remover. For smaller and fragile elements, the photoresist can also be stripped with an oxygen plasma asher. This protection method proved to be very efficient for membranes and cantilevers of any size, typically with 100% yield during the dicing phase.

3 CANTILEVER-BASED BIOSENSOR ARRAYS

3.1 INTRODUCTION

The sensor system presented in this chapter is part of a portable instrument under development for point-of-care testing to determine specific protein levels in body fluids.[1] In the following, contributions to sensor and electronic design, packaging, surface chemistry and biochemical research are discussed.

3.1.1 BIOSENSORS

Biosensors are devices that can detect highly specific interactions between biological molecules. They are generally composed of a biological element and a physicochemical detector. Biological reactions can be influenced by low concentrations of biomolecules, and biosensors can therefore be very sensitive. The advances in medicine and biochemistry over the last decades have dramatically increased our understanding of how biomolecules interact and how their presence and concentration govern physiological processes. Both for research and for medical diagnosis and treatment there is a demand for precise, sensitive detection of biomolecules.

In modern health care, sample analysis is often carried out in centralized laboratories. Although the analysis can be automated to a large degree, preparation of samples, long detection sequences, logistics and administration result in a long response time. This is in particular not satisfactory for emergency situations where rapid diagnosis can decide between life and death. On the other hand, near-patient or point-of-care testing is considered to provide better quality of service to the patient and save costs. There is therefore a growing interest in small, inexpensive, easy-to-use diagnosis tools to be used by a general practitioner or even by the patient himself. This drives the need for integrated systems,

1. Part of the work was done within the EU-project Biofinger (http://www.biofinger.org).

where sample preparation, detection, visualization and communication of results are combined in one instrument.

3.1.2 Detection Methods

Biosensors are often based on the binding between antibodies and their corresponding protein (antigen). The antigen will very specifically bind to the antibody, while other proteins are not affected. Similarly, DNA- or RNA-sensors use the specific binding to matching complimentary strands of these molecule chains. Sensors are made by immobilizing the receptor molecule (i.e. an antibody) and detecting the binding of the analyte in question (i.e. the antigen) using a physicochemical technique.

Typical biosensors on the market today are based on a fluorescent techniques, where a biochemically active receptor is modified with a fluorescent marker in order to produce an optical signal in the presence of a specific analyte. This includes the enzyme-linked immunosorbent assay (ELISA) technique, which is the dominant method for detecting specific proteins.

A more recent approach – currently still in the research stage – is the use of micro- or nanomechanical structures to detect the binding between an immobilized receptor and the matching analyte. Cantilever beams have been shown to deflect when their surface properties are changed by binding events [Fritz2000]. This is interpreted as a change of surface-stress of the cantilever, related to the new composition of the surface layer. Sterical hindrance of large, densely packed molecules is one of the mechanisms responsible for the stress change. As seen in Chapter 2, a surface-stress change induces a bending of the cantilever and a stress in the cantilever material.

Optical read-out of cantilever deflection is, due to its high sensitivity and use of existing AFM equipment, popular in this research field. However, the read-out can be affected both by the opacity and the refractive index of the liquid samples. The laser beam can also heat the cantilever and cause parasitic deflection [Chen1995]. The optical read-out is technically difficult to scale to large cantilever arrays, which would allow the simultaneous detection of multiple analytes [Alvarez2005, Battiston2001].

Piezoresistive read-out, on the other hand, is well suited for cantilever arrays and compact systems where the sensor is integrated with electronic circuitry as well as for microfluidic total analysis systems (μTAS) [Thaysen2001].

3.2 SENSOR DESIGN

The goal of the sensor design is the detection of surface-stress changes associated with surface binding of biomolecules. The major design considerations are:

- sensitivity
- system integration
- robust operation
- reproducible manufacturing

The design uses a standard CMOS process as a starting point in order to easily integrate the sensor with electronics on a silicon chip.

3.2.1 CANTILEVER GEOMETRY

Due to its well-defined mechanical properties, crystalline silicon is chosen as the main cantilever material, which also allows the implantation of piezoresistors in the CMOS process. The use of an electrochemical etch stop in the postprocessing provides an initial silicon thickness of 3.5 μm with the possibility of additional RIE thinning.

The length and width of the cantilever are 300 μm, which is almost 100 times the thickness of the silicon layer. Since the surface-stress change to be detected is in principle isotropic and uniform over the functionalized surface, the lateral size and shape of the cantilever does not directly influence the sensitivity of the sensor. This is in contrast to similar sensors based on optical read-out which measure the tip deflection of the cantilever. The tip deflection is quadratic to the length of the cantilever for a small, uniform bending, and therefore long cantilevers are usually preferred for optical read-out schemes. Using integrated sensors, the bending moment caused by the surface stress is directly and locally affecting the piezoresistors. The distribution of the active area also means that the width does not have the same significance as in detection of concentrated forces (as seen in for example AFM applications), since the surface-stress change is constant over the active surface area and independent on the width. However, the length and width must be sufficiently large to reduce the influence from the free and clamped edges.

3.2.2 Layer Stack and Protection

Since the sensors are designed for use in comparatively harsh environments (at least for CMOS electronics), such as physiological solutions, the sensor elements at the surface of the silicon must be protected. However, the protection layers separate the functionalization layer from the sensing piezoresistive layer and decrease the sensitivity of the sensor system. They should therefore be as thin as possible while still providing sufficient protection.

The CMOS process provides several silicon dioxide layers that can be left on top of the cantilever, as well as the final silicon nitride passivation, especially engineered for protection of the chip circuitry. Although the silicon nitride layer would give sufficient protection, the process flow does not allow for the removal of all the oxides without degrading the piezoresistive layer. Therefore, a sandwich of thermally grown field oxide and deposited (CVD) oxides is left on the cantilever after the CMOS process (see Fig. 3.1). The thickness of the silicon dioxide layers is 1.6 μm on top of a diffusion layer and 2.1 μm elsewhere. The silicon nitride layer is 1.0 μm thick.

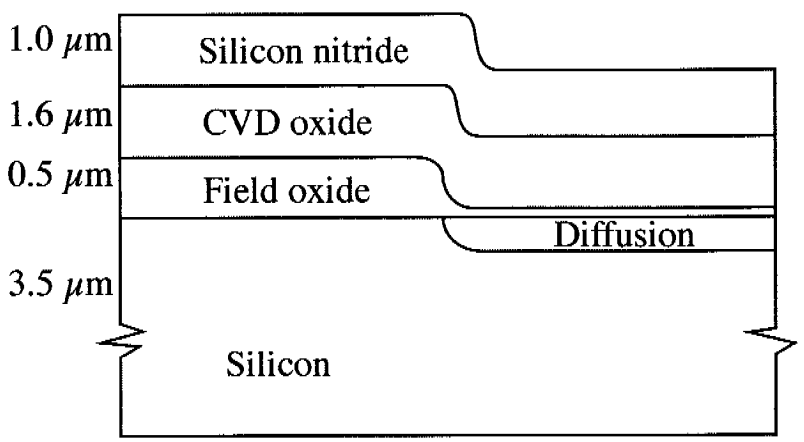

Fig. 3.1: Cross section of a cantilever (not to scale). The right part contains a diffused resistor, with a reduced thickness of the oxide layers.

3.2.3 Resistor Geometry

As a stress in the piezoresistive layer causes a relative change of resistivity, the absolute resistance does not directly influence the sensitivity. As seen in the sim-

ulations in Section 2.5.3, the stress field has only distinct concentration regions close to the clamped edge. Due to the uncertainty of the edge location after the micromachining, these regions are not ideal for placing the resistors. A part from the contributions from the free and clamped edges, there is in principal no preferred placement that would enhance the sensitivity by exibiting substantially higher stress values.

However, the resistor design greatly affects the internal noise contribution. The thermal noise power is proportional to the resistance and to the signal bandwidth, suggesting the use of a small resistance. However, since the bandwidth of the targeted signals is narrow (from 1 mHz to 1 Hz), the thermal noise is not dominant. The flicker noise, on the other hand, becomes important for low frequency measurements, with a spectral density inversely proportional to the frequency and the total number of charge carriers in the resistor (Eqn. (2.25)). The resistor volume should therefore be as large as possible in order to maximize the number of carriers.

A large enough resistance is also required to avoid self-heating of the sensor and to match the input stage of the amplifying circuitry. The sensors were therefore designed with 10 kΩ resistors, yielding a power dissipation of 2.5 mW per resistor for a bridge voltage supply of 5 V. With the ratio between width and length given by the targeted resistance R and the sheet resistance R_S, the resistor is laid out in a meander structure to cover as much as possible of the available area. This minimizes the flicker noise and averages the sensor output over the largest part of the cantilever. The p^+ diffusion used for the resistors has a sheet resistance of 40 Ω. With 300 μm x 300 μm cantilever plates and two resistors on each cantilever, a resistor length of 2130 μm was obtained using a width of 8.5 μm.

The simulations in Section 2.5.3 show how the clamping of the cantilever plate alters the stress distribution in the sensing layer, resulting in a larger stress change parallel to the cantilever axis. The resistors are therefore mainly aligned along the cantilever axis.

3.3 Chip Design

3.3.1 Sensor Array

The sensor chips feature an array of cantilever sensors together with signal conditioning and interface circuitry. Four cantilevers, equally spaced with a pitch of

500 μm, are located along one side of the chip in order to simplify the packaging. The cantilever array offers different measurement configurations; all cantilevers can be individually functionalized to detect different analytes. Alternatively, one or more cantilevers can act as a reference sensor by being functionalized to not bind analytes and thus provide a way to discriminate non-specific binding and other parasitic signals. Different configurations of the piezoresistive Wheatstone bridges have been fabricated and evaluated.

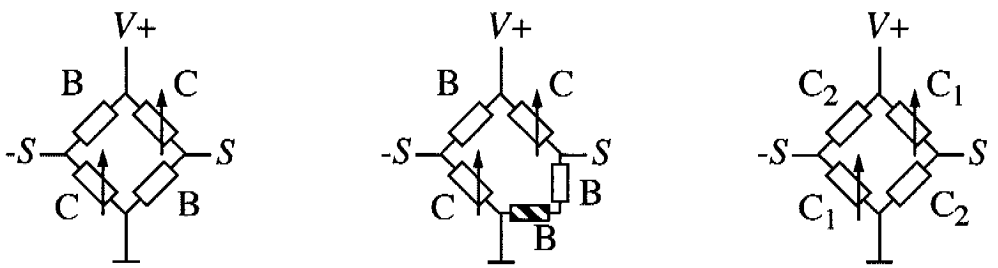

Fig. 3.2: Wheatstone bridge configurations: (a) Half-bridge: two resistors on the cantilever C, two on the bulk B. (b) Half-bridge with resistive offset compensation added to the bulk resistors. (c) Dual cantilever: two resistors on cantilever C_1, two on C_2.

HALF-BRIDGE

Two identical resistors on the same cantilever show the same signal response and are used as the active resistors in a half-bridge. Two matching resistors on the chip bulk constitute the passive parts of the Wheatstone bridge (see Fig. 3.2a).

HALF-BRIDGE WITH IN-BRIDGE OFFSET COMPENSATION

Although the four resistors are designed to be identical, the release process of the cantilevers induces a stress change in the resistors which results in an offset voltage from the bridge. To be able to compensate for this, one of the bulk resistors is designed with a lower nominal value and is connected in series with a low-noise transistor acting as a variable resistance (see Fig. 3.2b). The bias voltage for the transistor is provided through a bias filter (consisting of a chain of 20 switched-capacitor stages) with a cut-off frequency of 10 Hz and is used to balance the bridge for minimal offset.

DUAL-CANTILEVER SYMMETRIC BRIDGE

To enhance the symmetry of the four resistors in the bridge, two cantilevers, each with two resistors, are used to form one Wheatstone bridge (see Fig. 3.2c). One cantilever is functionalized to be the active sensing cantilever and the other one serves as a reference cantilever. Placed on otherwise identical cantilevers, the resistors are well matched, resulting in a minimal offset voltage. Common-mode signals affecting both cantilevers are directly cancelled out by the bridge design.

Fig. 3.3 shows a close-up of the sensor array of a sensor chip. This chip features one cantilever in half-bridge configuration with in-bridge offset compensation, one cantilever configured as half-bridge and two cantilevers forming a dual-cantilever configuration.

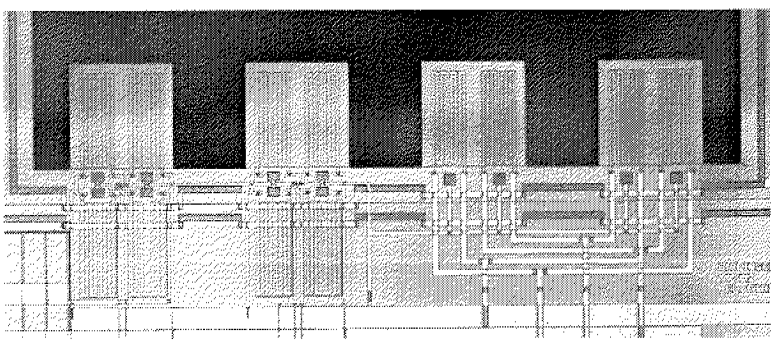

Fig. 3.3: Photograph of a fabricated sensor array. The chip has three different sensor configurations: (from left) half-bridge with resistive offset compensation, half-bridge configuration, and paired sensing and reference cantilever using a dual cantilever symmetric bridge.

3.3.2 ELECTRONIC BLOCKS

The electronic circuitry is designed for high-gain amplification of the sensor output signal, while maintaining low noise characteristics and the possibility of compensation of sensor offset. Two circuit versions were designed, one "high-offset" design that would allow sensor offset signals up to 200 mV, and a "low-offset" design for sensor offsets up to 5 mV. A block diagram of the circuitry on the "low-offset" chip is shown in Fig. 3.4.

The five-channel input multiplexer selects the differential signal from one of the Wheatstone bridges and feeds it to the input amplifier. A test input can also be

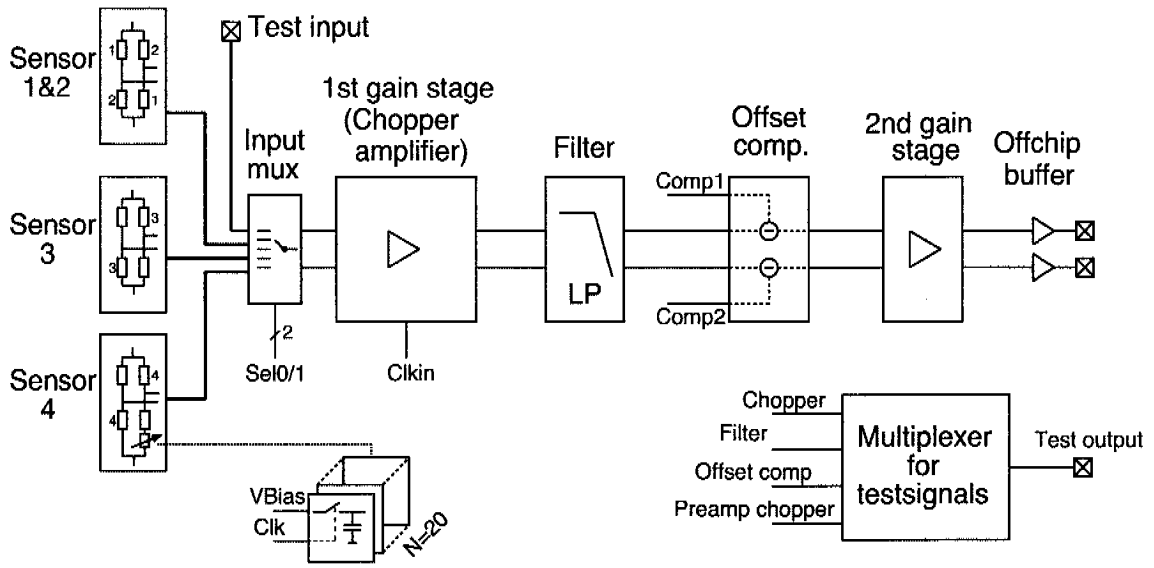

Fig. 3.4: Block diagram of the "low-offset" design. Sensor array, multiplexer, amplifiers and filters are integrated on a single chip. The whole signal chain is fully differential.

chosen, so that instead of a sensor, a differential signal provided through input pads can be used for testing and characterization of the circuitry. The serial resistance of the multiplexer switches is 2 kΩ, negligible compared to the input resistance of the amplifier, and does not affect the sensitivity.

The first gain stage is a low-noise chopper amplifier operating at a frequency of 4 kHz. The gain can be selected between 20 and 100. The use of a band-pass filter reduces the residual offset of the amplifier. The clock signal for the chopping is provided externally to the chip. The chopper stage is followed by a second-order low-pass filter with a cut-off frequency of 500 Hz.

An offset-compensation stage allows the adjustment of the offset by an external differential voltage supplied to the chip. The second amplifier stage has a selectable gain of 13 or 26. The output buffer provides a low-impedance output with the capability of driving a capacitive load of up to 10 nF. The chip output signal is differential with a maximum range of ±2.5 V. The bias voltage for the Wheatstone bridges is supplied through separate pads that are not connected to other circuitry and can be adjusted independently of the normal 5 V chip supply voltage.

The fabricated chip (after postprocessing, before packaging) is shown in Fig. 3.5.

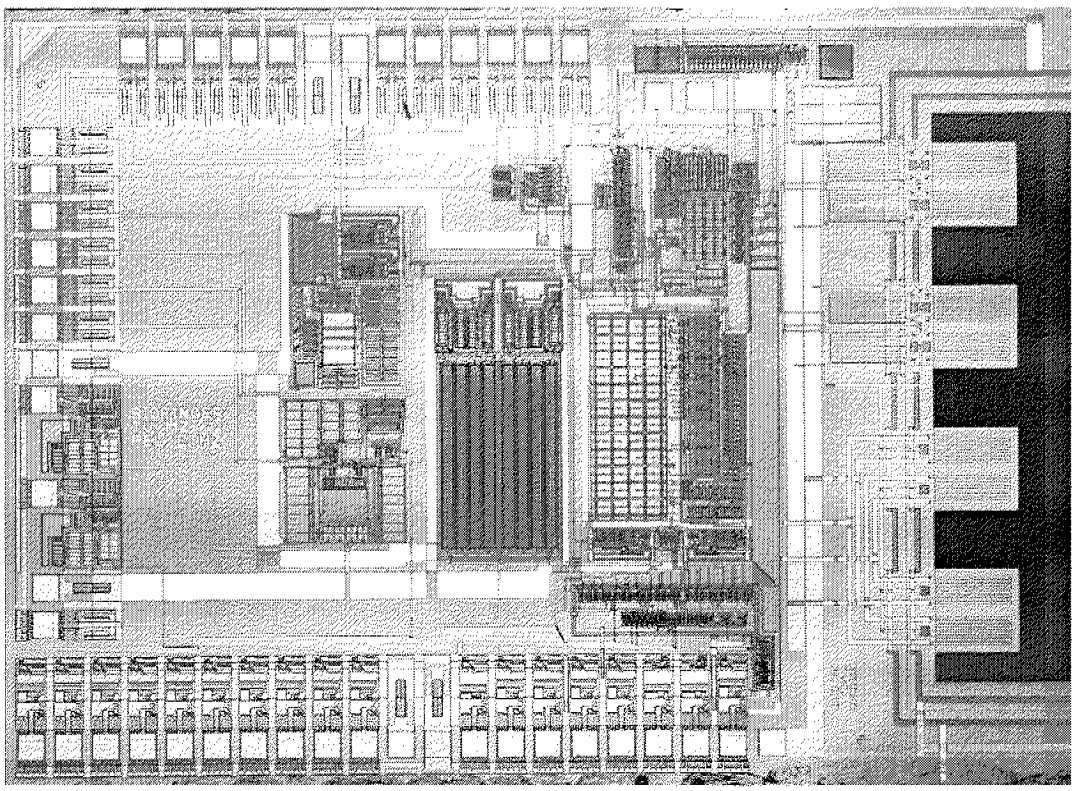

Fig. 3.5: Micrograph of the fabricated sensor chip ("low-offset" design). The chip measures 3.9 mm x 2.7 mm. The four cantilevers on the right side have dimensions of 300 µm x 300 µm.

The total chip size is 3.9 mm x 2.7 mm including silicon lugs on each side of the four-cantilever array.

The second, "high-offset" design features two half-bridge cantilevers and two half-bridge cantilevers with in-bridge offset compensation. The chopper amplifier on this chip has a gain of 20 and is followed by a second gain stage of 4 or 16 and a third gain stage of 4 or 8.

3.4 System and Packaging

The packaging of the sensor chip is an important aspect for the operation of the sensor system. As for any electronic chip, it must provide electrical connections and mechanical protection. It must also allow the exposure of the sensor to the analytes while protecting the electronic circuitry from the cleaning, functionalization and analyte solutions.

3.4.1 Liquid Cell

Both for testing and for the final application, it is desirable to consume only small amounts of analyte solution in each assay. This implies a small liquid chamber around the cantilever sensors. The small volume also reduces the average diffusion time in the chamber, which for diffusion-limited processes results in faster equilibrium times. Since one of the project goals is to package the chip in a disposable unit, the manufacturing costs should be low.

A microfluidic packaging concept was chosen to integrate a microchamber and capillary in- and outlets for the analyte solution. An advantage of microfluidic systems is the low Reynolds number, meaning the liquid flow is mainly laminar with no turbulence. Bubbles are less likely trapped in the channels and the fluids are easily replaced without mixing, which is important for cleaning and functionalization sequences. Typical microfluidic technology also allows integration of added functionality in the package, and the use of inexpensive materials and fabrication technologies.

The packaging solution chosen in this work is shown in Fig. 3.6 [Song2005]. The structural material is polydimethylsiloxane (PDMS), a silicone elastomer with low permeability to water, low electrical conductivity, and good optical transparency. Two PDMS plates are stacked on top of each other with the chip placed in a recess in the lower plate. The microchamber around the cantilevers has a volume of 1.75 μL. In- and outlet channels are structured in the PDMS and allow for thin fused-silica capillary tubes to be inserted and connected with standard laboratory fittings to a fluidic pump set-up. The total dead volume including the channels is 4.5 μL.

The plates are fabricated by casting of the commercially available PDMS (Sylgard 184 from Dow Corning) in a metal mould. The chip is inserted into the bottom plate which is placed on a small printed circuit board (PCB). After wire

bonding between the chip and the PCB, the second PDMS plate is added, closing the liquid chamber. An epoxy-based protection material (Hysol FP4460 from Loctite) is then dispensed around the package to seal any open gaps and to protect the rest of the chip and the bond wires.

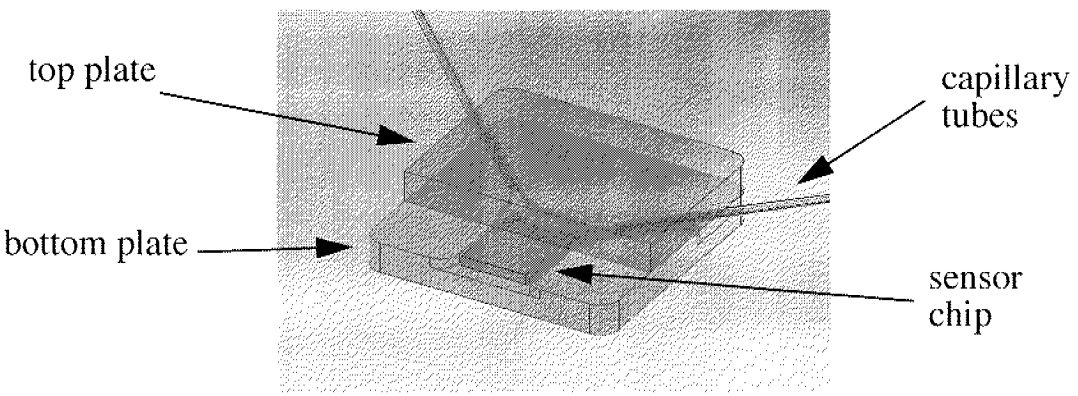

Fig. 3.6: The PDMS-based, microfluidic packaging of the sensor chip. The bottom plate measures 10 mm x 10 mm. The volume of the microchamber around the cantilevers is 1.75 µL. (Drawing courtesy of W.H.Song)

3.4.2 The Plug-in Cassette and Hand-held Unit

To avoid contamination across samples and to limit the need for on-site cleaning and functionalization procedures, the cantilever sensors are part of a small, disposable unit. The unit is plugged into a base unit containing the necessary off-chip electronics for acquisition and storage, including user interface and external communication.

For integration with the hand-held base unit, the disposable sensor PCB is designed according to the industry standard PCMCIA specification with a board size of 85.6 mm x 54 mm and a 68-pin electrical connector. The prototype of the base unit contains power supplies for the chip and a microcontroller-based communication and control unit. An LCD display visualizes the measurement data as it is recorded, and the stored data can be transferred to a computer over the serial interface.

3.5 SURFACE FUNCTIONALIZATION

The functionalization of the sensor surface is a critical part of the sensor system. It determines to which analytes the sensors are sensitive and also how well the analyte concentration translates into a change of surface stress. The functionalized surface should show a high binding affinity to the analyte with minimum non-specific binding. At the same time it should allow a high density of bound analytes on the surface in order to obtain a measurable influence on the surface stress.

The functionalization procedure involves the cleaning and physical preparation of the sensor surface, the immobilization of the biochemically selective receptor, such as an antibody, and finally the rinsing of excess or non-bound receptors.

3.5.1 SURFACE IMMOBILIZATION TECHNIQUES

Different immobilization techniques have been considered for the cantilever functionalization: silanization, thiol linkage, and protein-A binding.

Silanization involves linking of silanes to the oxidized surface, onto which antibodies bind, either directly or via a cross-linker. The result is a monolayer of antibodies; however, their orientation is random and only a fraction of the antibodies are biochemically active [Perrin1997].

Thiol-linkage uses the affinity of the thiol's sulphur-termination to gold, which results in a self-assembled monolayer of thiols onto which the antibodies can bind. The oriented antibodies have a high biochemical activity [Davies1994].

Protein-A (a coat protein extracted from the *Staphylococcus aureus* bacteria) binds easily to any support, and although its own orientation is not well-defined, the antibodies that in turn bind to the protein-A show a directivity which is favourable for subsequent antigen binding [Schramm1987].

For multi-analyte detection and reference cantilever operation, localized functionalization is needed. One strategy is to prepare the cantilever surfaces differently during the manufacturing with the help of layers from the CMOS process or by wafer-level photolithography during the post-processing. A functionalization process can then be applied on all cantilevers together, for instance inside the liquid cell, with the selective binding of the receptor molecules to the different surfaces governing the patterning.

Another option is the localization of the functionalization products by physical confinement of the liquids, for instance with a microfluidic tool dispensing onto each individual cantilever. This method has been tested on flat gold substrates but has not yet been transferred to cantilever chips.

Selective gold patterning of the cantilevers can easily be done on the processed CMOS wafers and is suited for thiol linkage in particular. Also, other potential receptors show a significantly different binding affinity between gold and silicon oxide or nitride surfaces. The binding density of an anti-PSA antibody was shown to be 10 times higher on gold than on silicon nitride.[1] The sensing cantilevers were therefore prepared with a gold surface, while the reference cantilevers are nitride coated.

3.5.2 Gold Deposition and Patterning

Gold patterning is performed on the CMOS wafers as part of the post-processing sequence (see Fig. 3.7). Since the wafer is considerably more fragile after the

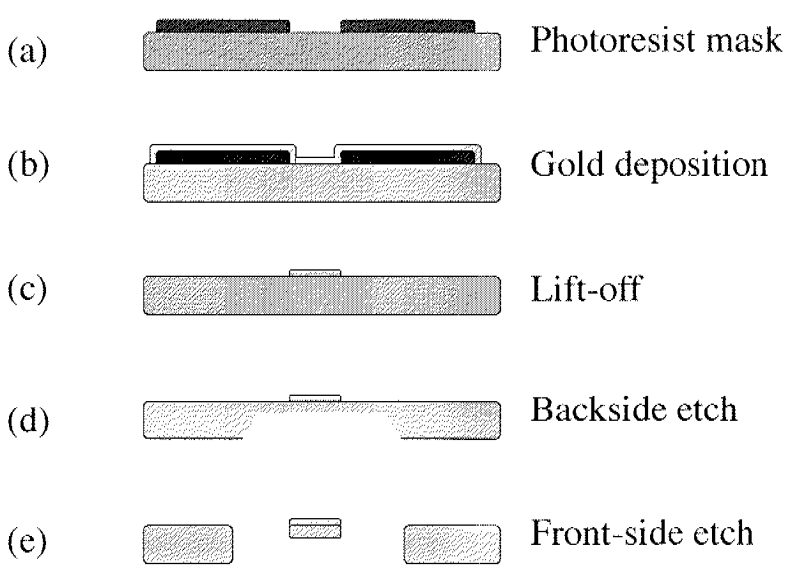

Fig. 3.7: The gold deposition and patterning on the cantilevers. (a) Photoresist is spun on and patterned. (b) Gold is evaporated. (c) Lift-off. (d) Backside silicon etch. (e) Front-side silicon etch (cantilever release).

1. M.Crowley, Cork University Hospital, Ireland, private communication.

backside bulk etching, the gold deposition is done before this etch step. However, in order to minimize wear on the gold surface, as many of the preparatory steps as possible are performed first, e.g. the dry etch opening of the backside nitride mask and the front-side, oxide-removal dry etch.

A lift-off technique is used to pattern the gold. First, a dedicated lift-off resist (LOR-7B, MicroChem, USA) is deposited. A normal, positive photoresist is then spun on top. The UV exposure in the mask aligner patterns the normal photoresist, but not the lift-off resist. The developer solution will, however, isotropically etch into the lift-off resist, creating a re-entrant profile that causes a discontinuity in the deposited metal layer. The discontinuity ensures clean and well-defined edges.

A 3-nm-thick layer of chromium is first applied to improve the adhesion of the gold. For the actual gold deposition, gold sputtering (150–200 nm) or gold evaporation (150 nm) was used.

After the gold deposition, the wafer is immersed in an dedicated remover solution (Remover PG, Microchem, USA) for several hours until the photoresist is dissolved completely, leaving the gold in place only where it is directly in contact with the nitride (or oxide) surface. Fig. 3.8 shows a pair of cantilevers, where one cantilever has been gold-coated.

3.5.3 Cleaning

A thorough cleaning of the surfaces is necessary for all immobilization experiments. Generally, strong etchants are used, such as piranha solution (sulphuric acid or ammonium hydroxide, and hydrogen peroxide) or aqua regia (hydrochloric acid and nitric acid). These products are not only dangerous to work with, they also degrade some sensor and packaging materials. Other, less aggressive cleaning methods were therefore investigated.

After dicing of the wafers, the chips are immersed in acetone to remove the photoresist layers which were applied to protect the cantilevers during this process (see Section 2.7.3). They are then rinsed with isopropanol and deionized (DI) water. The water is blown away with a nitrogen gun. An oxygen plasma asher (200 W for 3 minutes) is used to remove any organic residues. After packaging, the cleaning must be performed through the capillary tubes. As a standard procedure, a sequence of acetone, isopropanol and deionized water is pumped through the microchamber.

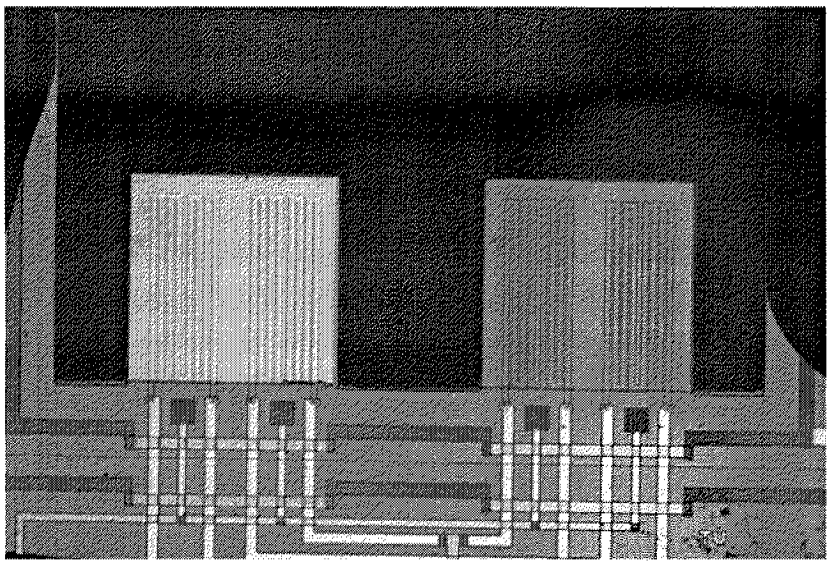

Fig. 3.8: Close-up photograph of a cantilever pair. The left cantilever has been coated with gold, while the right one is left uncoated to act as a reference cantilever for unspecific binding and common-mode signals.

For the binding experiments, chemical cleaning for 2 minutes with diluted (10 mM) hydrochloric acid (HCl) or sodium hydroxide (NaOH) was used prior to the immobilization step. Deionized water was used to wash away the cleaning chemicals. After repeated use of these cleaning agents, the chips would sometimes fail, probably due to leakage in the protection layers and packaging. The life-time of the chips was observed to be longer using NaOH instead of HCl.

Other techniques, for instance ozone cleaning, have been shown to be highly efficient on regular substrates. However, it has not yet been studied whether these methods can also be applied to packaged chips.

3.5.4 Activation and Rinsing

For packaged chips, the immobilization of the biomolecular receptor onto the sensor surface is performed by pumping the agent solution through the chamber. Phosphate-buffered saline (PBS) solution is used as solvent for the receptor. Prior to the receptor solution, pure PBS is injected to stabilize the system. PBS is also used after immobilization to rinse away excess, non-bound receptor molecules. The complete functionalization procedure is summarized in Tab. 3.1.

Tab. 3.1: Functionalization procedure. The "agent" contains the receptor molecules, for instance protein-A, thiols or anti-bodies.

Purpose	Product	Time (min)
Remove organic residues and contamination	Acetone	1
	Isopropanol	2
	DI-water	1
Clean surface	NaOH or HCl	2
	DI-water	10
Stabilize	PBS	2
Immobilization	Agent+PBS	30
Flush	PBS	2
	DI-water	2

3.6 CHARACTERIZATION

The final goal of this sensor is the detection of biomolecules, and the sensor system has been optimized for this application. Since the signal levels in a typical biomolecular binding experiment are small and strongly dependent on a variety of experimental factors, surface chemistry preparation being one important example, this type of experiments is not optimal for the systematic evaluation of the sensors. Practical considerations of a multi-party project with parallel development also lead to the need for, e.g. testing of the sensors and electronics before the functionalization process has been fully established and is ready for exploitation. The system and its different components have therefore been characterized by a variety of non-biological methods, namely electrical, mechanical and chemical methods.

In the first place, a qualification of the signal conditioning chain of the on-chip circuitry is important, to verify the amplification gain, frequency range and noise level. Only with the knowledge of the characteristics of the circuitry connected to

the sensors can the output signals from the chip be correctly interpreted and related to the original sensor signals.

3.6.1 Electrical Characterization

The sensors and electronic circuitry are tightly integrated on the chip and can not be taken apart. There are however ways to decouple the sensors in order to measure the circuitry part on its own. The input multiplexers provide a channel for an external, differential signal to be fed to the input amplifiers. The response of the circuitry to an injected test signal can therefore be characterized in terms of gain and frequency response. Stand-alone sensors are also tested, with an alternative instrumentation path and external amplification. In this case the advantages of the single-chip integration are not exploited and, for instance, the longer non-amplified signal path leads to the introduction of additional noise.

Sensor Offset

The offset voltage from the Wheatstone bridges could be measured directly on test structures without on-chip circuitry. For dual-cantilever configurations the offset was 1–3 mV at 5 V bias, which is within the specifications of the "low-offset" circuitry design (5 mV). The offset of the circuitry-integrated sensors was found by measuring the needed compensation voltage to balance the amplifier output. The offset of the half-bridge configuration was 25±5 mV, well within the range of the "high-offset" design (200 mV). The in-bridge compensation configuration was functional, however, this configuration was susceptible to low-frequency fluctuations and light sensitivity. The focus was therefore set on the dual-cantilever configuration, allowing for higher gain and exhibiting less drift.

Sensor Noise

A stand-alone sensor equivalent to the dual-cantilever bridge on the "low-offset" chip was studied with a dynamic signal analyser (Hewlett Packard 3562A). The output of the sensor bridge was amplified by an instrumentation amplifier (Burr-Brown INA110) at a gain of 500 to obtain sufficient signal levels for the analyser. The noise-power density spectrum in the frequency range 0.1 Hz to 10 kHz is shown in Fig. 3.9a.

In order to estimate the noise from the sensors only, the measurement was repeated with the amplifier only (inputs short-circuited) and the difference between both data sets was calculated (see Fig. 3.9b).

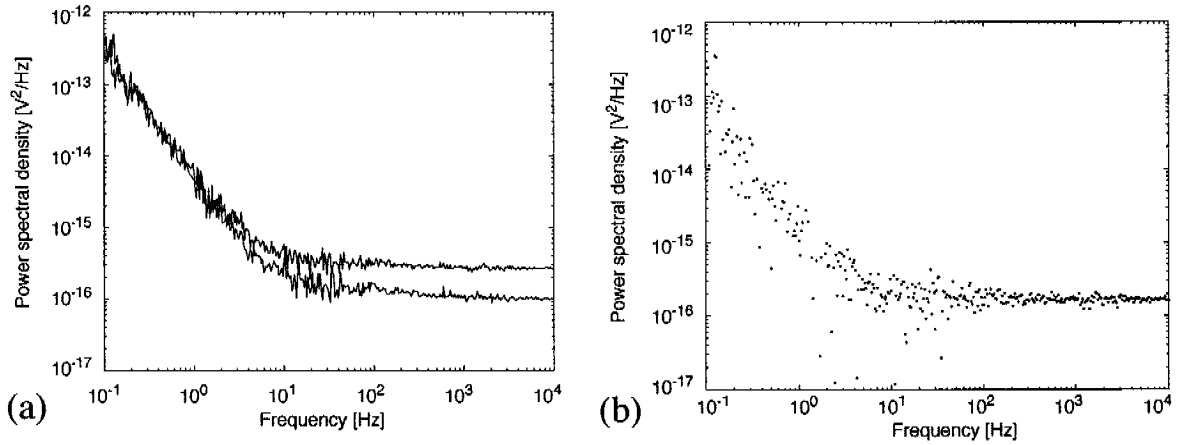

Fig. 3.9: *(a) Noise spectrum from a dual-cantilever sensor bridge including the preamplifier (upper curve) compared to the preamplifier alone (lower curve). The data are input-referred noise spectral power densities. The specified thermal noise of the amplifier is $1 \cdot 10^{-16}$ V^2/Hz, which coincides with the high-frequency asymptote of the lower curve. (b) Calculated difference between the measurements in (a). The difference at low frequency (dominated by the 1/f-noise) is small, and some calculated data points are negative and do not appear in the logarithmic plot. The high-frequency values around $2 \cdot 10^{-16}$ V^2/Hz are consistent with the expected thermal noise of the sensor resistors, $1.7 \cdot 10^{-16}$ V^2/Hz.*

At high frequency, where the thermal noise is dominant, the input-referred noise of the amplifier only is measured to be $1 \cdot 10^{-16}$ V^2/Hz, which is in agreement with the specifications of the amplifier. The calculated noise of the sensors at high frequency, around $2 \cdot 10^{-16}$ V^2/Hz, are consistent with the expected thermal noise of the sensor resistors, $1.7 \cdot 10^{-16}$ V^2/Hz, calculated from the resistance of 10 kΩ.

The 1/f-noise, seen at lower frequencies, is dominated by the amplifier, and the substraction from nearly equal signals does not allow a conclusive analysis. The expected 1/f-noise spectral density for the resistors at 0.1 Hz, using Eqn. (2.25), is $2.5 \cdot 10^{-15}$ V^2/Hz, which is far below the noise levels of the amplifier at this frequency.

ON-CHIP AMPLIFIER

The on-chip circuitry was characterized with the help of the test inputs and outputs. The total gains are 49, 55, 61 and 67 dB for the "low-offset" design and 50, 56, 62 and 68 dB for the "high-offset" chip. The bandwidth is 460 Hz. The noise level of the on-chip amplifying chain was measured with the dynamic signal analyser. The measurements were repeated with chopping disabled in the preamplifier in order to evaluate its performance (see Tab. 3.2).

Tab. 3.2: Measured noise levels of the amplifier chain in the "high-offset" chip. The noise is 2–3 times lower when enabling the chopper amplifier. The total gain was 2500 (highest setting).

	Chopped (10 kHz)		Not chopped	
	Output	Input referred	Output	Input referred
50 mHz-10 Hz	1.1 mV	0.43 μV	4.1 mV	1.6 μV
50 mHz-1 kHz	2.8 mV	1.1 μV	6.0 mV	2.3 μV
50 mHz-5 kHz	3.1 mV	1.2 μV	6.1 mV	2.4 μV

3.6.2 MECHANICAL DEFLECTION

A common way of characterising AFM cantilevers with integrated deflection sensors is to deflect the cantilever with a force on its tip, usually in order to obtain a known deflection z, and measure the corresponding sensor output V. The stiffness k is easily calculated from resonance frequency measurements since, as seen in Eqn. (2.13), the resonance frequency is a function of the stiffness and the mass only. The mass, or equivalent mass in the case of non-rectangular cantilevers, is calculated from dimensions and material density. The applied force is then found with $F = k \cdot z$, and a sensitivity S in terms of sensor output per applied force can be calculated,

$$S = \frac{V}{F} = \frac{V}{kz}$$

This method can also be applied to the surface-stress sensors. However, it is important to keep in mind that the force distribution is different to the one caused by a surface-stress change, and the resulting sensitivity S does not directly translate into a measure of the surface-stress sensing capabilities. As seen in Eqn. (2.15) and Section 2.4.3, the stress in this case is approximately linear along the cantilever axis, and the average value which is detected by the distributed piezoresistors is half of the maximum value near the clamped edge. The measured signals can be compared to results from FEM simulations as in Section 2.4.3.

Deflection Sensitivity

Deflection measurements were performed with the help of a piezoelectric actuator (piezotube). The cantilever chips were glued to small printed circuit boards, which were mounted on a custom-made metal holder to fit into the scanning stage of a commercial AFM system (Multimode MMAFM-2, Veeco Instruments Inc.). On top of the piezotube, where for AFM operation the sample to scan is located, a small wedge made from anisotropic etched silicon was placed. The cantilever was then positioned to touch down with its outer edge on the wedge (see Fig. 3.10). By actuating the piezotube in z-direction, an almost vertical force could then be exerted on the contact point of the cantilever edge.

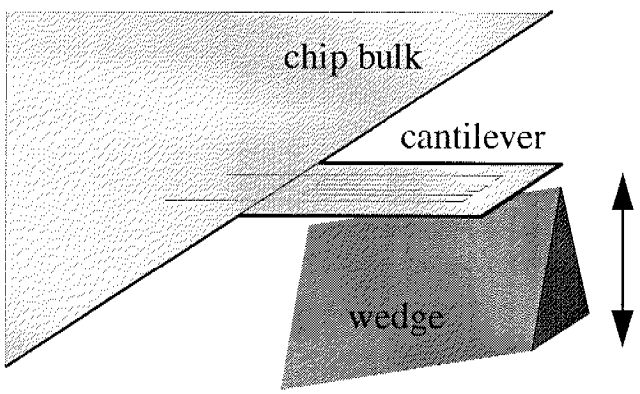

Fig. 3.10: Schematic of the mechanical deflection measurement. The cantilever is bent by a punctual force on its free end applied by the wedge, which is moved vertically by the piezotube. The silicon wedge is fabricated using anisotropic etching.

The z-actuation was controlled by the AFM software, which permits low-frequency, triangular ramping or manual stepping of the z-position. The output volt-

age from the sensor Wheatstone bridge was recorded and related to the deflection. Fig. 3.11 shows the linear response of the sensor to deflection amplitudes up to 1 μm. The sensitivity is 0.74 μV/nm/V.

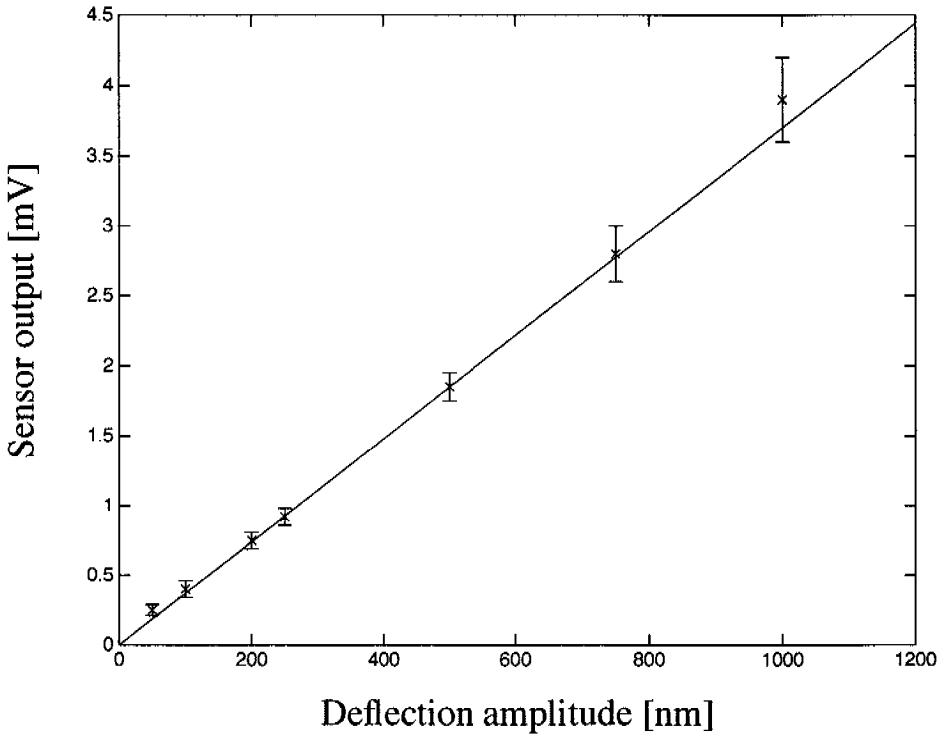

Fig. 3.11: Sensor output (with 5 V bridge bias) as a function of the deflection amplitude for a test sensor (no integrated electronics). The linear approximation (solid line) has a slope of 3.7 μV/nm, equivalent to a deflection sensitivity of 0.74 μV/nm/V.

As seen in Fig. 3.12a, deflections down to a few nanometer are clearly detectable. However, the low-frequent drift, attributed to instabilities of the mechanical set-up, is in the order of 0.1 nm/s. All displacements in the relatively long mechanical chain (glued cantilever chip, screwed PCB and clamped metal holder in addition to the AFM piezotube) influence the signal. Another error source is the creep of the piezotube as seen in the step response of Fig. 3.12b.

Noise measurements on a non-touching cantilever indicated a noise-level of 3 μV, with a resulting detection limit of 2 nm (three times RMS noise) at 5 V bias.

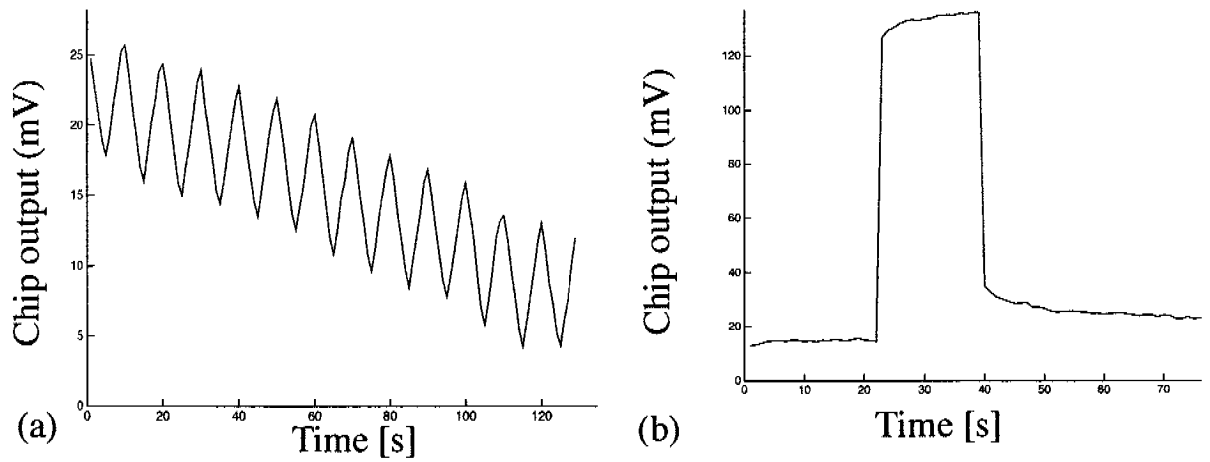

Fig. 3.12: (a) Amplified sensor response to mechanical deflection (ramping of 10 nm at 0.1 Hz). The signal drift is caused by the mechanical set-up. (b) Amplified sensor response to mechanical deflection of the cantilever. The step corresponds to a 100 nm deflection of 20 seconds duration. The sampling frequency was 1 Hz. The creep and drift observed are attributed to the piezotube acting on the cantilever. The "hi-offset" chip used for these experiments had a gain of 320 and a bridge bias of 5 V.

3.6.3 Humidity Measurements

In order to reproducibly generate a distributed surface stress, polymer coatings have been studied as test system. The humidity-induced swelling of polymers has been investigated by [Buchhold1998, Boltshauser1993] for the development of humidity sensors. Silicon membranes were coated with polyimide and the stress in the membranes was correlated to changes of the ambient humidity.

The same effect can be applied to cantilever sensors [Jensenius2002]. The expansion of the polymer can be expected to create the equivalent to a surface-stress change on the cantilever. This is therefore a way to evaluate the sensors in an operational concept close to the targeted surface-binding experiments, but with less uncertainties in terms of signal response caused by biochemical factors and thus better reproducibility. A known expansion can be used to quantify the surface-stress sensitivity of the sensor. Finally, different sensor designs can be compared directly if the polymer layers are identical.

HUMIDITY CYCLING

The measuring cantilever was drop-coated with photoresist (Shipley S1818) as sensitive layer, while the reference cantilever was kept uncoated. The estimated layer thickness was 20 μm. The photoresist was cured in an oven at 100°C for 30 minutes. The humidity cycling was performed in a climate chamber (SB-305, Weiss Umwelttechnik, Reiskirchen, Germany). A Labview (National Instruments) program on an external computer controlled the humidity and temperature settings of the climate chamber. The temperature was kept constant and was verified by the internal temperature sensor of the chamber (precision ±0.1 K). The cantilever sensor was a test structure without on-chip electronics. The sensor output together with the chamber humidity is shown in Fig. 3.13.

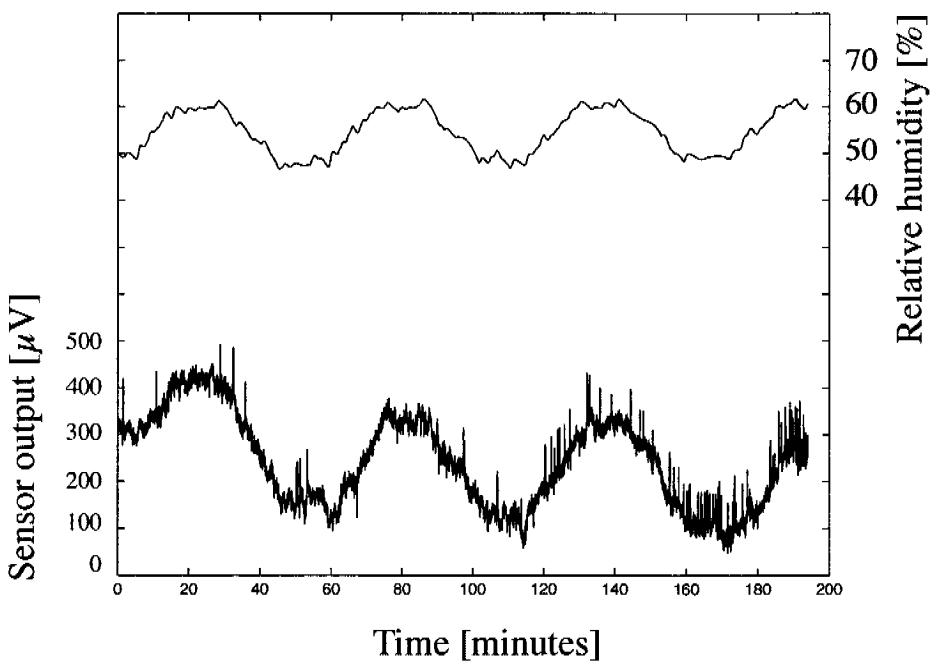

Fig. 3.13: Cantilever coated with photoresist submitted to humidity cycling. Voltage output from the sensor Wheatstone bridge (lower curve) and measured humidity using a commercial sensor (upper curve). The humidity is cycled between 50% and 60% with a period of 57 minutes (step up 1% per 90 s, flat 900 s, step down 1% per 90 s, flat 900 s). An offset calibration was performed before the measurement started.

In Fig. 3.14, the sensor output signal is plotted against the measured humidity for multiple cycles between 30% to 80% relative humidity. The graph shows the lin-

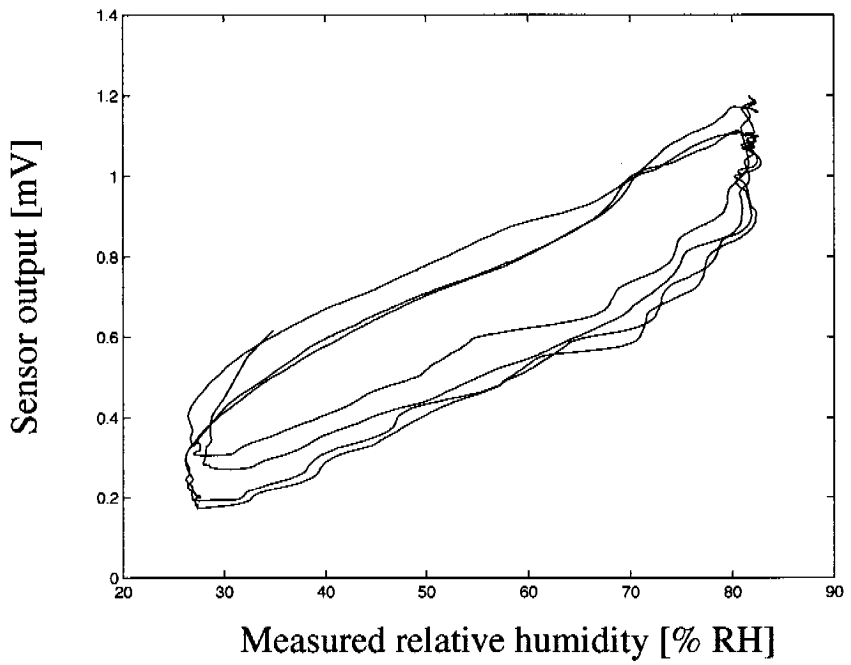

Fig. 3.14: Sensor output plotted against the measured humidity during three cycles between 30 and 80% RH. The sensor output has been low-pass filtered (moving average of 100 samples at a sample rate of 1 Hz) in order to better distinguish each cycle. The humidity change rate was 0.67%/min.

earity of the humidity response, but also reveals a hysteresis caused by the absorption and desorption rate of the humidity in the photoresist layer. The sensitivity is 18 μV/% RH, with a limit of detection of 1.5 % RH (at three times RMS noise).

Temperature Cycling

With the same climate chamber, the sensors were also submitted to temperature cycling, while the relative humidity was kept constant. A graph of the sensor output together with the temperature is shown in Fig. 3.15. The sensitivity to temperature is 110 μV/K. The response to temperature is not immediate, but shows a

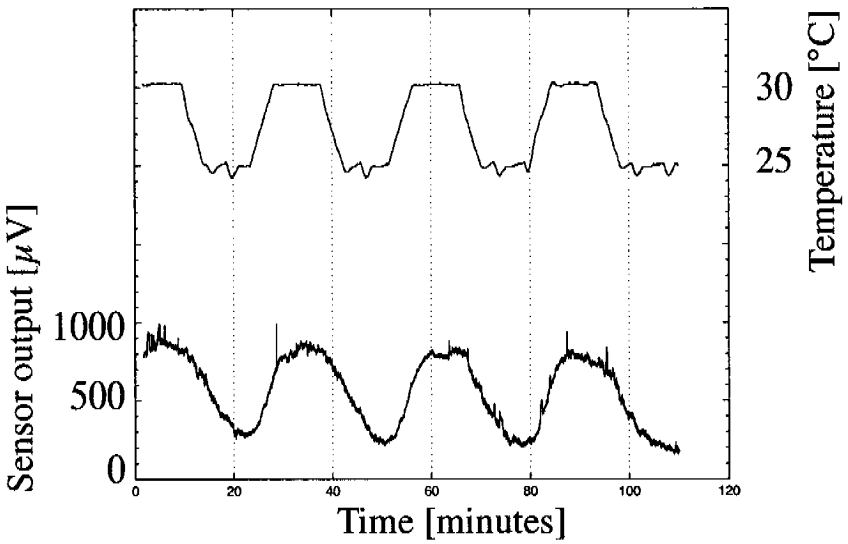

Fig. 3.15: Sensor output voltage and reference temperature inside the climate chamber as a function of time, while cycling the chamber temperature between 25 and 30 °C. The relative humidity was kept constant at 50% RH.

non-negligible stabilization time. This can partly be explained by the thermal mass of the climate chamber. Another factor is the temperature-dependent partition coefficient of humidity in the polymer. As the temperature changes, the humidity in the polymer is driven towards a new equilibrium with the surrounding humidity and the resulting change of humidity inside the polymer is detected by the sensor, in addition to the effect of the thermal expansion of the polymer.

3.6.4 Volatile-Organic-Compound Detection

Analyte absorption in a polymer layer has been used in several ways to achieve the detection of volatile organic compounds. Physical properties of the polymer are changed by the absorption of the analyte, for instance, the dielectric constant and volume in capacitive sensors [Kummer2004] or the mass in resonant sensors [Lange2001]. The volume change due to absorption can, similarly to the adsorption of humidity, be detected by the resulting stress change of a polymer-coated cantilever.

The cantilever preparation was the same as for the humidity measurements in Section 3.6.3, a drop-coating of photo-resist (Shipley S1818). The chips were mounted in a custom-made, automated gas measurement flow system

[Koll1999]. The flow system provides alternating a reference gas (dry air) and a mix of analyte gas and reference gas through the sensor chamber. The concentration of the gas mixture is programmable and the mixing is stabilized in one flow line while the reference gas is provided through a second line. A rotating valve switches the measuring chamber input between the two lines and provides a sub-second change of concentration, which is suitable for determination of the step response of the sensors.

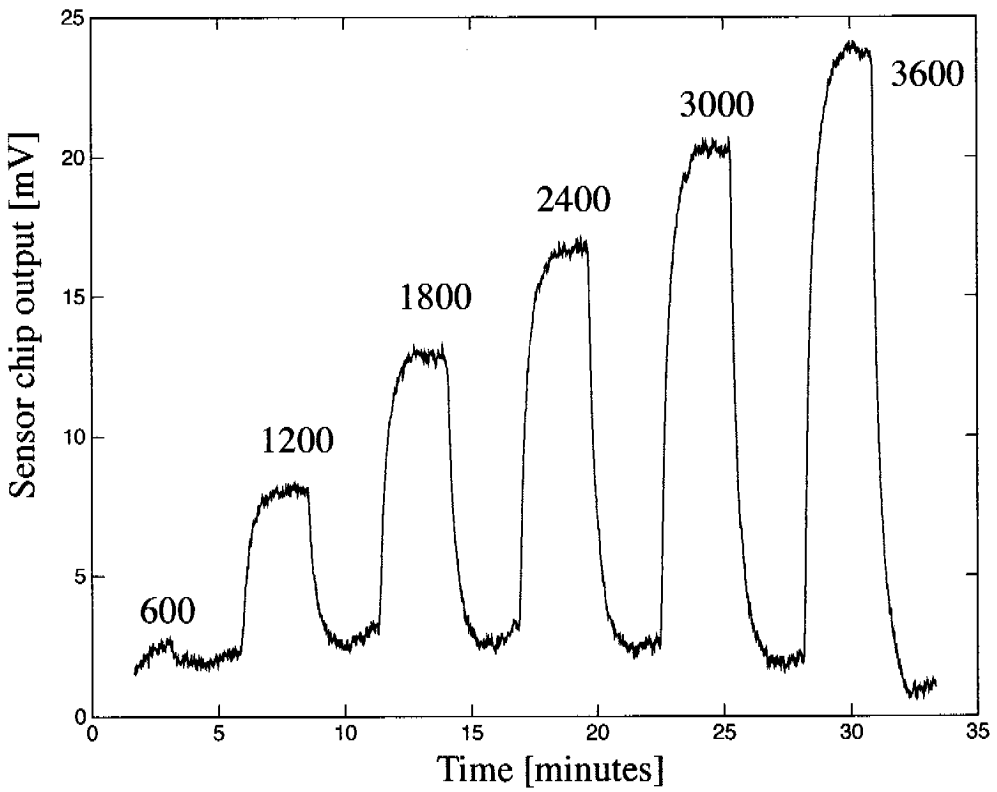

Fig. 3.16: Sensor response of a cantilever coated with photoresist to ethanol gas concentrations from 600 ppm to 3600 ppm. The chip gain is 320 and the bridge bias is 5 V. The lowest setting of 600 ppm is at the limit of operation of the mass flow controller which makes the concentration uncertain.

The sensor response to ethanol gas is shown in Fig. 3.16. The ethanol concentration was ramped from 600 ppm to 3600 ppm in steps of 600 ppm. The chip output sensitivity is 6 μV/ppm, corresponding to a detection limit of 250 ppm (3 times the background noise level). The on-chip amplification was 320 and the

bridge bias was 5 V. The equivalent sensor sensitivity is 5 nV/ppm/V. As seen in Fig. 3.16, the response has a time constant of 25 s, attributed to the absorption rate in the polymer.

3.6.5 Liquid Operation

Stability in Liquid

The first experiments with the chips in liquid environment were performed in a dual-in-line (DIL) package. After wire bonding, the wires and the chip were covered with a UV-curable epoxy (Epotek OG116) leaving only the cantilevers unprotected (see Fig. 3.17b). A PMMA ring was glued on top of the package to form a liquid reservoir (see Fig. 3.17a). The liquids were injected with a pipette.

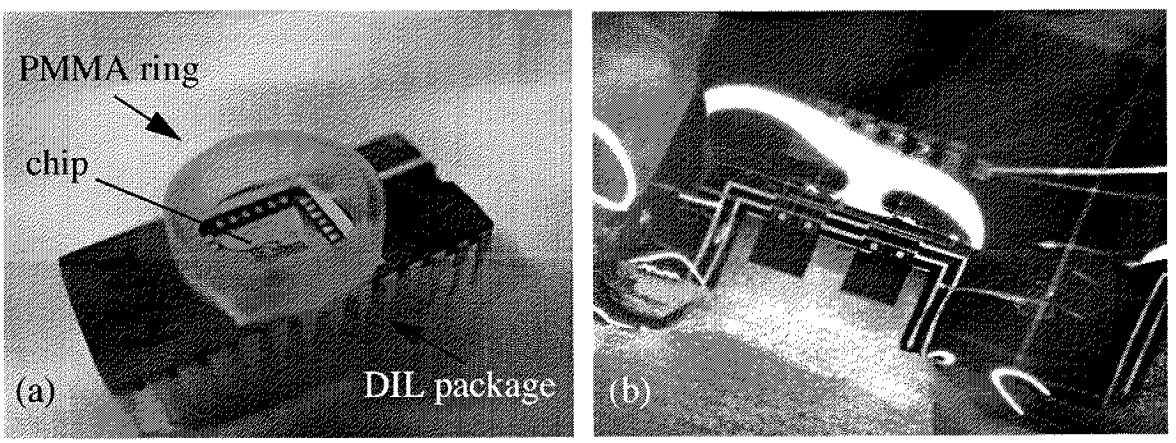

Fig. 3.17: (a) Liquid cell for non-flow experiments. A PMMA ring is glued on top of a standard 28-pin DIL package. (b) Close-up of the sensor chip inside the package. Bond pads and wires are covered by a protecticve epoxy.

Renewal of the liquid in the reservoir consisted of cycles of extracting and injecting liquids with a pipette.

After injection of DI-water, a change in the sensor signal of 200–500 μV (non-amplified) that would take 1–2 hours to stabilize was observed (see Fig. 3.18). The open packaging caused the sensor to be sensitive to changes in the liquid meniscus and was consequently not appropriate for high-sensitive measurements. However, it allowed for evaluation of the long-term physical stability

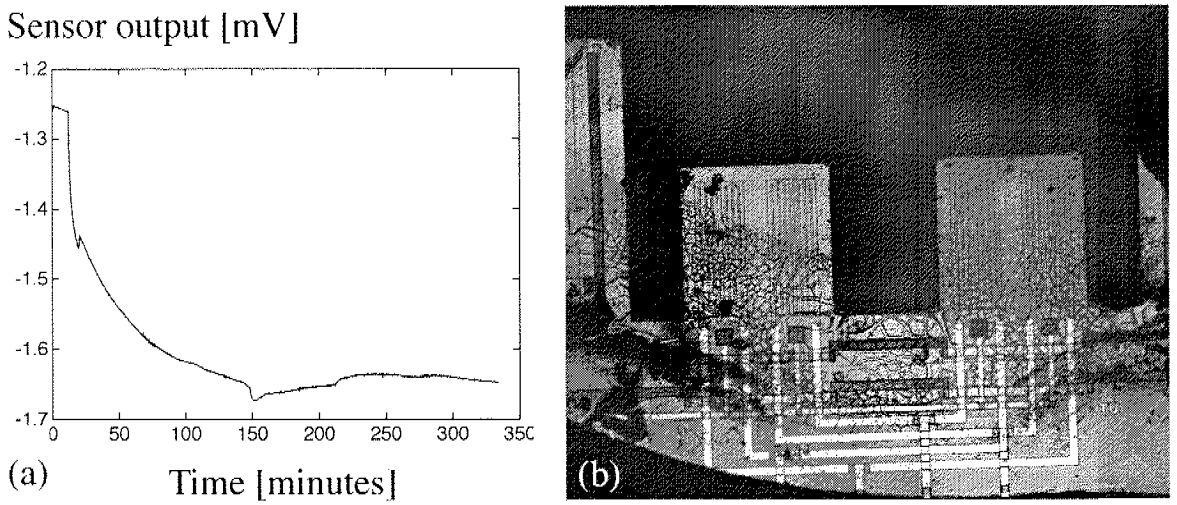

Fig. 3.18: (a) Sensor output (non-amplified) after immersion in DI-water. The Wheatstone bridge is biased at 2.25 V. (b) Photograph of a chip after 20 hours in PBS solution. A visible layer has built up on top of the sensors. The chip was rinsed in DI-water and dried before the photograph was taken.

of the chips in different solutions. The (powered) chips had a life-time of more than two to three days in DI-water. They would typically fail after 1 day in PBS solution. In some cases a build-up of salt crystals was observed, suggesting that electrolysis of the salt solution was taking place. Water was sometimes detected between the chip and the protective epoxy, reaching the bond pads, indicating that the epoxy did not stick well enough to the chip surface.

Care was taken to cover any exposed metal on the chip with epoxy. For instance, the metal lines carrying biasing potentials for substrate and n-well during KOH etching are exposed at the edges of the chip after dicing, and were subject to electrochemical dissolution if they were not protected.

External Flow Set-up

Once the chips were packaged in the PDMS package (Section 3.4.1) they could be tested in a flow set-up. The first experiments involved the use of a syringe to pump the liquid through the liquid chamber. It was seen that over-pressure in the chamber would delaminate the PDMS plates and cause the liquid to leak between the two plates. This was avoided by sucking the liquid through the chamber, thus creating an under-pressure in the chamber.

To achieve a controlled, slow flow in the chamber, a hydrostatic pressure driven (gravitational flow) set-up was used (see Fig. 3.19). The teflon tubes have a inner

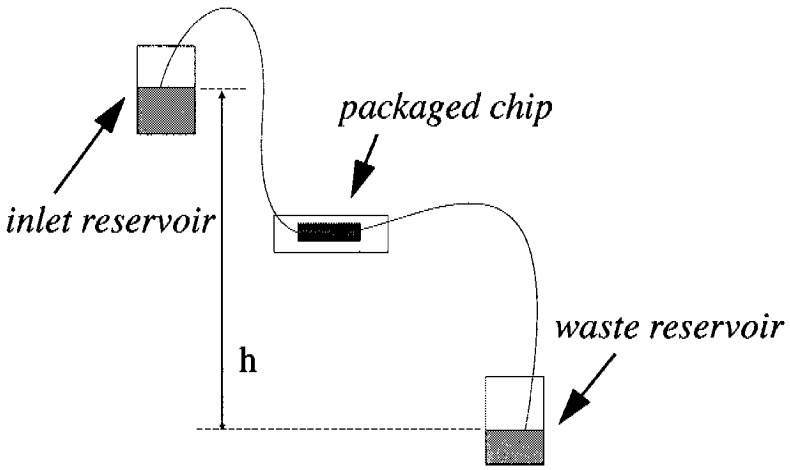

Fig. 3.19: Schematic of hydrostatic-pressure-driven flow set-up. The flow rate is function of the height difference h.

diameter of 500 μm and the total tube length was 90 cm. The flow speed is adjusted by changing the height difference between the inlet and waste reservoirs. Moreover, by placing the chamber near the height of the inlet reservoir, a minimal over-pressure could be achieved. To calibrate the flow speed, a precision scale was placed under the outlet tube, allowing the drops to be counted and weighed. A height difference of 30 cm was found to give a flow of 1 μL/s. However, residual air bubbles in the flow system caused perturbations of the flow speed, which could not be avoided.

A peristaltic pump (MS-Reglo 7331, Ismatec, Switzerland) was used to obtain higher and more reproducible flow rates. The pump was placed at the outlet, sucking the liquid through the chamber, in order to avoid over-pressure that would destroy the package. The pumping speed can be controlled over 30 steps, each step equivalent to 0.05 μL/s. Although the average flow rate is easily controlled and the set-up is less vulnerable to bubbles, the rotating rollers of the pump modulate the pressure and short-term flow rate. This can be seen in Fig. 3.20a, where the roller motion is clearly seen in the sensor output. Since the read-out sampling rate of 1 Hz was close to the frequency of the roller oscillations, an aliasing pattern is seen in the graph.

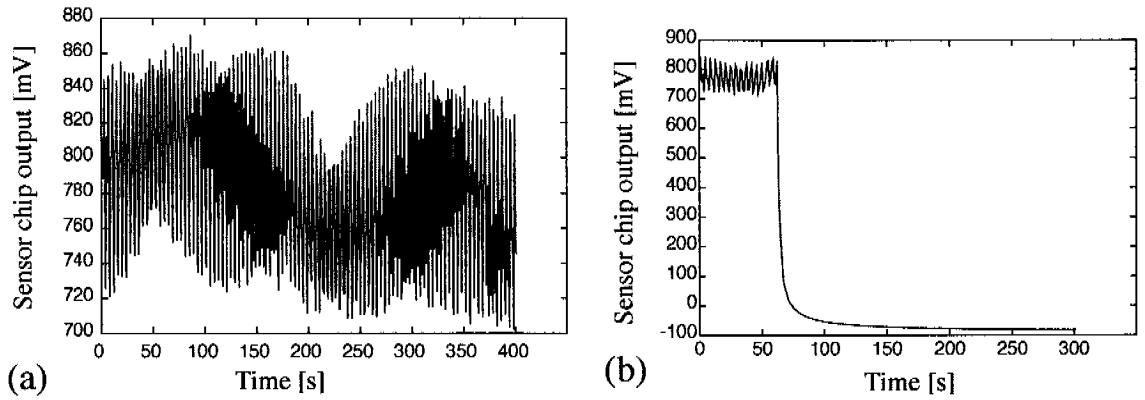

Fig. 3.20: (a) Sensor output at peristaltic-driven flow. The pressure modulations caused by the pump fingers are around the same frequency as the sampling rate (1 Hz), which results in a aliasing pattern in the graph. (b) After the pump is stopped, there is a relaxation time before the sensor signal is stable.

A flow sensitivity of the sensor of 1.2 mV/V per μL/s was measured. Since the read-out would be considerably influenced by the flow sensitivity, it was concluded that the flow needs to be stopped completely during high-sensitivity measurements. However, at the moment the pump is stopped there is a relaxation time before the signal is stable again (see Fig. 3.20b). The compliance of the system slows down the relaxation of the pressure. This effect can be reduced by stiffer tubes, however, the peristaltic pump relies on a soft tube being pressed by the rotating rollers.

The flow sensitivity of the sensor system is believed to arise from the asymmetric input and output channels in the microfluidic chamber. Since the inlet channel is vertically shifted from the outlet channel, there is a vertical flow component in the chamber along the y-axis of the cantilevers. The flow therefore presses on the cantilevers and creates a stress in the piezoresistors. In the case of a dual-cantilever configuration, the different locations of the cantilevers experience different pressure and the flow signal can not be cancelled out. An improved microchamber should therefore avoid this vertical gradient.

The most problematic issue, also for stopped-flow measurements, is the presence of bubbles inside the chamber. A bubble near or touching a cantilever creates a strong signal disturbance. Hermetical sealing of the packaging reduced the

amount of bubbles, though they could not be avoided completely. Degassing of the liquids was seen to greatly reduce the occurrence of bubbles. A desiccator was used to degas all analyte and cleaning solutions for 30 minutes prior to the experiments. The effect of the degassing is, however, limited in time (typically only 1/2 to 1 hour).

BIOCHEMICAL DETECTION EXPERIMENTS

The combination of stopped-flow operation and degassing of the sample and cleaning fluids provided a satisfactory experimental set-up. The next step is the detection of biochemical and biological binding on the cantilevers. However, the preliminary results do not show sufficient reproducibility. The biochemical preparation and surface functionalization is therefore under further development with the goal of ensuring reproducible biological detection experiments.

4 CMOS AFM ARRAY SYSTEMS

After an introduction to atomic force microscopy (AFM) and related microscopy techniques, the design of AFM cantilevers with integrated sensors and actuators will be explained. Two examples of highly integrated AFM systems using cantilevers arrays will be presented, including characterization and imaging results.

4.1 SCANNING PROBE MICROSCOPY

4.1.1 SCANNING PROBE MICROSCOPY TECHNIQUES

The AFM systems presented in this chapter are members of the scanning probe microscopy (SPM) family. Whereas optical microscopes use lenses to scale up a reflected or transmitted image and electron microscopes use electromagnetic lenses to scan an electron beam over the sample, SPM features a measurement probe scanned closely over the sample surface. Different types of SPM techniques can be distinguished by the type of interaction between probe and sample used for the measurement. The lateral resolution is determined by the confinement of the interaction and by the precision of the scanning movement. Usually, a piezoelectric actuator is used to obtain precise, sub-nanometer movements. The sensitivity and resolution of the modulated signal determines the non-lateral image quality factors, such as the height resolution in topology imaging.

Scanning tunnelling microscopy (STM) is one of the most famous examples of SPM, which for the first time demonstrated image resolution down to single atoms [Binnig1982]. A tunnelling current $I \sim V \cdot e^{-az}$ between the tip and the surface is exponentially dependent on their distance z, and small height differences down to 10^{-5} nm can be resolved [Sarid1994]. As in many other SPM systems, a feedback loop is used to maintain the distance between tip and sample constant by controlling the z-axis position of the tip. Thus, the tip continuously tracks the surface topography and the height information is read out from the z-axis actuation signal.

STM is, however, limited to conducting surfaces. The invention of AFM [Binnig1986] broke this barrier and permitted the imaging of soft, non-conducting surfaces like, for example, biological samples. AFM is based on the interaction between the tip and the surface due to atomic or molecular forces, and the measured force acting on the tip reflects the topography of the surface. Other scanning force microscopy techniques use the detection of for instance magnetic or electrical forces to image the magnetostatic or electrostatic properties of the sample surface.

Scanning near-field optical microscopy (SNOM) is a more recent member of the SPM family. A near-field light source, created by shining a light beam through an aperture smaller than the wavelength of the light, is scanned over the surface and the reflected or transmitted light intensity is recorded. The half-wavelength diffraction limit of conventional optical microscopes is side-stepped and lateral resolutions of 50–100 nm can routinely be achieved [Hecht2000]. The light source is controlled to stay at a constant distance from the sample, and the topography is recorded at the same time as the optical properties.

4.1.2 AFM Detection Schemes

The first AFM systems used the deflection of small metallic wires to detect the interaction forces, but soon microfabricated cantilevers of silicon, silicon dioxide and silicon nitride with precisely defined properties and efficient batch manufacturing were used instead.

In the beginning, the deflection was measured by the tunnelling current between the cantilever and a reference tip, as if a stationary STM measurement is performed on the cantilever itself. However, optical read-out schemes have been dominating ever since they were introduced in 1988 [Meyer1988]. These schemes include laser-diode feedback, homodyne and heterodyne interference and polarization detection systems, as well as the most dominating, the multiple photodiode deflection method. More recently, non-optical methods based on piezoresistive force sensors, as presented in this thesis, have gained increased interest as they solve some shortcomings of optical systems.

4.1.3 Operation Modes

The topography read-out is usually done in constant-force mode, where a feedback controller regulates the height of the sample in order to maintain a constant tip-sample force. In constant-height mode the tip is scanned in the lateral direc-

tions only and the varying forces, i.e. tip deflections, must be translated into topographical information.

AFM can be performed in contact or non-contact mode. In contact mode a relatively high force is used to keep a small tip-sample distance (repulsive regime). The non-contact mode relies on the longer-range, attractive interaction forces and is more suitable for soft samples.

The non-contact mode is in most cases associated with dynamic (or resonant) operation, where the cantilever is driven to vibrate near its fundamental resonance frequency. The tip-sample interaction slightly shifts the resonance frequency and alters the vibration amplitude and phase at the driving frequency. For constant-force imaging, the height is in this case continuously adjusted to maintain a constant vibration amplitude or phase.

Although all combinations of these different techniques are theoretically possible, most AFM imaging is done using either the constant-force, contact, static mode or the constant-force, non-contact, dynamic mode.

4.1.4 Cantilever Arrays

The serial nature of SPM inherently limits the image acquisition speed. Also, high resolution scanning stages provide only comparatively small scanning ranges, typically below 100 μm. The use of arrays of scanning cantilevers is a way to speed up the image acquisition rate and to extend the total scan area [Minne1998, Minne1999]. Multiple cantilevers also provide redundancy and allow for continued operation without having to replace cantilevers after individual failure, which is of particular importance in embedded or autonomous systems [Staufer2000]. For chemical force microscopy and surface analysis, it can also be advantageous to have an array of individually functionalized cantilevers, permitting the realization of several different interaction assays simultaneously in one experiment.

Although parallel or multiplexed optical systems have been investigated for chemical sensing [McKendry2002], integrated sensing elements greatly simplify multi-cantilever designs and have shown to be more efficient for SPM imaging [Minne1998].

Finally, the prerequisite for simultaneous multi-cantilever, high-resolution topography imaging is height control for each cantilever. In most topography SPM systems a piezotube or a similar actuator is used to move the sample relative to the

single scanning cantilever. With several cantilevers tracking the surface, however, the height actuation has to be performed individually for each cantilever. This can be achieved by a highly integrated system with height actuation capability implemented in each cantilever itself.

4.2 CANTILEVER DESIGN

The AFM cantilever developed during this thesis is designed for integration in a cantilever array and is based on previous work of Dirk Lange [Lange2002]. Two vital functions for force microscopy are included in the cantilever itself: height actuation by a thermal, bimorph actuator and force detection by piezoresistive stress sensors. Both these elements are fabricated in the CMOS process and the silicon cantilever is shaped in a post-CMOS process sequence as explained in Section 2.7.

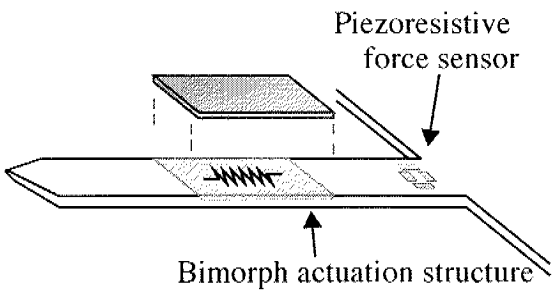

Fig. 4.1: Schematic of the cantilever design. The length and width are 500 µm and 85 µm, respectively. The bimorph actuator segment is 250 µm long. The piezoresistive force sensor is located near the clamped end.

A schematic of the cantilever design is shown in Fig. 4.1. The dimensions have been chosen to obtain a cantilever stiffness k in the order of 1 N/m, which is appropriate for both static and dynamic cantilever operation. The length of the cantilevers is 500 µm, which provides sufficient distance between the chip bulk and the sample surface, yet without making the cantilevers too long and fragile to manufacture and use. The array pitch is set to 110 µm, so that adjacent, slightly overlapping images from multiple cantilevers can be recorded with a x-y scanner of 120 µm range. The width of each cantilever is 85 µm, yielding a spacing of 25 µm.

4.2.1 FORCE SENSOR

The CMOS process provides a p^+ diffusion of 400 nm depth (source/drain implementation) which is used for the piezoresistive force sensors. Four identical resistors form a Wheatstone bridge placed near the clamped end of the beam, where the stress response from a tip force is maximum (see Eqn. (2.15)).

As seen in Section 2.4.2, the relative resistance changes of resistors aligned along and across the cantilever axis are of opposite sign. The bridge resistors can therefore be oriented pair-wise in the two directions, with all four resistor changes contributing unidirectionally to the bridge output (see Fig. 4.2).

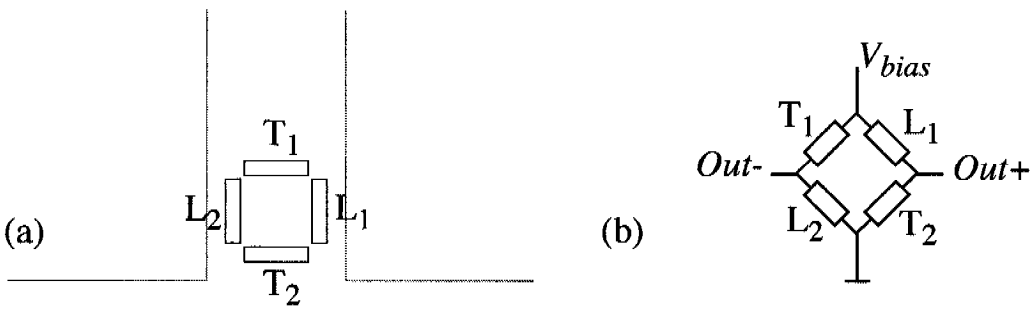

Fig. 4.2: (a) Piezoresistive bridge located near the clamped edge of the cantilever. (b) The four resistors form a full Wheatstone bridge, with two resistors along the cantilever axis and two resistors across.

4.2.2 HEIGHT ACTUATION

A resistive heater in combination with a bimorph layer stack allows precise deflection of the cantilever by application of an electrical signal. The heater is a diffused p^+ resistor from the CMOS process. The bimorph is formed by the silicon of the cantilever and a thick aluminium layer, the latter being composed of the two CMOS metal layers merged through a "via"[1] opening.

The higher temperature expansion coefficient of the aluminium ($2.3 \cdot 10^{-5}$ K^{-1}) relative to that of silicon ($2.6 \cdot 10^{-6}$ K^{-1}) [Roberts1981] will make the heated bimorph bend downwards as the aluminium expands more than the silicon. The bending (and radius of curvature) is uniform over the area of the heater element as long as

1. An opening of the insulating oxide between two metal layers.

the temperature is uniform. The resulting deflection is, within the range of linear operation, proportional to the temperature elevation [Chu1993].

A large part of the cantilever is reserved for the actuator element in order to achieve a substantial actuation range of several micrometer tip deflection. The force sensor on the other hand is relatively small and confined to a short segment of the cantilever (see Fig. 4.1).

4.2.3 Integration of Sensing and Actuation Elements

The actuator should move the cantilever tip down to and up from the sample surface by deflecting the cantilever, ideally without affecting the force sensor signal. Their co-integration on the cantilever, however, leads to unwanted sensor-actuation coupling (SAC), caused by a combination of mechanical, thermal and electrical effects.

The heated bimorph element creates a bending moment along its length. Some strain will also propagate into the adjacent, single-layer cantilever segments, but as long as the sensors are placed sufficiently far away from the bimorph, the sensor signal is expected to be unaffected. However, when the actuation excites one of the resonant modes of the cantilever, the whole cantilever will be oscillating, with bending moments also in the sensor regions. A strong, mechanical SAC is therefore expected at the resonance frequencies of the cantilever.

Thermal cross-talk can be expected since thermal actuation necessarily creates heating and temperature gradients, and the piezoresistors used are influenced by temperature changes (see Section 2.2.4). A static analysis of the temperature distribution shows that the temperature decreases almost linearly from the heater towards the bulk of the chip, which acts as a heat sink [Juillerat1999]. The force sensor is therefore placed away from the actuator and as close as possible to the bulk chip, where the temperature rise is smaller. Although the symmetry of the bridge cancels out the influence from a uniform temperature field, temperature differences between the resistors will affect the bridge output. The resistors are therefore placed as close as possible to each other, so that the temperature gradient causes minimal temperature differences.

The proximity of the leads carrying the driving signal for the thermal heater and the leads connecting the Wheatstone bridge can cause capacitive SAC, although this is only a problem for relatively high frequencies. Another electrical coupling can arise through a shared power supply, if the high current through the heater

affects the supply voltage for the sensor and amplification circuitry. Separate and well-regulated power supplies are therefore desirable.

4.2.4 Frequency Response

Knowledge of the actuation performance at different frequencies is important for the cantilever operation at high scanning speeds. The feedback and driving control of the AFM imaging system has to be designed and operated in accordance with the dynamic parameters of the cantilever system in order to optimize the scanning performance.

When designing the associated control system, it is especially interesting to have a mathematical model of the cantilever which can be integrated with the simulation tools that are used for the circuitry design, as this permits a complete simulation of the combined system. The model can be expressed as a transfer function, with the actuation signal as input and the mechanical response of the actuation as output. In our case, where the useful actuation is the deflected height of the cantilever tip, and the actuation signal is the electrical power provided to the heater, the transfer function is expressed as deflected tip height z per heating power P:

$$T_{actuation}(\omega) = \frac{z(\omega)}{P(\omega))} \tag{4.1}$$

A detailed physical model for the behaviour of an electrothermally actuated cantilever, deriving the temperature distribution and using modal analysis to calculate a qualitative frequency response, has been developed in [Lange2002, Lammerink1990, Lammerink1991]. In the following, a simpler, descriptive model will be developed with the goal of providing a transfer function precise enough for including the cantilever in a design simulation of a complete control system [Volden2004]. The validity of this model will be justified by measurements of fabricated cantilevers presented in the next sub-chapters.

The power dissipated in the heating resistor warms up the bimorph and, eventually, the rest of the cantilever. The cooling is taking place mainly by conduction through the cantilever and the heat dissipated by convection through the air can be neglected. Heat flows out from the cantilever through the base to the bulk of the chip, which acts as a heat sink. As the frequency of the actuation signal increases, the temperature oscillations are confined to a smaller area, due to the

finite speed of the heat propagation [Lange2002]. The thermal actuation will therefore show a low-pass characteristic.

We will associate the electrothermal heating with the transfer function of a first order low-pass filter $L(\omega)$ of cut-off frequency ω_c:

$$T_{heater} = L(\omega) = \frac{\omega_c}{\omega_c + i\omega} \tag{4.2}$$

The mechanical response of the cantilever can be approximated by a damped harmonic oscillator $H(\omega)$, with resonance frequency ω_0 and damping factor δ:

$$T_{cantilever} = H(\omega) = \frac{\omega_0^2}{-\omega^2 + 2i\omega\delta + \omega_0^2} \tag{4.3}$$

Together with a scaling factor K, which represents the efficiency of the actuation at near-dc operation, the total transfer function of the thermal actuation is:

$$T_{actuation} = K\ T_{heater}\ T_{cantilever} \tag{4.4}$$

or explicitly

$$\frac{z}{P} = K \cdot L(\omega)H(\omega) = K\ \frac{\omega_c}{\omega_c + i\omega}\ \frac{\omega_0^2}{-\omega^2 + 2i\omega\delta + \omega_0^2} \tag{4.5}$$

The amplitude of this transfer function with an example set of parameters is shown in Fig. 4.3. The transfer function will be compared to measurements on fabricated cantilevers in Section 4.4 and 4.5.

4.3 Fabrication and Packaging

The processing of wafers for the fabrication of AFM chips follows the general procedure outlined in Section 2.7. After dicing of the wafers, the chips were mounted on small printed circuit boards using epoxy glue and wire-bonded. For characterization of the chips with a commercial AFM piezo-scanner, the boards

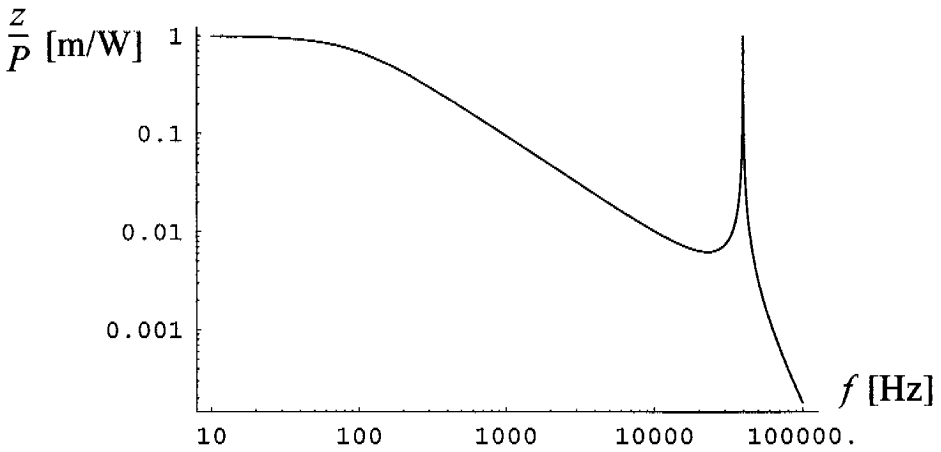

Fig. 4.3: Simulated amplitude of the transfer function z/P as a function of frequency f. The parameters are $K=1$ m/W, $\omega_0=250000\ s^{-1}$, $\omega_c=600\ s^{-1}$, $\delta=300$.

were mounted on a metal holder, similar to the one used for commercial AFM cantilevers.

4.3.1 Connection Interface

In contrast to passive cantilevers for optical read-out, which only need a mechanical fixation usually obtained by clamping, cantilever chips with integrated read-out and electronics need electrical connections. For testing and characterization, the above described packaging method is reliable and satisfactory. However, in the perspective of developing these AFM systems into commercial instruments that are relatively easy to use, a faster and easier way of replacing the chips is desirable. AFM cantilevers have a limited life-time in normal laboratory usage, and even if multi-cantilever arrays provide redundancy in case some cantilevers are damaged, the whole chip eventually has to be replaced.

A connector solution was therefore developed, that avoids the need for wire bonding and also provides a good fixation and alignment of the chip. This solution also integrates into the fabrication process and does not demand additional, cost-driving processing steps. For scanning operation on flat surfaces, any steric extension on top of the chip has to be minimized, in order to allow for a small angle between the cantilever and the surface (see Fig. 4.4).

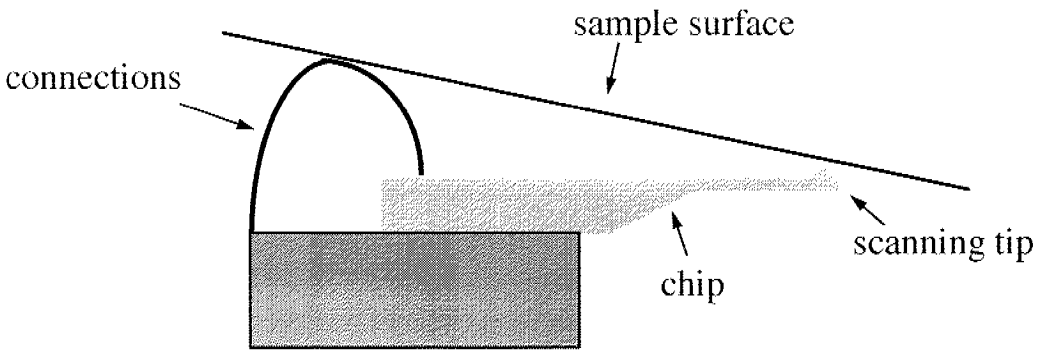

Fig. 4.4: Schematic of a cantilever chip scanning a sample surface. If the connections to the chip extend high above the chip, the scanning angle will have to be adjusted so that the surface is not touched by e.g.connecting wires.

The presented plug-in concept is based on a clamping mechanism, where a thin metal lever holds the chip from the top (see Fig. 4.5). The lever is parallel to the chip surface and extends only to the back part of the chips, where the bond pads are located, so that the scanning angle can be kept small.

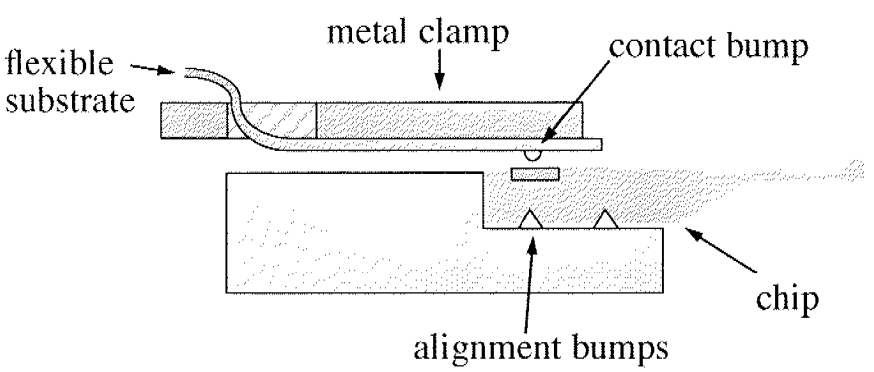

Fig. 4.5: Schematic of the plug-in concept. The chip is aligned by metal bumps in the holder fitting into backside holes in the chip. The metal clamp holds the chip in place while pressing the contact bumps of the flexible substrate against the chip bond pads.

The chip rests on a metal holder which also provides alignment features. Using electrical discharge machining, two small, precise bumps are made on the top

surface of the metal holder (see Fig. 4.6a). The chips have corresponding openings at their bottom surface that the bumps fit into (see Fig. 4.6b). A square opening of 300 μm x 300 μm provides a fix point and a rectangular opening of 300 μm x 500 μm, allowing translation, provides the angular fixation for the round metal bumps. The openings are fabricated with the same backside KOH etch as used for the silicon membrane fabrication (see Section 2.7) so that no additional masks or processing steps are needed for the chips. The resulting holes are grooves with walls that have a 54° angle to the chip surface owing to the anisotropic etching characteristics of silicon.

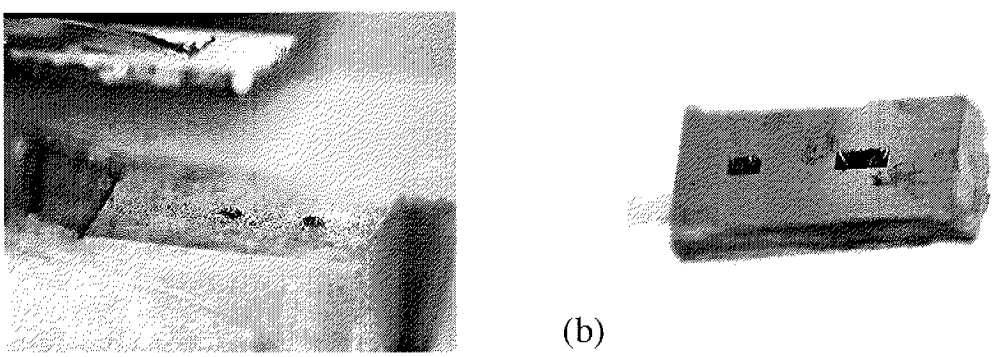

Fig. 4.6: (a) Chip holder with metal bumps for alignment. (b) Chip backside with matching holes, anisotropically etched.

A thin, flexible substrate carries connection leads that terminate in gold covered copper balls right under the metal clamp. The substrate used for evaluation was the commercial "Gold Dot" product (Delphi Connection Systems, Michigan, USA[1]) with a connector pitch of 167 μm. The gold balls connect directly to the bond pads of the CMOS chips. The standard aluminium pads of the CMOS process are used without modification.

Fig. 4.7 shows an AFM chip mounted in the holder. The connector scheme allows for easy replacement of the AFM chips with the help of normal tweezers. The alignment features ensure the correct placement of the chip with a precision better than 25 μm. The contact resistance, measured using a chip that had two bond pads connected to each other, was below 1 Ω per contact.

1. http://delphi.com/connect/

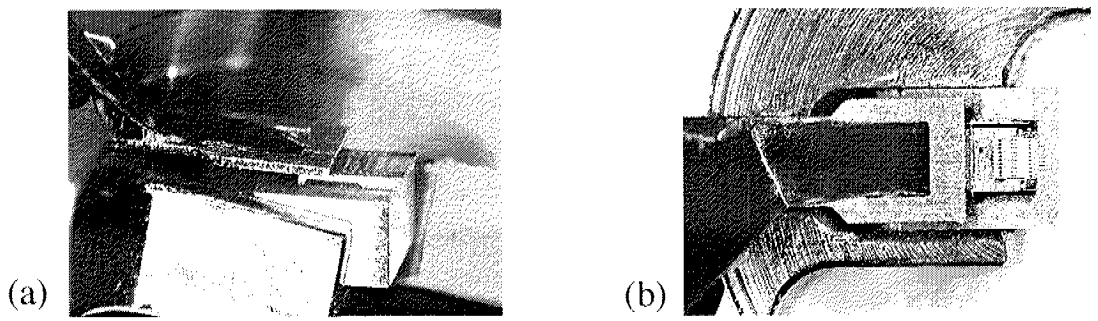

Fig. 4.7: AFM chip inserted into the clamp, seen from the side (a) and from the top (b). The flexible substrate carrying the connection leads is seen on the left side of the photos.

4.3.2 Tips for Enhanced Image Resolution

For AFM and other scanning probe imaging techniques, the lateral resolution is dependent on the sharpness of the scanning tip, since the acquired image is the result of a convolution between the tip and the sample [Castle1997]. For low-resolution scanning, the lithographically defined triangular shape of the cantilever end can act as the scanning tip. However, the sharpness of this tip is limited by the lithographic definition and the subsequent silicon RIE that cuts the cantilever out of the membrane. In order to achieve a higher resolution a sharper tip has to be used, either by mounting a separately fabricated tip onto the cantilever or by fabrication of tips directly on the cantilever.

From a production point of view it is desirable to develop an efficient wafer-scale solution to avoid individual processing of each chip or cantilever.

Integrated Tips

The direct fabrication of tips on CMOS chips poses some challenges. In order not to damage the electronic components, temperatures during post-processing should not exceed 400 °C. This rules out the use of oxide sharpening [Marcus1990], which is a very common finishing technique for AFM tips. The electronics must also be protected from etchants used during processing. Methods to integrate a sharp tip in the cantilever silicon surface in a post-CMOS technique have been investigated [Ono2002]. A tetramethylammonium hydroxide (TMAH) solution was used to etch away the silicon around the tip. PECVD (plasma-enhanced chemical vapour deposition) silicon oxide was used as mask

material. An island of oxide defines the location of the tip, which is left as a silicon pyramid with walls formed by the anisotropic etching (see Fig. 4.8a).

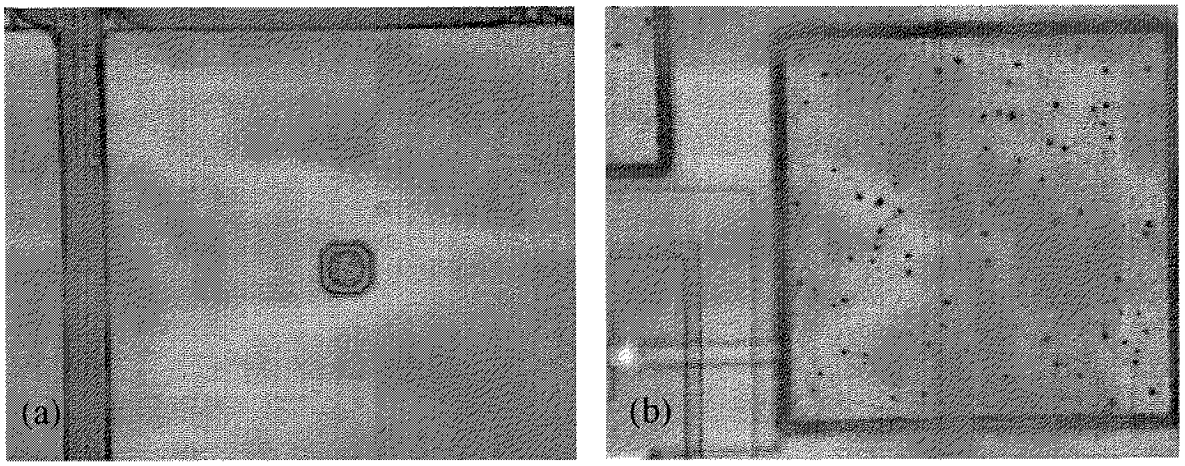

Fig. 4.8: (a) TMAH etching of integrated silicon tips. The square with rounded corners is the oxide mask defining the tip location. The inner octagonal is the tip being shaped by anisotropic etching. (b) Aluminium pads attacked by the etchant.

This procedure was applied to a processed wafer with AFM arrays (before the cantilever release from the front side). However, the aluminium layers were clearly attacked during the TMAH etch, most probably through pin-holes in the oxide layer that should have protected the aluminium pads (see Fig. 4.8b). Also, the reproducibility of the tip shape was not sufficient, and variations in etch rate over the wafer caused unfinished tips in some areas and over-etched, rounded tips in others.

Composite Tip Mounting

Examples of separate tip fabrication with subsequent transfer of tips onto the CMOS cantilevers have been demonstrated [Akiyama1999]. For the imaging results presented in Section 4.5, sharpened silicon nitride tips prefabricated on silicon nitride cantilevers[1] were transferred onto the AFM cantilevers. The nitride cantilevers were first perforated with a laser, to be more easily broken off at a well-defined location close to the tips. The free end of the nitride cantilever carrying the tip was then glued on top of the AFM cantilever using a small dose of

1. Provided by Prof. Urs Staufer, University of Neuchâtel, Switzerland

epoxy glue (see Fig. 4.9a). The alignment was done with translation stages under a stereo microscope. After hardening of the epoxy, the nitride cantilever was torn off, leaving the nitride tip on top of the AFM silicon cantilever.

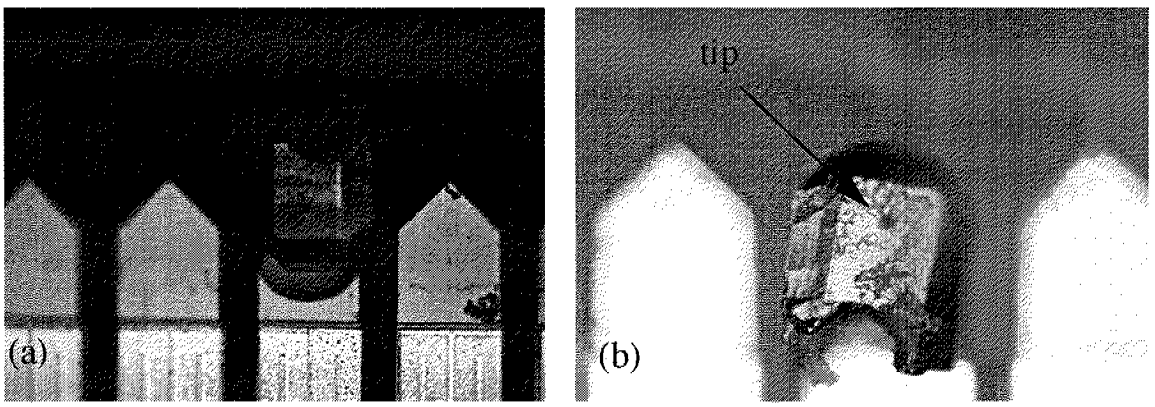

Fig. 4.9: Mounted silicon nitride tips. (a) the nitride cantilever carrying the tip was glued onto the AFM cantilever and broken off at the laser-cut perforation. (b) a broken-off cantilever tip was manually placed on top of the AFM cantilever.

This tip transfer technique however leaves the remains of the nitride cantilever extending out from the silicon cantilever, with the result that the tip is not at the very end of the cantilever. Consequently there is a great risk of touching the sample surface with the cantilever end instead of with the tip. Another method was therefore also investigated, where a broken-off nitride tip was picked up and placed on the end of the silicon cantilever with the nitride remains pointing towards the cantilever base. The results were better (see Fig. 4.9b), but the method was more laborious and time-consuming.

4.4 Ten-Cantilever Multiplexed Array

This microsystem integrates an array of ten cantilevers together with analog electronics on a single CMOS chip. The design has been developed and presented in [Lange2002] including some characteristics of fabricated chips. This chapter will present a more complete characterization of these devices, which laid the base for a more integrated design presented in the next subchapter.

4.4.1 CANTILEVER DESIGN

The CMOS process used is a high-voltage process offering extra layers for the fabrication of high-voltage components in addition to the layers of a normal low-voltage process (see Tab. 4.1). The extra layers also offer additional possibilities for sensor design. Most importantly, a deep n-well and a shallow p-well are provided. N-type resistors can in turn be placed in the p-well for use as piezoresistive elements. The shallow, low-doped p-well can also be used for piezoresistors.

*Tab. 4.1: Process parameters for a 2.0-µm, high-voltage, double-metal CMOS process (courtesy of austria*microsystems*, Graz, Austria). (TCR = temperature coefficient of resistivity)*

Device layer	Thickness (µm)	Sheet resistance (Ω)	Min. width (µm)	TCR (10^{-3} K^{-1})
n-well	4.0	1900	5.0	7.3
deep n-well	6.75	900	5.0	6.2
shallow p-well	1.55	2000	5.0	4.6
n^+ diffusion	0.5	27	2.4	1.4
p^+ diffusion	0.55	57	2.4	1.5
metal-1	0.55	0.09	3	3.2
metal-2	0.9	0.06	3	3.1

The reticle design includes a series of arrays with some variations of the cantilever structure. There are three different Wheatstone bridges, each applied in two different cantilever configurations. In the first configuration, the deflection sensor is located at the base of the cantilever and the thermal actuator in the middle segment of the cantilever. In the second, "inverted" configuration, the thermal actuator is located in a broader base segment and the deflection sensor at the beginning of the second, narrower end segment.

The different Wheatstone bridge designs use different layers for the resistors and for the connecting leads [Franks2002]. The first design (A) uses p-well resistors and p-diffusion connection leads. The second design (B) has the diffusion leads replaced by metal lines. The third design (C) uses p-diffusion resistors and metal connections. The presented characterization focuses on the non-inverted cantilever configuration and C-type resistors.

4.4.2 System Design

The system includes multiplexers for selection of the active cantilever. The signal from the selected Wheatstone bridge is fed through the dual input-multiplexer and into a differential output amplifier of gain 23. An externally provided current can be added to the bridge signal before the amplifier to compensate for the offset from the sensor. The actuation input signal goes through the input multiplexer to the driving module present for each cantilever. The module includes a sample-and-hold filter, so that the specified actuation signal for each cantilever can be kept constant while the other cantilevers are selected and adjusted. The buffer amplifier driving the heating resistor effectively implements a voltage gain of 2, where the heating resistor, having a third, mid-way terminal, functions as voltage divider for the negative feedback to the amplifier.

4.4.3 Characterization

Actuation Response

The frequency response of the cantilever actuation, i.e. the cantilever vibration amplitude in response to a signal applied to the bimorph actuator, was measured using an optical vibrometer (OFV 300/2000, Polytec, Germany) in combination with a gain-phase analyser (HP-4194A, Hewlett Packard, USA). The gain-phase analyser drives the cantilever actuator, scanning the frequency over the desired measurement frequency range. The laser beam from the vibrometer is focused on the cantilever end and reflected back into the vibrometer sensor, measuring the axial velocity of the reflection spot. The velocity is returned by the vibrometer controller as a proportional voltage and is recorded by the gain-phase analyser. If the cantilever is driven harmonically, the amplitude of the oscillation can be calculated by dividing the measured velocity by $2\pi f$, where f denotes the actuation frequency.

In order to obtain the actuation efficiency, i.e. the deflection of the cantilever tip per applied heating power, the exact heating power is calculated from the driving voltage. When driven by a sinusoidal voltage $V(t) = V_{ac}\sin\omega t$, the instantaneous, dissipated power in the resistor $P = V^2/R$ will include frequency components at 2ω only. However, the gain-phase analyser measures only the signal component at the driving frequency ω. Therefore, a dc component has to be added to the sinusoidal signal in order to obtain vibrational components at the driving frequency ω.

In the experimental set-up, a dc component V_{dc}, equal to the amplitude V_{ac}, was added to the sinusoidal driving voltage from the gain-phase analyser. When applying a total power $P = (V_{ac}\sin\omega t + V_{dc})^2/R$, the vibration amplitude recorded at frequency ω is related to the heating power component $P_\omega = 2V_{ac}V_{dc}/R \cdot \sin\omega t$.

In the approximation of a homogeneous silicon cantilever with rectangular cross section, the fundamental resonance frequency of the cantilever can be estimated with the help of Eqn. (2.13). Using an effective length of 450 μm due to the narrow tip and a thickness of 4 μm, the expected resonance frequency is around 25 kHz. The cantilevers effectively show a fundamental resonance frequency between 20 kHz and 25 kHz.

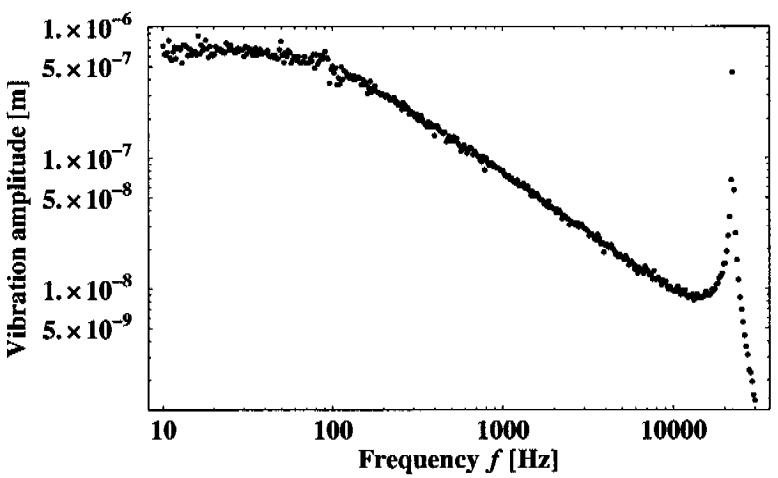

Fig. 4.10: Measured frequency response of the thermally driven cantilever. The driving power component at the measuring frequency P_ω was 1 mW.

Consequently, the range for the frequency scans was chosen to be 10 Hz to 30 kHz, with close-up scans around the resonance peaks. A typical amplitude transfer characteristic of the thermally excited cantilever is shown in Fig. 4.10. Beyond a corner frequency of around 100 Hz the vibration amplitude decreases with 1/f. This distinct low-pass characteristic is typical for the thermal actuation. Around 24 kHz the fundamental resonance frequency of the cantilever is clearly seen. The amplitude at the resonance frequency is comparable to the amplitude at near-dc frequencies.

The data were fit to the model described in Section 4.2.4 and the superposition of the fit model curve and the data can be seen in Fig. 4.11. The fit model is able to

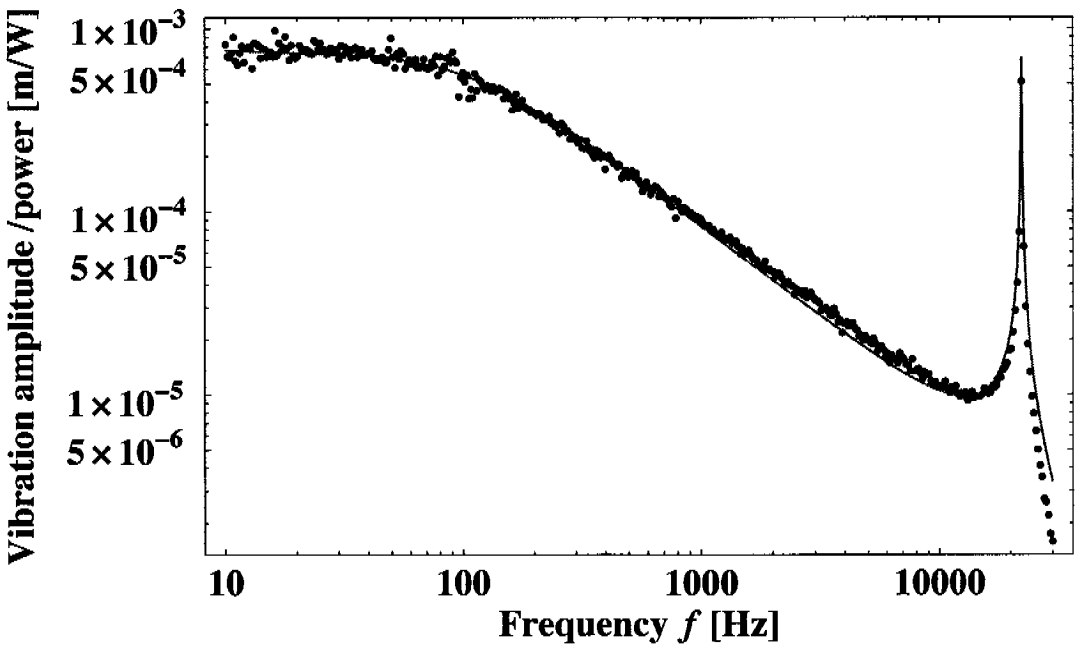

Fig. 4.11: Actuation efficiency of the thermally driven cantilever as a function of frequency. Superposition of the fit model curve (grey line) and the measured raw data (black dots).

closely represent the measured data points, and the model parameters can be extracted. The actuation efficiency at low frequency, corresponding to K in Eqn. (4.5), is 800 μm/W. The resonance frequency ω_0 is 140000 s^{-1} (or 22 kHz).

Actuation Efficiency

The amplitude values calculated from the optical vibrometer output signal depend on the position of the laser beam on the cantilever, and even if care is taken to focus the beam on the tip of the cantilever, some uncertainty in the optically read-out values will be introduced. To verify these values, a second method to determine the actuation efficiency was developed, using the a piezo-tube from a commercial AFM system (Multimode MMAFM-2, Veeco Instruments Inc, USA). With the Nanoscope running in force-distance ramping mode, the cantilever tip was set to touch down on the surface. A known heating power was then applied to move the tip away from the surface. The piezo-tube was adjusted to get back to the same touch-down point. The cantilever deflection is then equal to the applied piezo-tube height offset. The resulting dc actuation efficiency was compared to the efficiency determined by the vibrometer for low frequencies. The low frequency actuation efficiency $z/P = 800$ μm/W corresponds well to the efficiency $z/P = 700$ μm/W obtained using the piezo-tube. The additional heat transfer from the tip to the surface can explain the slightly lower efficiency in the latter case. The measured actuation efficiency enables cantilever deflections up to 7 μm with a 5 V driving voltage (10 mW).

Array Uniformity

Around 50 cantilevers were tested and statistics on the parameter spread could be established. Tab. 4.2 summarizes the model fit parameters from three arrays of ten cantilevers. The spread in resonance frequency is also visualized in Fig. 4.12,

Tab. 4.2: Fit model parameters extracted from 3 identical arrays of each 10 cantilevers.

Parameter	Mean	Std.deviation	Unit
ω_0	140 000	7800	s^{-1}
δ	390	36	s^{-1}
ω_c	690	39	s^{-1}
K	$7.6 \cdot 10^{-4}$	$8.8 \cdot 10^{-5}$	m/W

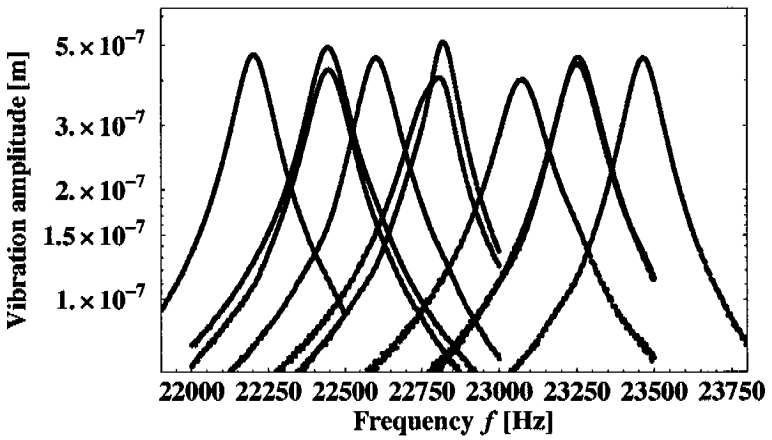

Fig. 4.12: Vibration amplitude as a function of frequency around the fundamental resonance frequency of ten cantilevers in a single array.

which shows the superposition of the resonance peaks from all ten cantilevers of one array.

The process variations in the processing of the cantilever arrays contribute to variations in geometry and physical characteristics of the cantilevers. The length and width of the cantilevers are defined by photolithography and are precise to within 2-3 micrometer, thus having a high relative precision. A misalignment of the photolithography mask with the wafer will change the dimensions of the cantilevers in an almost uniform way across one array and would only be seen as a variation between different arrays in the case of a rotational misalignment. The thickness can however be subject to higher relative variations. Although the depth of the n-well diffusion used as the etch stop in the electrochemical etch stop (ECE) process is well defined in an industrial CMOS process, the quality of the ECE process will determine the resulting membrane uniformity. When additional membrane thinning is performed with RIE, the uniformity of this etching step is equally important. In our case, the RIE etch used for membrane thinning seems to be non-uniform, resulting in a thickness variation. It is therefore assumed that the spread in resonance frequency reflects the thickness variations in the fabricated silicon membrane from which the cantilevers are released. As the resonance frequency is proportional to the thickness (Eqn. (2.13)), the relative spread in resonance frequency (±3% in the array from Fig. 4.12) would imply the same relative spread in cantilever thickness. The variations between arrays are larger,

around 6%, and can be attributed to the spread in thickness of the different membranes on the processed wafer, where each array is released from a separate membrane.

SENSOR-ACTUATOR CROSSTALK

The heater is confined to the middle section of the cantilever and creates a bending moment over the length of the bimorph. Bending or stress caused by the thermal actuation should be minimal outside this area in order not to interfere with the sensing principle. The stress sensors are placed at the clamped edge of the cantilever, at 50 μm distance from the heater, and should ideally only detect a force acting on the cantilever tip. Such a tip force will create stress along the whole cantilever, with a maximum at the clamped edge. With the present cantilever design, however, a sensing signal was measured with the piezoresistors as soon as the cantilever was thermally excited, without any force acting on the tip. As seen in Section 4.2.3, this sensor-actuator coupling can be explained in terms of the thermal gradient that extends outside the heater and generates a signal in the piezoresistive Wheatstone bridge.

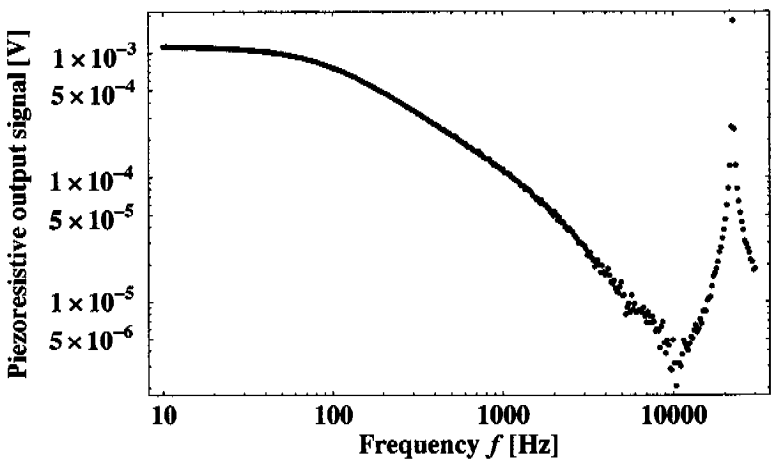

Fig. 4.13: Amplified output signal of the piezoresistive Wheatstone bridge as a function of the driving frequency f of the thermal actuation, while no force was applied to the tip.

Parallel to the vibrometer read-out, the signal from the integrated sensor was measured through the on-chip amplifier and also recorded on the gain-phase ana-

lyser. Fig. 4.13 shows the output signal from the piezoresistive Wheatstone bridge as a function of the frequency. The low-pass characteristic of the thermal actuation is visible, as well as the peak from the mechanical resonance. In between, around 10 kHz, there is a distinct dip in the sensor signal. In order to investigate the nature of the crosstalk, the ratio between the sensor signal and the actual vibration amplitude was calculated (see Fig. 4.14).

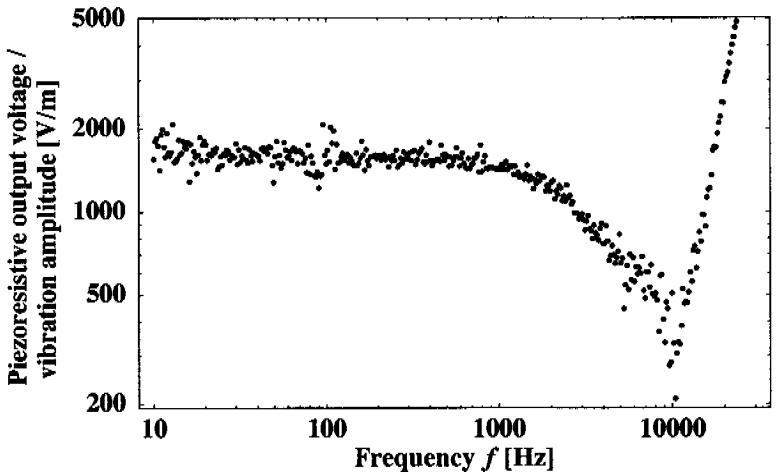

Fig. 4.14: Output signal of the piezoresistive Wheatstone bridge divided by the mechanical vibration amplitude measured with the vibrometer. Note that the mechanical resonance around 22 kHz does not appear distinctively in this ratio.

For low frequencies up to around 1 kHz, the cross-talk signal from the sensor is constant. For these frequencies the cross-talk is explained by the thermal gradient extending over the sensor bridge. Above 1 kHz the signal drops off, since the temperature oscillations created by the heater are more and more confined and do no longer reach the sensor. The steep rising slope from 10 kHz and onwards is expected to be the capacitive coupling between actuation and sensor connecting leads. The resonance frequency does not appear distinctively on this graph, since the augmented mechanical vibration amplitude due to resonance induces a corresponding proportional strain in the sensor elements, and the resulting ratio remains constant.

4.5 Four-Channel Parallel Array

This microsystem features, like the previously described design, an array of cantilevers and integrated electronics. However, in addition to the analogue electronics, extensive digital circuitry is included, in particular a digital controller for each scanning cantilever. Fig. 4.15 shows a photograph of the processed chip.

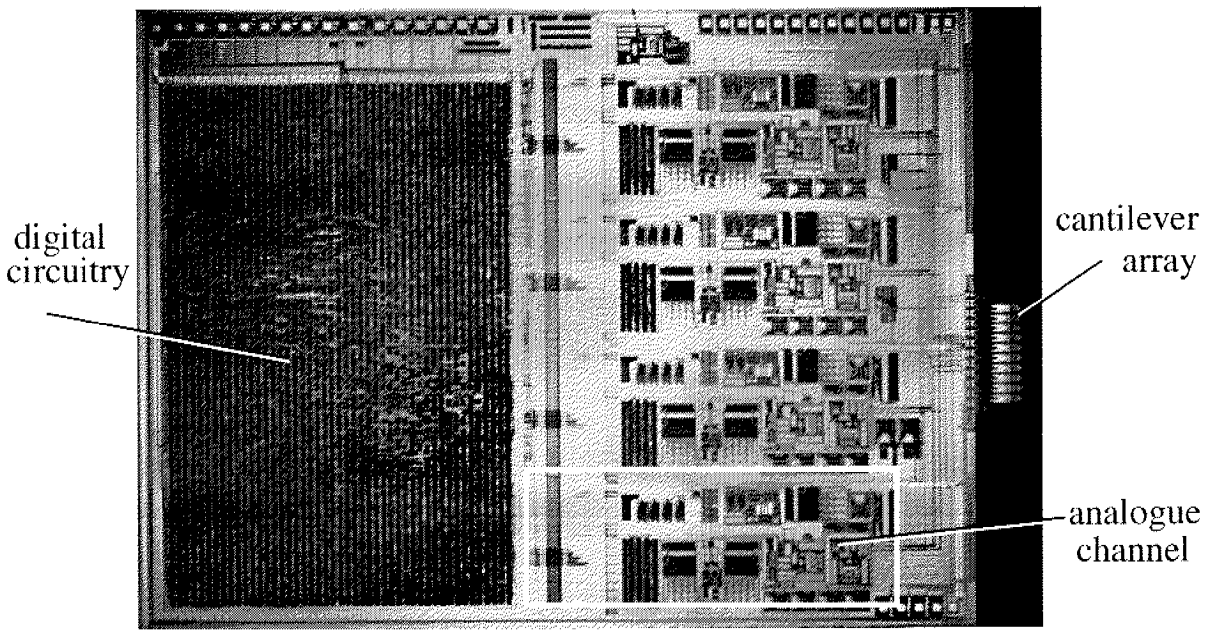

Fig. 4.15: Photograph of the monolithic AFM microsystem. The chip size is 7 mm x 10 mm. The cantilever array points out from the chip on the right side, the four analogue channels cover the right half of the chip, and the digital circuitry is in the dense block on the left half.

The cantilevers have piezoresistive force sensors and thermal actuators. Additional cantilever structures provide a first-order, self-adjusting compensation of the common offsets in the sensor array. Fully differential low-noise amplification stages are followed by pseudo-differential analogue-to-digital converters (ADC). Each scanning cantilever has its own programmable digital signal processing (DSP) unit, which acts as a controller for the cantilever deflection, via digital-to-analogue converters (DAC) and power drivers for the thermal actuation. The force and actuation signals are read out from the chip over its digital inter-

face, which also allows the programming of operation modes and controller parameters into the device.

4.5.1 Cantilever Design

Since the microsystem integrates the full sensing and actuation loop on-chip, the electronics must be well tailored to the characteristics of the cantilevers and its actuator and sensor elements. The basic cantilever construction was therefore preserved from the previous, well-characterized designs, with similar dimensions and with the same location of actuator and sensor elements. The rapid development pace of the commercial CMOS technology forced a change in the available technology from the foundry. For this design, a 0.8-μm, low-voltage process had to be chosen. Other than the lack of the deep n-well and the shallow p-well, this meant a change in some of the process parameters as well. For instance, the silicon part of the cantilever is made from the single available n-well of this process with a nominal junction depth of 3.5 μm. The full cantilever array can be seen in Fig. 4.16.

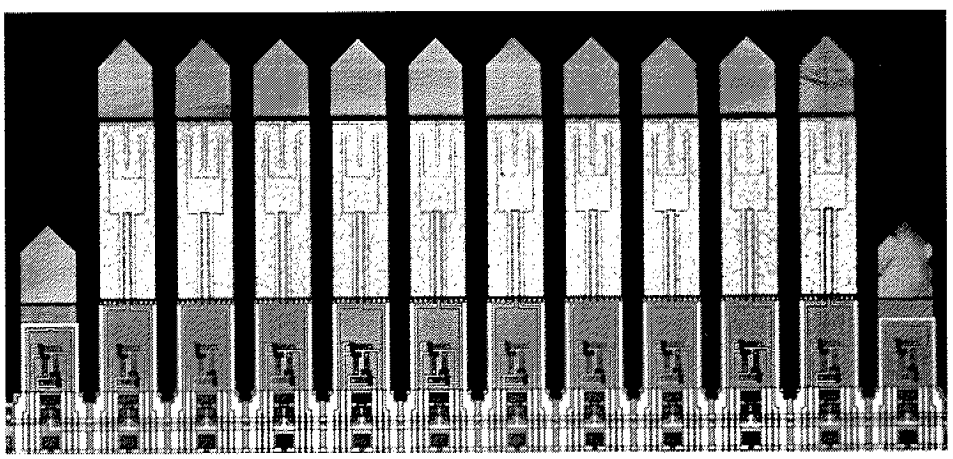

Fig. 4.16: Cantilever array with 500 µm long scanning cantilevers. The reference cantilevers on the sides are 250 µm long and provide automatic offset compensation.

Thermal Actuator

The actuator segment is 250 μm long and contains an additional reference resistor located in between the meanders of the heating resistor (see Fig. 4.17a). Since

the two resistors are of same composition and are heated to the same temperature, they exhibit the same relative heat-induced resistive change. This is used by the driving circuitry to provide precise heating power independent of the temperature [Barrettino2004].

The layer composition is as described in Section 4.2.2, with a silicon thickness of 3.5 μm and the double metal layer of 1.6 μm. The p^+ diffusion (400 nm deep) is used for the resistors. The resistance of the heating resistor is 1.3 kΩ, as measured on test cantilevers not connected to electronics.

Force Sensor

The same p^+ diffusion is used for the four piezoresistors of the force sensor, which are connected in a full Wheatstone bridge configuration (see Fig. 4.17b). In order to increase the resistance of the Wheatstone bridge while still maintaining a small footprint, each resistor is composed of two 20-μm-long, geometrically parallel, thin resistors in series using the minimum design width of 2 μm. The resulting resistance of the bridge, which is also equivalent to that of each resistor, is 900 Ω.

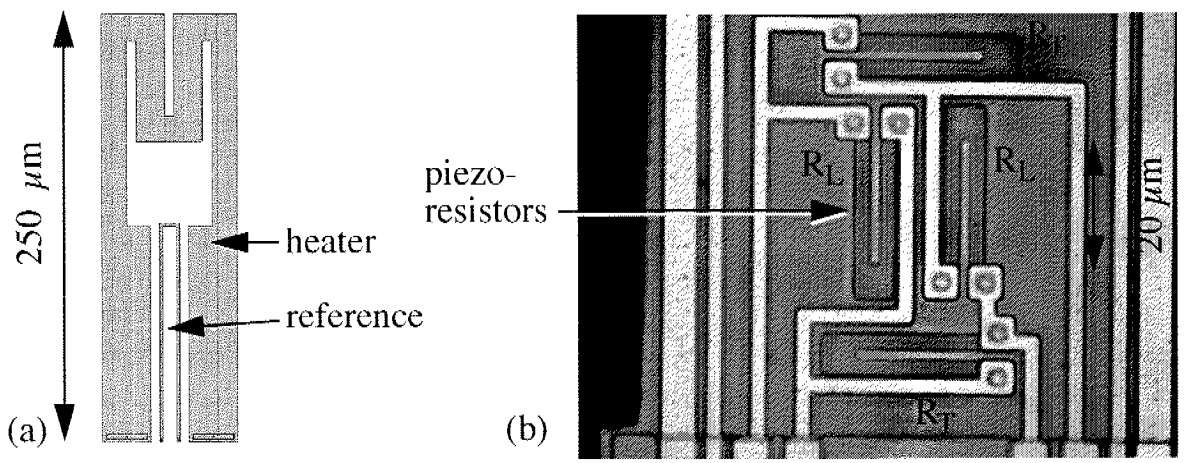

Fig. 4.17: (a) Actuator resistor design. The outer loop is the heater resistor, the smaller loop is the reference resistor for temperature compensation. (b) Force-sensing, piezoresistive Wheatstone bridge. Each resistor is a U-shaped diffusion of 2 µm width. Two resistors are longitudinal to the cantilever axis (R_L) and two are transverse (R_T).

REFERENCE CANTILEVER

As explained in Section 2.6.6, the release of the cantilevers causes an offset of the force sensor output due to different stress in the piezoresistors. This offset signal is in the order of 50 mV at 5 V bias; thus much higher than the force signals. The offset value is, however, systematic and equal for all the sensors, as long as the geometry of the cantilevers is the same. The sensor array therefore includes two reference cantilevers, whose purpose is to isolate the common offset. The reference cantilevers are situated at the sides of the cantilever array (see Fig. 4.16). They are only 250 μm long and will not touch the sample surface during scanning. The sensor part in the lower region of the cantilevers, and also the surrounding bulk structure, are identical to that of the scanning cantilevers. The signal from a reference cantilever is substracted from the signal of the scanning cantilevers after the first amplification stage, effectively eliminating most of the sensor offset. During the image-scanning experiments, no further offset compensation was needed.

4.5.2 SYSTEM DESIGN

Although a device with 10 independently scanning cantilevers can be technically fabricated, this first generation includes only 4 independent analogue channels to reduce the chip size. By further optimizing the circuitry, omitting non-critical features and test elements, a next generation design is expected to integrate ten channels. For future compatibility the array was therefore designed with ten scanning cantilevers, of which only four are activated by the integrated controllers. Except from the shared digital interface, all the analogue and digital components described in the following sections are duplicated for each channel to allow independent cantilever operation. The block diagram in Fig. 4.18 gives an overview of the components included on the chip.

ANALOGUE CIRCUITRY

The differential voltage signal from the Wheatstone bridge is first amplified by a programmable amplifier of gain 8 or 16, before the substraction of the equally amplified signal from the reference cantilever is carried out. The following anti-aliasing filter also includes a per-cantilever fine-adjustment of the offset whereby an 8-bit DAC provides a programmable compensating current. Another programmable gain stage (1x or 10x) is followed by a fixed gain stage (10x) before the signal is converted to digital by a 10-bit pseudo-differential ADC.

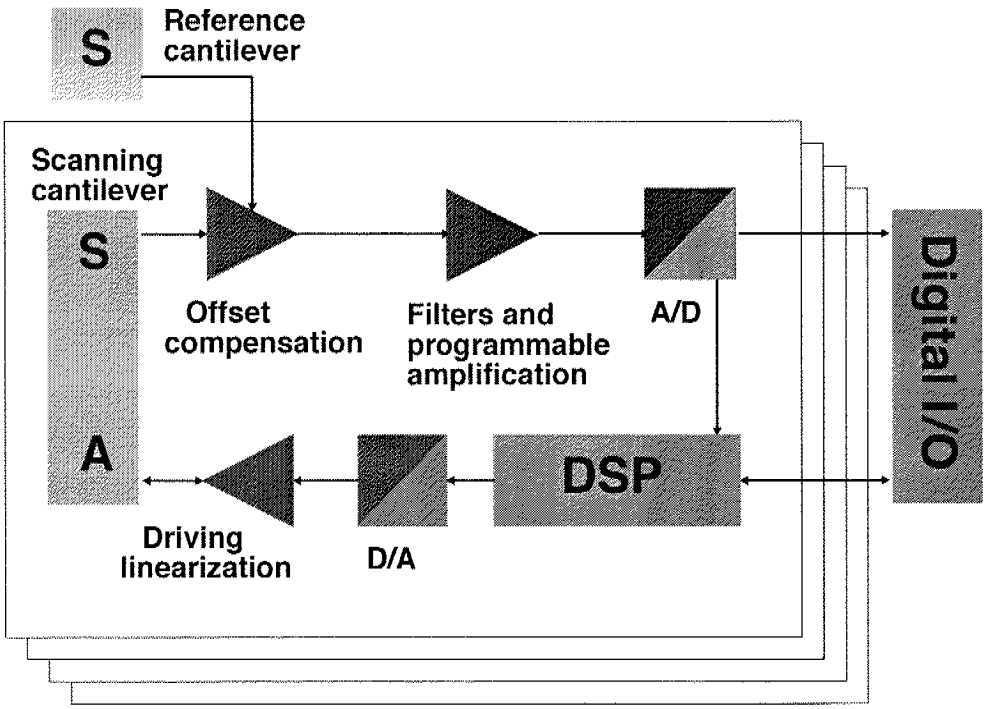

Fig. 4.18: Block diagram of the AFM system chip. S denotes the force sensor, and A denotes the thermal actuator. The feedback circuitry block is repeated for each scanning cantilever, whereas the reference cantilever and the digital interface block are shared.

The digital part (described in the next section) calculates the actuation signal which is converted to analogue by a 10-bit flash DAC. The driving circuitry includes a square-root builder in order to achieve a linear heating power in the thermal actuator as a function of the control-signal voltage.

The reference voltages for the ADC and DACs are provided externally, so that their working range can be adjusted in a flexible way according to the application. As an example, the forces are normally low when imaging in constant-force mode, but vary more when performing force-distance measurements.

Digital Signal Processing

The per-channel DSP unit comprises two infinite-impulse-response (IIR) filters to control the actuation in response to the force signal and the programmable set-point. The filters implement the formula

$$z_i = z_{i-1} + a \cdot z_{i-1} + b \cdot z_{i-2} + c \cdot v_i + d \cdot v_{i-1} + e \cdot v_{i-2} + f \cdot r \qquad (4.6)$$

where z is the actuation, v the measured force and r the reference value for the force (the set-force). a,b,c,d,e and f are 11-bit signed fixed-point coefficients. The filters store the previous two actuation and force signals between each iteration. The precision of the internal calculation is 16-bit. One multiplication and one addition are executed per clock cycle, requiring six cycles for the complete calculation. The true update rate of the actuation signal is limited by the ADC which needs 11 clock cycles per conversion. With a typical clock rate of 1 MHz, the update rate can therefore reach 91 kHz. The total calculation power of the on-chip filters is equivalent to 16 million arithmetic operations per second, one of the highest ever realized on a MEMS device.

The two filters can be programmed to perform different functions by choosing adequate coefficients. The first filter has been used to compensate for sensor-actuator coupling by substracting a low-pass-filtered fraction of the actuation signal from the sensor signal. The second filter has been used as a PID controller for constant-force imaging. As a simple example, an integrating controller can be implemented by choosing for instance c = -0.1, f = 0.1 and a,b,d,e zero (for a integration factor of 0.1): $z_i = z_{i-1} + 0.1 \cdot (r - v_i)$.

The coefficients a-f as well as the set-point force r are programmed over the digital, industry standard I^2C interface bus [Philips2005]. The first filter has individual coefficients per cantilever, the second uses a shared set. The I^2C bus is also used to select operation modes, amplification gains and output bit rates.

The force and actuation signals are read out from the chip over high-speed, serial lines. For open-loop operation (or an off-chip control loop) an actuation signal can be fed in through the serial input lines.

External Equipment

A piezo-scanner (Multimode, Veeco) was used as an x-y scanning stage. Since the chip provides the z-actuation, any precise x-y stage would be sufficient for operation. A printed circuit board provided stabilized power supply and reference voltages to the chip. The data from the chip were sent to a computer using a FPGA (field-programmable gate array) board that provided a high-speed serial link. The I^2C bus was connected to the same computer using a standard

I^2C-to-USB converter. A Labview^{TM} graphical interface was used to program the chip and visualize the data.

4.5.3 Cantilever Characterization

Characterization of the cantilevers was performed on test cantilevers that were not connected to any circuitry, in order to have direct access to actuator and sensor signals without influence from electronic components.

Actuation Frequency Response

The frequency response of the actuation was measured with a vibrometer as explained in Section 4.4.3. Fig. 4.19 shows a frequency scan from 10 Hz to 100 kHz. The overall response is similar to that of the cantilevers described in Section 4.4, however the resonance frequency is higher (43 kHz). This can be explained by the change of process parameters with layers of different thickness and profile. In this design, the single n-well depth and the resulting cantilever thickness is uniform along the length of the cantilevers.

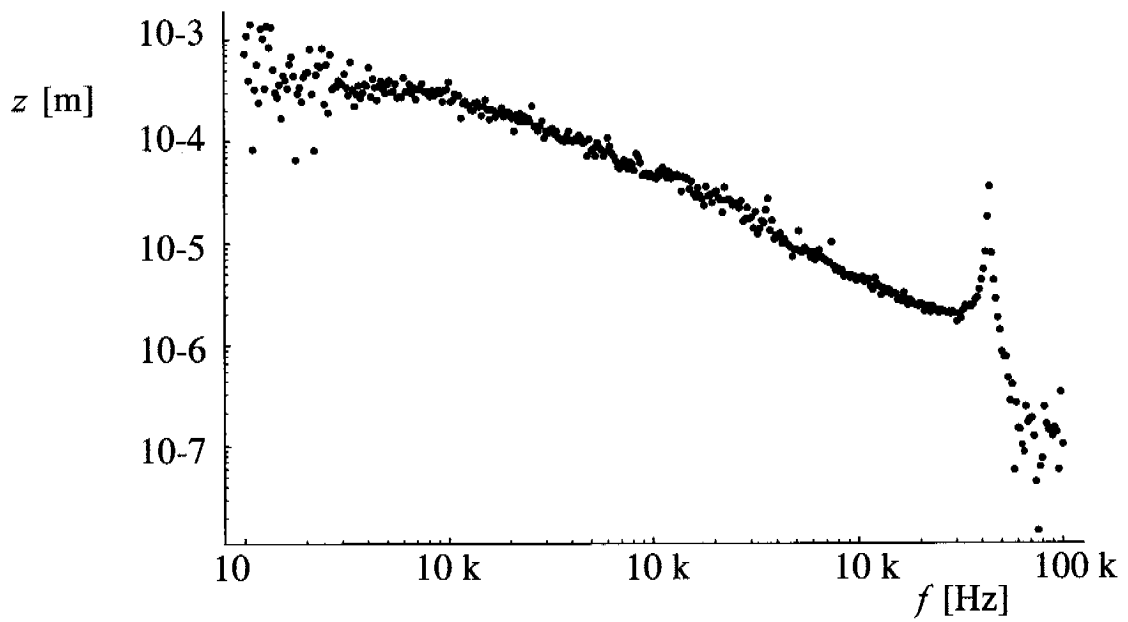

Fig. 4.19: Vibration amplitude z as a function of frequency for a thermally actuated cantilever. The applied dynamic heating power is P_ω = 1.32 mW. The resonance frequency is seen at 43 kHz.

The data were fit to the actuation-response model presented in Section 4.2.4. The resulting parameters and the fitted curve together with the measured data are seen in Tab. 4.3 and Fig. 4.20, respectively.

Tab. 4.3: Extracted parameters from fitting the model in Section 4.2.4 to the measured frequency response.

ω_0 [s^{-1}]	δ	ω_c [s^{-1}]	K [m/W]
266300	367	576	$4 \cdot 10^{-3}$

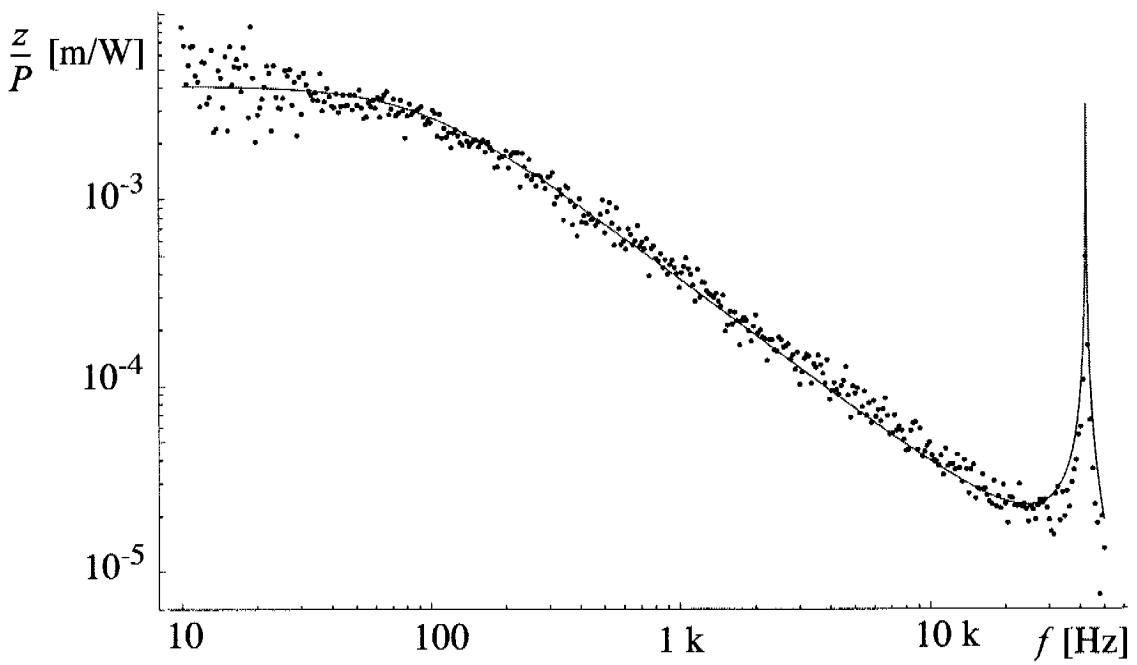

Fig. 4.20: Actuation efficiency (vibration amplitude z per driving power P) as a function of frequency. Superposition of the fit curve (grey line) and the measured data (black dots).

ACTUATION EFFICIENCY

The actuation efficiency was determined with the help of a piezotube as explained in Section 4.4.3. The efficiency was found to be 250 μm/W. The linearity of the actuation was verified by applying several heating-power steps up to 6 mW and by stepping the piezotube accordingly to track the deflections (see Fig. 4.21). The drift and creep of the piezo-tube limits the precision of this method for higher actuation amplitudes than 1 μm.

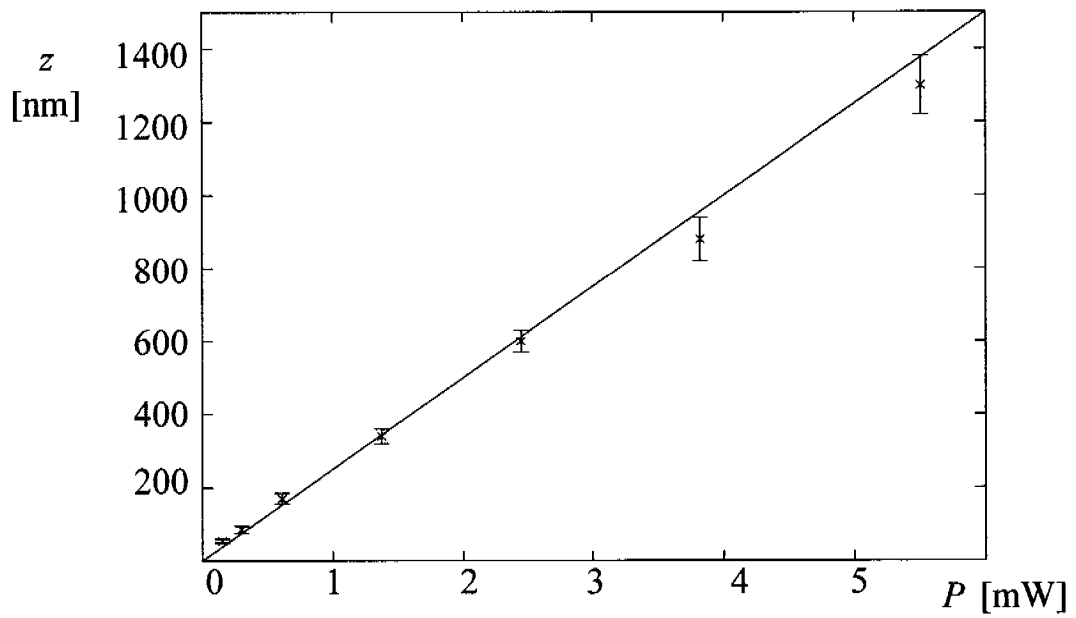

Fig. 4.21: Cantilever deflection z as a function of the heating power P.

SENSITIVITY

The sensitivity of the force sensor was measured by bending the cantilever with a piezotube and reading out the resulting voltage from the Wheatstone bridge. With a biasing of the bridge of 5 V, the sensitivity was 5 μV/nm, thus a deflection sensitivity of 1 μV/nm/V.

4.5.4 FORCE-DISTANCE MEASUREMENTS

For force-distance measurements, the AFM system is operated in open-loop mode. An actuation signal is fed to the chip and the force signal is read out while the cantilever tip is cycled towards and away from the sample (see Fig. 4.22). As the tip comes in contact and is pressed against the sample surface (b), the meas-

ured force is a result of the combined stiffness of the cantilever and the tip-sample interaction. For hard tips and surfaces, the slope of the force versus the distance translates into the stiffness k of the cantilever. When the cantilever is retracted from the surface (c), the tip stays attached due to adhesion forces and pulls on the cantilever. At the snap-off point (d) the tip is released and the cantilever is freely moving without interaction (e). A smaller pull-in force can also be

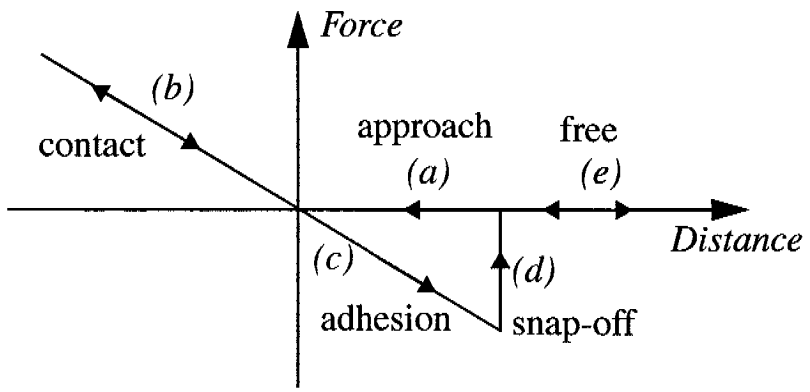

Fig. 4.22: Idealized force-distance measurement curve: (a) the tip is approaching the surface, (b) after contact, the cantilever is bent against the (hard) surface, (c) the tip is stuck to the surface as the cantilever retracts, (d) the tip "snaps" off, (e) the cantilever is free.

observed, just as the tip reaches the surface. The snap-off and pull-in forces are for measurements in air dominated by the capillary effects of the thin water film covering most surfaces.

The quantification of these forces is useful for surface analysis and it is of more interest to have a well defined contact area, than to achieve a smallest possible one [Franks2002]. The measurements were therefore performed using spherical glass beads with a known, accurate diameter, which were mounted on the cantilever end to act as the contact tip. Glass beads of 20 μm diameter were glued using an epoxy (see Fig. 4.23a) providing an estimated contact area of 0.03 μm^2. The beads were left uncoated.

The sample surfaces analysed were small glass chips with gold patterns, which were coated with either a methyl-terminated or an amino-terminated undecanethiol self-assembled monolayer (SAM). Fig. 4.23b shows the force-distance

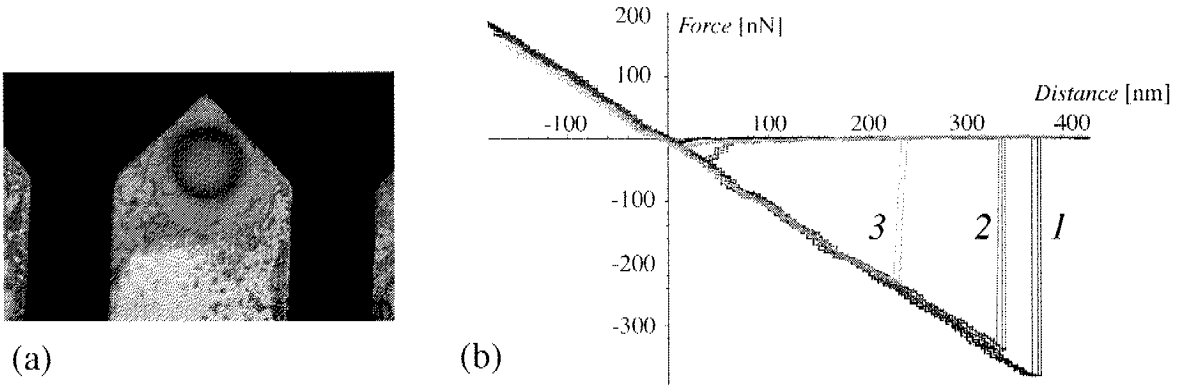

Fig. 4.23: (a) Glass bead of 20 µm diameter mounted on a cantilever for surface analysis [Hafizovic2004]. (b) Force-distance plots for different samples: 1=glass, 2=amino-terminated SAM on glass, 3=methyl-terminated SAM on glass.

curves for the two SAM surfaces as well as for an uncoated glass surface. Four consecutive cycles (approach and lift-off) are displayed. Both pull-in and snap-off forces are visible. The snap-off force is strongest for the uncoated glass surface and stronger for the amino-terminated SAM than for the methyl-terminated SAM. This agrees well with the fact that glass is hydrophilic due to surface hydroxyl groups, the amino-groups are less hydrophilic, and the methyl-groups are non-polar and hydrophobic [Hafizovic2004].

4.5.5 Constant-Force Imaging

For imaging, the chip was operated with the built-in IIR filters programmed for PID control. The chip regulates the actuation power in order to keep the cantilever tip in contact with the sample, with a constant applied force given by the reference force values r. The read-out actuation signal will therefore follow the topography of the sample while the cantilever is moved over the surface. The error signal, the difference between the measured force signal and the reference force, can also be read out through the serial lines.

Fig. 4.24a shows the scanned image of a silicon calibration grating. The step height is 18 nm and the pitch of the grooves is 3 μm. The scanning speed was 20 μm/s, and the reference force was 50 nN. The IIR filters were also used to perform on-chip real-time averaging of 300 data samples. The profile of a single line scan across the step, recorded at 3 μm/s is shown in Fig. 4.24, which demon-

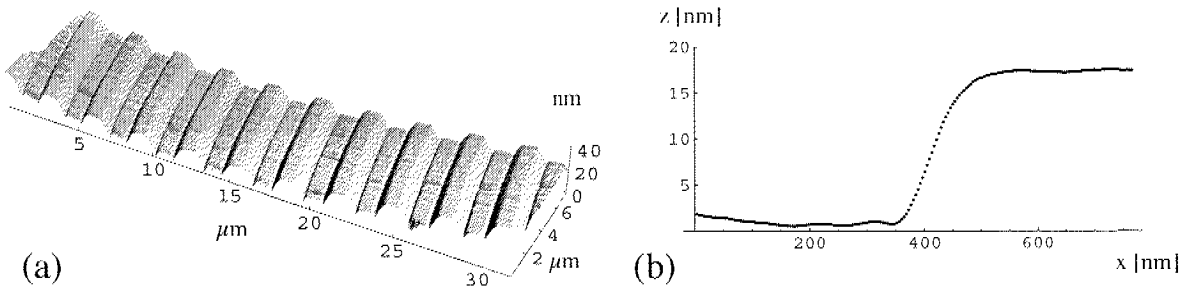

Fig. 4.24: (a) Scanned image of a silicon calibration grating. The step height is 18 nm, and the pitch is 3 μm. (b) Profile of a single line scan across the step.

strates a good tracking and vertical resolution of less than 1 nm [Hafizovic2004]. Silicon nitride tips were used for these experiments (see Section 4.3.2).

The scanned image of a soft, biological sample is shown in Fig. 4.25a. The sample is a dried-out network of chicken neurites on a silicon oxide surface. The reference force was 10 nN and the scanning speed 100 μm. For comparison, an optical microscope image of the same structure is shown in Fig. 4.25b.

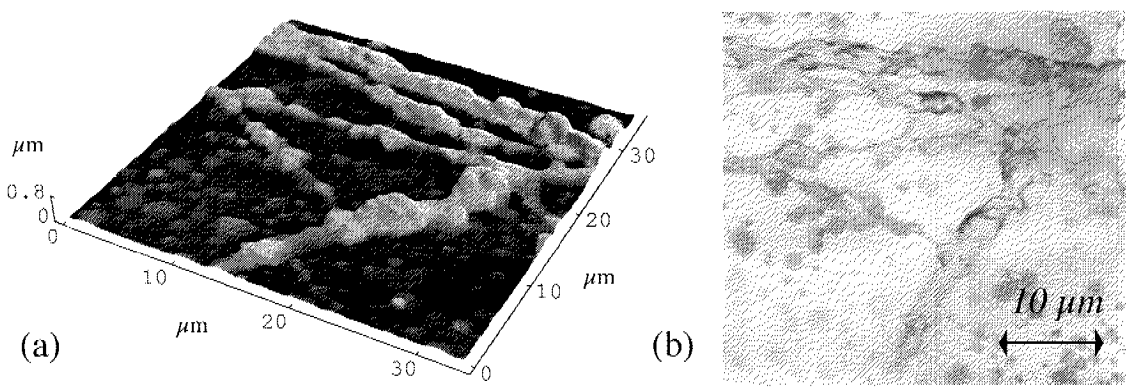

Fig. 4.25: (a) Dried-out network of chicken neurites, recorded in constant-force-mode. (b) Optical microscope image of the same sample [Hafizovic2004].

5 CONCLUSION AND OUTLOOK

SUMMARY

Multi-cantilever, CMOS-based microsensor systems for two different applications have been designed, fabricated and characterized. The first system features an array of surface-stress sensing cantilevers. Although primarily targeted for liquid, biomolecular detection, it has been demonstrated as a versatile platform also for other measurements involving change of surface-stress including humidity and volatile-organic-compound (VOC) detection with the use of polymer coating. The second device is a complete system for AFM imaging featuring an array of self-sensing and self-actuating cantilevers. Both systems integrate on a single CMOS chip the sensor elements together with comprehensive electronic circuitry for enhanced functionality and flexibility.

Certain general technical aspects and challenges are common to the two systems. The combination of microcantilevers and piezoresistive detection has been shown to be an efficient way of creating highly sensitive devices. These devices have been realized using standard, industrial CMOS processing and subsequent micromachining. The array designs can be easily scaled to any number of cantilevers. The post-CMOS processing has been improved through new processing technologies targeted at protecting fine, fragile microstructures during critical operations, such as wafer dicing.

The direct integration of high-gain amplification on the sensor chip poses challenges in respect to sensor offsets. The use of Wheatstone bridges, crucial for the reduction of cross-sensitivities, has been refined to highly symmetrical configurations. This translates into minimized signal offsets, as well as a reduced influence from stray noise and common-mode disturbance.

The fabricated surface-stress sensing system allows single-cantilever measurements as well as symmetric, dual-cantilever configurations. In the latter case one cantilever acts as a reference cantilever. Each cantilever has dimensions of 300 μm x 300 μm and features two diffused, 10-kΩ resistors. The on-chip cir-

cuitry consists of an input multiplexer, a low-noise chopper amplifier, a low-pass filter, additional gain stages and output buffers. The total gain (between 49 and 67 dB) can be selected. Deflection measurements show a sensor sensitivity of 0.74 μm/nm/V. The input-referred noise level of the circuitry is 0.43 μV in the range of 50 mHz to 10 Hz. Coated with a polymer, the sensors were used for humidity sensing and VOC detection.

Previous AFM designs were fully characterized in order to understand the dynamic behaviour of thermally actuated cantilevers. These prerequisite studies led to the design of a new, integrated cantilever-control system. The new AFM system features 500-μm-long scanning cantilevers with integrated thermal actuators (for height actuation) and piezoresistive force sensors. Reference cantilevers of 250 μm eliminate the inherent sensor offset arising from the built-in stress of the surface layers. The analogue, fully-differential amplifier chain has a selectable gain between 38 and 64 dB. The digital-signal-processing unit provides programmable, closed-loop control of the cantilever actuation for constant-force imaging. Four cantilevers can be controlled independently by individual controllers. A digital interface is used for reading out the data and for programming operating parameters. Image scanning experiments in constant-force mode show a height resolution of 1 nm. Other operation modes allow, for instance, force-distance measurements which have been demonstrated for surface analysis.

Outlook - Surface-Stress Sensor System

Testing of the surface-stress sensing systems in a liquid environment has revealed many technological challenges. Leak-proof protection of circuitry and connections suitable for mass-production will have to be developed. The electrical potential between the silicon bulk and the cantilever, due to the biased n-well, can cause electrochemical reactions. This could be reduced by alternative resistor or cantilever designs.

Optimized design of the cantilevers and flow chamber would result in reduced sensor flow sensitivity. Conversely, the flow-sensitivity can also be exploited for a new type of flow sensor. For stopped-flow measurements, alternative pumps could reduce the stabilization time, thus improving the signal acquisition. As a long-term perspective, the addition of integrated pumps and filters to the sensor system can lead to a full μTAS device.

In this thesis, the system performance has been throroughly investigated using physicochemical model tests which could be easily performed in a repetitive fashion. This builds the foundation for investigating biochemical assays in the future. The first results in this direction do not show sufficient reproducibility yet, but once the functionalization of the sensor surface can be performed in a more reliable way, reproducible detection of biomolecules is expected.

OUTLOOK - AFM ARRAY SYSTEM

The AFM system is currently limited by the capacity of the external interface. A custom-made, real-time data acquisition program is needed to fully exploit the data rates available from the chip, especially for parallel scanning. The signal-to-noise ratio can be improved by further buffering and shielding of the power supplies and off-chip connections. The power consumption of the thermal actuation currently causes internal crosstalk, which can be solved by a symmetric driving architecture. The footprint of the circuitry can be reduced by eliminating test facilities and non-critical functionality. This will allow additional control channels and true parallel operation of more cantilevers within the same chip dimensions. The lateral resolution is limited by the tip quality, and although the use of additional tips has been demonstrated, a sharper integrated tip is desirable.

Integrated elements on the cantilevers can provide additional sensing functions for other scanning probe techniques, such as electric force microscopy. The chip can serve as a base instrument for a range of micro- and nanoscale force interaction studies. Provided they are CMOS-compatible, post-processing techniques can be added to achieve batch fabrication of tips and functionalization features.

The compact size and complete functionality makes this chip a candidate for integration in other systems where force scanning is desired. With high-volume CMOS fabrication, the chip could constitute the heart of a low-cost AFM system, expanding further the exploitation of nanoscale imaging into new applications and markets.

REFERENCES

[Akiyama1999] T. Akiyama, U. Staufer, N. F. de Rooij, "Wafer- and piece-wise Si tip transfer technologies for applications in scanning probe microscopy", *IEEE Journal of Microelectromechanical Systems* 8 (1999) pp. 65–70.

[Akiyama2000] T. Akiyama, U. Staufer, N. F. de Rooij, D. Lange, C. Hagleitner, O. Brand, H. Baltes, A. Tonin, H. R. Hidber, "Integrated atomic force microscopy array probe with metal-oxide-semiconductor field effect transistor stress sensor, thermal bimorph actuator, and on-chip complementary metal-oxide-semiconductor electronics", *Journal of Vacuum Science and Technology* B 18 (2000) pp. 2669–2675.

[Akiyama2002] T. Akiyama, U. Staufer, N. F. de Rooij, "Fast driving technique for integrated thermal bimorph actuator toward high-throughput atomic-force microscopy", *Review of Scientific Instrumentation* 73 (2002) pp. 2643–2646.

[Alvarez2005] M. Alvarez, J. Tamayo, "Optical sequential readout of microcantilever arrays for biological detection", *Sensors and Actuators B: Chemical* (in press, available online).

[Ansys2004] Ansys University Advanced release 8.1, ANSYS, Inc., Canonsburg (PA), USA.

[Baltes1996] H. Baltes, "Future of IC microtransducers", *Sensors and Actuators A: Physical* 56 (1996) pp. 179–192.

[Bao2000] M.-H. Bao, "Micro Mechanical Transducers - Pressure Sensors, Accelerometers and Gyroscopes" (Handbook of Sensors and Actuators 8), Elsevier 2000.

[Barrettino2004] D. Barrettino, "CMOS Readout and Control Architectures for Monolithic Hotplate and Cantilever Microsystems", Ph.D. thesis (no. 15412), ETH Zurich, Switzerland, 2004.

[Battiston2001] F.M.Battiston, J.-P.Ramseyer, H.P.Lang, M.K.Baller, C.Gerber, J.K.Gimzewski, E.Meyer and H.-J.Güntherodt, "A chemical sensor based on a microfabricated cantilever array with simultaneous resonance-frequency and bending readout", *Sensors and Actuators B: Chemical* 77 (2001) pp.122–131.

[Binnig1982] G.Binnig, H.Rohrer, C.Gerber, E.Weibel, "Surface Studies by Scanning Tunneling Microscopy", *Physical Review Letters* 49 (1982) pp.57–61.

[Binnig1986] G.Binnig, C.F.Quate, C.Gerber, "Atomic force microscope", *Physical Review Letters* 56 (1986) pp.930–933.

[Boisen2000] A.Boisen, J.Thaysen, H.Jensenius, O.Hansen, "Environmental sensors based on micromachined cantilevers with integrated read-out", *Ultramicroscopy* 82 (2000) pp.11–16.

[Boltshauser1993] T.Boltshauser, "CMOS Humidity Sensors", Ph.D. thesis (no.10320), ETH Zurich, Switzerland, 1993.

[Brand1992] O.Brand, H.Baltes, U.Baldenweg, "Thermally excited silicon oxide bridge resonators in CMOS technology", *Journal of Micromechanical Microengineering* 2 (1992) pp.208–210.

[Buchhold1998] R.Buchhold, A.Nakladal, G.Gerlach, P.Neumann, "Design studies on piezoresistive humidity sensors", *Sensors and Actuators B: Chemical* 53 (1998) pp.1–7.

[Cadence2000] Custom IC Design Tools (4.4.6), Cadence Design Systems, Inc., San Jose (CA), USA

[Cammarata1994] R.C.Cammarata, "Surface And Interface Stress Effects In Thin Films", *Progress in Surface Science* 46 (1994) pp.1–38.

[Castle1997] J.E.Castle, P.A.Zhdan, "Characterization of surface topography by SEM and SFM: problems and solutions", *Journal of Physics D: Applied Physics* 30 (1997) pp.722–740.

[Chen1995] G.Y.Chen, T.Thundat, E.A.Wachter, R.J.Warmack, "Adsorption-induced surface stress and its effects on resonance frequency of microcantilevers", *Journal of Applied Physics* 77 (1995) pp.3618–3622.

[Chu1993] W.H.Chu, M.Mehregany, R.L.Mullen, "Analysis of tip deflection and force of a bimetallic cantilever microactuator", *Journal of Micromechanical Microengineering* 3 (1993) pp.4–7.

[Davies1994] J.Davies, A.C.Dawkes, A.G.Haymes, C.J.Roberts, R.F.Sunderland, M.J.Wilkins, M.C.Davies, S.J.B.Tendler, D.E.Jackson and J.C.Edwards, "A scanning tunneling microscopy comparison of passive antibody adsorption and biotinylated antibody linkage to streptavidin on microtiter wells", *Journal of Immunological Methods* 167 (1994) pp.263–269.

[Eigler1990] D.M.Eigler, E.K.Schweizer, "Positioning single atoms with a scanning tunnelling microscope", *Nature* 344 (1990) pp.524–526.

[Franks2002] W.Franks, D.Lange, S.Lee, A.Hierlemann, N.Spencer, H.Baltes, "Nanochemical surface analyzer in CMOS technology", *Ultramicroscopy* 91 (2002) pp.21–27.

[Fritz2000] J.Fritz, M.K.Baller, H.P.Lang, H.Rothuizen, P.Vettiger, E.Meyer, H.-J.Güntherodt, Ch.Gerber, J.K.Gimzewski, "Translating Biomolecular Recognition into Nanomechanics", *Science* 288 (2000) pp.316–318.

[Gere1997] J.M.Gere, S.P.Timoshenko, "Mechanics of Materials", PWS Publishing Company, Boston, 1997.

[Ghatnekar2005] S.Ghatnekar-Nilsson, E.Forsén, G.Abadal, J.Verd, F.Campabadal, F.Pérez-Murano, J.Esteve, N.Barniol, A.Boisen, L.Montelius, "Resonators with integrated CMOS circuitry for mass sensing applications, fabricated by electron beam lithography", *Nanotechnology* 16 (2005) pp.98–102.

[Gutman1995] E.M.Gutman, "On the thermodynamic definition of surface stress", *Journal of Physics: Condensed Matter* 7 (1995) pp.663–667.

[Hafizovic2004] S.Hafizovic, D.Barrettino, T.Volden, J.Sedivy, K.-U.Kirstein, O.Brand, A.Hierlemann, "Single-chip mechatronic microsystem for surface imaging and force response studies", Proceedings of the National Academy of Science 101 (2004) pp.17011–17015.

[Hagleitner1999] C. Hagleitner, D. Lange, T. Akiyama, A. Tonin, R. Vogt, H. Baltes, "On-chip circuitry for a CMOS parallel scanning AFM", in: *Proc. SPIE* 3673 (1999) pp. 240–248.

[Han1996] W. Han, S. M. Lindsay, "A magnetically driven oscillating probe microscope for operation in liquids", *Applied Physics Letters* 69 (1996) pp. 4111–4113.

[Hansen1999] O. Hansen, A. Boisen, "Noise in piezoresistive atomic force microscopy", *Nanotechnology* 10 (1999) pp. 51–60.

[Hecht2000] B. Hecht, B. Sick, U. P. Wild, V. Deckert, R. Zenobi, O. J. F. Martin, D. W. Pohl, "Scanning near-field optical microscopy with aperture probes: Fundamentals and applications", *Journal of Chemical Physics* 112 (2000) pp. 7761–7774.

[Jensenius2002] H. Jensenius, "Microcantilever-based studies of bio/chemical systems", Ph.D. thesis, Mikroelektronik Centret, Technical University of Denmark, 2002.

[Juillerat1999] C. Juillerat, "Optimization of CMOS AFM Cantilevers", Diploma thesis, Physical Electronics Laboratory, ETH, Zurich, Switzerland, 1999.

[Kloeck1989] B. Kloeck, S. D. Collins, N. F. de Rooij, R. L. Smith, "Study of electrochemical etch-stop for high-precision thickness control of silicon membranes", *IEEE Transactions on Electron Devices* 36 (1989) pp. 663–669.

[Koll1999] A. Koll, "CMOS Capacitive Chemical Microsystems for Volatile Organic Compounds", Ph.D thesis (no. 13460), ETH Zurich, Switzerland, 1999.

[Lammerink1990] T. S. J. Lammerink, M. Elwenspoek, R. H. Van Ouwerkerk, S. Bouwstra, J. H. J. Fluitman, "Performance of Thermally Excited Resonators", *Sensors and Actuators A: Physical* 21 (1990) pp. 352–356.

[Lammerink1991] T.S.J.Lammerink, M.Elwenspoek and J.H.J.Fluitman, "Frequency dependence of thermal excitation of micromechanical resonators", *Sensors and Actuators A: Physical* 27 (1991) pp.699–703.

[Lange2001] D.Lange, M.Zimmermann, C.Hagleitner, O.Brand, H.Baltes, "CMOS 10-cantilever array for constant-force parallel scanning AFM", in: *Proceedings of Transducers'01/Eurosensors XV*, Munich, Germany, 2001, pp.1074–1077.

[Lange2002] D.Lange, O.Brand, H.Baltes, "CMOS Cantilever Sensor Systems", Springer-Verlag, Berlin, 2002.

[Lange2003] D.Lange, C.Hagleitner, C.Herzog, O.Brand and H.Baltes, "Electromagnetic actuation and MOS-transistor sensing for CMOS-integrated micromechanical resonators", *Sensors and Actuators A: Physical* 103 (2003) pp.150–155.

[Marcus1990] R.B.Marcus, T.S.Ravi, T.Gmitter, K.Chin, D.Liu, W.J.Orvis, D.R.Ciarlo, C.E.Hunt, and J.Trujillo, "Formation of silicon tips with <1 nm radius", *Applied Physics Letters* 56 (1990) pp.236–238.

[McKendry2002] R.McKendry, J.Zhang, Y.Arntz, T.Strunz, M.Hegner, H.P.Lang, M.K.Baller, U.Certa, E.Meyer, H.-J.Güntherodt, C.Gerber, "Multiple label-free biodetection and quantitative DNA-binding assays on a nanomechanical cantilever array", *Proceedings of the National Science Academy* 99 (2002) pp.9783–9788.

[Meyer1988] G.Meyer, N.M.Amer, "Novel optical approach to atomic force microscopy", *Applied Physics Letter* 53 (1988) pp.1045–1047.

[Minne1998] S.C.Minne, G.Yaralioglu, S.R.Manalis, J.D.Adams, J.Zesch, A.Atalar, C.F.Quate, "Automated parallel high-speed atomic force microscopy", *Applied Physics Letters* 72 (1998) pp.2340–2342.

[Minne1998] S.C.Minne, J.D.Adams, G.Yaralioglu, S.R.Manalis, A.Atalar, C.F.Quate, " Centimeter scale atomic force microscope imaging and lithography", *Applied Physics Letters* 73 (1998) pp.1742–1744.

[Minne1999] S.C.Minne, S.R.Manalis, C.F.Quate, "Bringing Scanning Probe Microscopy up to Speed", Kluwer Academic Publishers, Boston, 1999.

[Müller2000] T.Müller, M.Brandl, O.Brand, H.Baltes, "An industrial CMOS process family adapted for the fabrication of smart silicon sensors", *Sensors and Actuators A: Physical* 84 (2000) pp.126–133.

[Nathan1999] A.Nathan, H.Baltes, "Microtransducer CAD -Physical and Computational Aspects" (Computational Microelectronics), Springer 1999.

[Ning1995] Y.Ning, Y.Loke, G.McKinnon, "Fabrication and characterization of high g-force, silicon piezoresistive accelerometers", *Sensors and Actuators A: Physical* 48 (1995) pp.55–61.

[Ono2002] M.Ono, D.Lange, O.Brand, C.Hagleitner, H.Baltes, "A complementary-metal-oxide-semiconductor-field-effect-transistorcompatible atomic force microscopy tip fabrication process and integrated atomic force microscopy cantilevers fabricated with this process", *Ultramicroscopy* 91 (2002) pp.9–20.

[Paci2003] D.Paci, "Modelling and simulation of cantilever based chemical sensors", Student thesis, Scuola Superiore Sant'Anna, Pisa, Italy, 2003.

[Parameswaran1989] M.Parameswaran, H.P.Baltes, Lj.Ristic, A.C.Dhaded, A.M.Robinson, "A New Approach For The Fabrication Of Micromechanical Structures", *Sensors and Actuators* 19 (1989) pp.289–307.

[Perrin1997] A.Perrin, Ph.D. thesis, University Claude Bernard - Lyon 1, France, 1997.

[Philips2005] Philips Semiconductors I^2C-bus Information, <http://www.semiconductors.philips.com/buses/i2c/>

[Rasmussen2003] P.A.Rasmussen, J.Thaysen, O.Hansen, S.C.Eriksen, A.Boisen, "Optimised cantilever biosensor with piezoresistive read-out", *Ultramicroscopy* 97 (2003) pp.371–376.

[Roberts1981] R.B.Roberts, "Thermal expansion reference data: silicon 300–850 K", *Journal of Physics D: Applied Physics* 14 (1981) pp.163–166.

[Sarid1994] D.Sarid, "Scanning Force Microscopy", Oxford University Press, New York, 1994.

[Savran2003] C.A.Savran, T.P.Burg, J.Fritz, S.R.Manalis, "Microfabricated mechanical biosensor with inherently differential readout", Applied Physics Letters 83 (2003) pp.1659–1661.

[Schramm1987] W.Schramm, T.Yang, A.R.Midgley, "Surface modification with protein A for uniform binding of monoclonal antibodies", *Clinical Chemistry* 33 (1987) pp.1338–1342.

[Sensonor2005] Sensonor SP12 TPM sensor, <http://www.sensonor.no>, Sensonor, Horten, Norway.

[Smith1954] C.S.Smith, "Piezoresistance effect in germanium and silicon", *Physical Review* 94 (1954) pp.42–49.

[Song2005] W.H.Song, "Packaging Techniques for CMOS-based Chemical and Biochemical Microsensors", Ph.D. thesis (No.15987), ETH Zurich, Switzerland, 2005.

[Staufer2000] U.Staufer, T.Akiyama, C.Beuret, S.Gautsch, W.Noell, G.Schürmann, C.Stebler, N.F.deRooij, "Micro-electromechanical systems for nanoscience", *Journal of Nanoparticle Research* 2 (2000) pp.413–418.

[Stoney1909] G.C.Stoney, "The Tension of Metallic Films Deposited by Electrolysis", *Proceedings of the Royal Society of London* A82 (1909) pp.172–175.

[Thaysen2001] J.Thaysen, "Cantilever for Bio-Chemical Sensing Integrated in a Microliquid Handling System", Ph.D. thesis, Mikroelektronik Centret, Technical University of Denmark, 2001.

[Thundat1995] T. Thundat, G. Y. Chen, R. J. Warmack, D. P. Allison, E. A. Wachter, "Vapor Detection Using Resonating Microcantilevers", *Analytical Chemistry* 67 (1995) pp. 519–521.

[Timoshenko1987] S. Timoshenko, S. Woinowsky-Krieger, "Theory of Plates and Shells" (Second Edition), McGraw-Hill, New York, 1987.

[Tortonese1991] M. Tortonese, H. Yamada, R. C. Barrett, C. F. Quate, "Atomic force microscopy using piezoresistive cantilever", in: *Proceedings of Transducers'91*, San Francisco, USA, 1991, pp. 448–451.

[Veeco2005] DMASP - Micro-actuated Silicon Probes for Fast Scanning and Ideal Resonances, <https://www.veecoprobes.com>, Veeco Instruments, Santa Barbara (CA), USA.

[Vettiger2002] P. Vettiger et al, "The "millipede" - nanotechnology entering data storage", *IEEE Transactions on Nanotechnology* 1 (2002) pp. 39–55.

[Villarroya2004] M. Villarroya, F. Pérez-Murano, C. Martín, Z. Davis, A Boisen, J. Esteve, E. Figueras, J. Montserrat, N. Barniol, "AFM lithography for the definition of nanometre scale gaps: application to the fabrication of a cantilever-based sensor with electrochemical current detection", *Nanotechnology* 15 (2004) pp. 771–776.

[Volden2004] T. Volden, M. Zimmermann, D. Lange, O. Brand, H. Baltes, "Dynamics of CMOS-based Thermally Actuated Cantilever Arrays for Force Microscopy", *Sensors and Actuators A: Physical* 115 (2004) pp. 516–522.

[Wong2003] H. Wong, "Low-frequency noise study in electron devices: review and update", *Microelectronics Reliability* 43 (2003) pp. 585–599.

[Wu2001] G. Wu, H. Ji, K. Hansen, T. Thundat, R. Datar, R. Cote, M. F. Hagan, A. K. Chakraborty, A. Majumdar, "Origin of nanomechanical cantilever motion generated from biomolecular interactions", *Proceedings of the National Science Academy* 98 (2001) pp. 1560–1564.

CURRICULUM VITAE

Tormod Volden

Born 09.12.1971

Citizen of Norway

Professional experience

2000–2005	ETH Zurich, Physical Electronics Laboratory. Research assistant and PhD student under supervision of Prof. Dr. Henry Baltes.
1996–2000	DNR (The Norwegian Radium Hospital), Oslo. Research engineer in the department of medical physics and technology.
1995–1996	FFI (The Norwegian Defence Research Institute), department of electronics. National service as research assistent.
1995	SINTEF research centre in Oslo, department of instrumentation. Diploma work and research, 5 months.
1994	Daniel den Hoed Cancer Center, Rotterdam, The Netherlands, department of radiotherapy. 3 months placement.

Education

1997	Postgraduate course in biomedical instrumentation, University of Oslo.
1990–1995	Institut National des Sciences Appliquées (INSA) Toulouse, France. Graduated as *Ingénieur Diplômé* from the department of material physics and instrumentation.

PUBLICATIONS

JOURNAL PAPERS

- T. Volden, M. Zimmermann, D. Lange, O. Brand, H. Baltes, "Dynamics of CMOS-based thermally actuated cantilever arrays for force microscopy", *Sensor and Actuators A: Physical* 115 (2004), pp. 516–522.
- S. Hafizovic, D. Barrettino, T. Volden, J. Sedivy, K.-U. Kirstein, O. Brand, A. Hierlemann, "Single-Chip Mechatronic Microsystem for Surface Imaging and Force Response Studies", *Proceedings of the National Academy of Science* 101 (2004), pp. 17011–17015.
- D. Barrettino, S. Hafizovic, T. Volden, J. Sedivy, K.U. Kirstein, A. Hierlemann, "CMOS Monolithic Mechatronic Microsystem for Surface Imaging and Force Response Studies", *IEEE Journal of Solid-State Circuits* 40 (2005), pp. 951–959.

CONFERENCE CONTRIBUTIONS

- T. Volden, D. Barrettino, S. Hafizovic, K.-U. Kirstein, A. Hierlemann, H. Baltes, "Single-chip AFM array with integrated digital controllers", Proc. IEEE Sensors, Vienna, Austria, October 24–27, 2004, pp. 1228–1231.
- T. Volden, M. Zimmermann, J. Lichtenberg, H. Baltes, "CMOS-Integrated Surface-Stress Sensor Array", 1st Workshop on Nanomechanical Sensors, Madrid, Spain, November 15–16, 2004, p. 32.
- T. Volden, M. Zimmermann, D. Lange, O. Brand, H. Baltes, "Dynamics of CMOS-based thermally actuated cantilever arrays for force microscopy", Proceedings of the 17th European Conference on Solid-State Tranducers, Eurosensors XVII, Guimarães, Portugal, September 21–24, 2003, pp. 192–193, ISBN 972-98603-1-9.
- S. Hafizovic, T. Volden, D. Barrettino, K.-U. Kirstein, A. Hierlemann, "Single-Chip Atomic Force Microscopy", Proc. IEEE International Conference on Micro Electro-Mechanical Systems (MEMS 2005), Miami, USA, January 30–February 3, 2005, pp. 638–641.

- D. Barrettino, S. Hafizovic, T. Volden, J. Sedivy, K.U. Kirstein, A. Hierlemann and H. Baltes, "CMOS Monolithic Atomic Force Microscope", Proc. IEEE Symposium on VLSI Circuits, Honolulu, USA, June 17–19, 2004, pp. 306–309.
- O. Brand, D. Lange, M. Zimmermann, C. Hagleitner, M. Ono, W. Franks, T. Volden, A. Hierlemann, H. Baltes, "CMOS-based 10-cantilever force sensor array for atomic force microscopy", Technical Program & Abstracts 11th International Conference on Scanning Tunneling Microscopy/Spectroscopy and Related Techniques STM'01, Vancouver, Canada, July 15–20, 2001, p. 46.
- K.U. Kirstein, Y. Li, M. Zimmermann, C. Vancura, T. Volden, W.H. Song, J. Lichtenberg, A. Hierlemann, "Cantilever-Based Biosensors in CMOS Technology", Design, Automation and Test in Europe (DATE 2005), 7–11 March 2005, Munich, Germany, pp. 1340–1341.

ACKNOWLEDGMENTS

I owe my greatest gratitude to Prof. Henry Baltes for giving me the opportunity to join his group and realize this thesis. His encouragement and trust from start to end, as well as his knowledge and wisdom have been a great inspiration. The top-quality working and social conditions in his laboratory are a great testimony of good leadership.

The co-examiners Prof. Oliver Brand and Dr. Jan Lichtenberg have followed my work and I am deeply grateful for their guidance, comments and corrections. All good parts of this thesis can be attributed to them.

Among my colleagues, my office-mates have been especially important. Wendy Franks has been a tremendous support from day zero, professionally as well as socially. Jürg Schwizer did most of his work outside the laboratory, but we often caught up in the powder slopes of mighty Swiss mountains. My later office-mates Martin Zimmermann and Yue Li made every day in the office a great pleasure. They both worked with me on projects, and Martin's circuitry work is an important contribution to this thesis.

Packaging and dynamic-cantilever experts Wan Ho Song and Cyril Vancura were also closely cooperating with me on the Biofinger project. On the AFM projects I had the pleasure to work with Sadik Hafizovic, Diego Barrettino and Dirk Lange, without whose contributions this thesis wouldn't be half of what it is.

I am thankful for the fruitful discussions with Prof. Korvink and Prof. Tabata during their visits and the help I received from the mechanical workshop of the physics department. Also students Jan Sedivy and Christian Koffmane did excellent work on our projects.

I very much enjoyed cooperation with our project partners from IMT in Neuchâtel (Switzerland), CIT and CUH in Cork (Irland) and CNM in Barcelona (Spain) and Martha in Berlin (Germany). Their friendly work spirit and hospitality during meetings and workshops gave us the best of international research cooperation.

In the laboratory, our staff Erna Hug, Yelena von Allmen, Christoph Kolb and Igor Levak were an excellent support. The technical competence of Donat Schei-

willer is especially appreciated. All other colleagues, including fellow research assistants and team leaders have been a great help, from enlightening discussions to efficient fabrication teamwork: Sergio Coronini, Urs Frey, Markus Graf, Frauke Greve, Christoph Hagleitner, Flavio Heer, Andreas Hierlemann, Nicole Kerness, Kai-Uwe Kirstein, Adrian Kummer, Petra Kurzawski, Tomi Salo, Andri Schaufelbühl, Robert Sunier, Stefano Taschini, Tobias Vancura and Timo.

Although not directly in the laboratory, the most important support has always come from my family and friends. Some geographically far away yet close in heart and mind; their love and encouragement has followed me from long time before I started here, and will support me further. New friends made living in Zurich a wonderful experience, as old friends make life a wonderful experience.

Thank you all!